FUNDAMENTAL STUDIES OF PALLADIUM AND PLATINUM SIZE-SELECTED MODEL CATALYSTS

by

Francis Sloan Roberts

A dissertation submitted to the faculty of
The University of Utah
in partial fulfillment of the requirements for the degree of

Doctor of Philosophy

Department of Chemistry

University of Utah

May 2014

The University of Utah Graduate School

STATEMENT OF DISSERTATION APPROVAL

The dissertation of **Francis Sloan Roberts**

has been approved by the following supervisory committee members:

Scott L. Anderson	, Chair	**3/20/2014** Date Approved
Peter B. Armentrout	, Member	**3/13/2014** Date Approved
Michael D. Morse	, Member	**3/14/2014** Date Approved
Marc D. Porter	, Member	Date Approved
Clayton C. Williams	, Member	Date Approved

and by **Cynthia J. Burrows**, Chair of

the Department of **Chemistry**

and by David B. Kieda, Dean of The Graduate School.

ABSTRACT

The research presented in this dissertation describes fundamental studies of size-selected palladium and platinum clusters supported on a metal oxide surface. Using carbon monoxide (CO) oxidation as a probe reaction, the catalytic activity as well as the surface properties of the model catalysts were investigated with an emphasis on elucidating the interplay between size-dependent physical and electronic structures. The details and background for model catalyst research are provided in Chapter 1 with a description of the importance of cluster size and how changes in the physical and electronic structure affect catalytic activity. A brief description of the experimental setup is presented at the end of Chapter 1 along with an introduction to a new and important addition to the setup -- a vacuum ultraviolet (VUV) lamp. The lamp was constructed with the goal of performing ultraviolet photoelectron spectroscopy, and the details of the design and operation are given in Chapter 2.

Using the newly designed VUV lamp, the valence electronic structure of the $Pd_n/TiO_2(110)$ model system was investigated in order to determine changes as a function of cluster size, CO exposure, and oxidation. The size-dependent core and valence level shifts were found to track equally in direction and magnitude, with the details given in Chapter 3. The focus then turns to the Pt_n/alumina/Re(0001) system to investigate the size-dependent surface properties and catalytic activity. Beginning in Chapter 4, the VUV lamp was used to measure the valence electronic structure of the model catalyst,

and it was determined that size-dependent shifts in the Pt_n valence band strongly correlate with the size-dependent activity for the CO oxidation reaction. The valence band structure is thought to determine how efficiently the clusters dissociatively adsorb oxygen, which is considered to be the rate limiting step in the reaction. Chapter 5 provides further detailed study of the physical and electronic structure of the model catalyst, and the findings suggest the growth of 3-dimensional clusters (as opposed to single layer, 2-dimensional clusters) to be vitally important in determining the electronic structure of the Pt_n clusters, and ultimately their catalytic activities.

TABLE OF CONTENTS

ACKNOWLEDGEMENTS

First and foremost, I would like to thank my advisor, Professor Scott L. Anderson, for allowing me the opportunity to work under his tutelage for the past five years. All of the strides I have made as a scientist and as a researcher are thanks to his willingness to discuss and share his experiences, granting me access to an invaluable source of wisdom. I feel my time spent in his laboratory at the University of Utah has successfully prepared me for life after graduate school, and for that, I am forever grateful.

Perhaps one of the best aspects of Scott's lab is the group dynamic that he has created. The bonds that I have formed between my lab mates, both past and present, have impacted my life greatly, and I hope to maintain them beyond my time spent here. Our unquestioning, mutual support of one another through difficult times made this experience better than I could have hoped for. I would like to particularly thank Matthew D. Kane for his deep personal friendship as well as his patience and brilliant insight when working together.

I would also like to thank the other members of my committee: Professor Peter B. Armentrout, Professor Michael D. Morse, Professor Marc. D. Porter, and Professor Clayton C. Williams. You consistently challenged me as a scientist while making me feel like a colleague – thank you. I owe the members of the chemistry department shops, Dale Heisler, Ron Jones, and Dennis Romney, a great deal of gratitude for their patience during my numerous visits.

Lastly, and most importantly, I would like to thank my loving family; my parents, Tri and Valerie, and my sister, Emily. They have been a steady source of strength and encouragement throughout my life, and I attribute the position I am in today to their eternal support.

CHAPTER 1

INTRODUCTION

1.1 Model Catalysts and Cluster Size

The importance of catalysts in the world today is unparalleled in terms of their ubiquitous use in chemical production, pollution remediation, as well as many other sectors, and are involved in about 35% of the world's gross domestic product (GDP).[1] Their ability to increase reaction rates and selectively determine the major reaction products provides the ultimate tool to control chemical processes. Because of their key role in such a large portion of the world's economy, there is a strong push to improve overall catalyst performance and reduce cost. As a result, there is a lot of work geared towards both applied catalysis research as well as fundamental research in order to obtain a basic understanding of catalyst functionality. Much of the fundamental work on heterogeneous catalysts involves the use of what are known as "model catalysts." While a real-world, applied catalyst typically consists of a high surface area metal oxide support decorated with a large size distribution of catalytic noble metal clusters (such as Pt, Au, etc.), model catalysts are instead prepared in a very controlled environment and are studied under precise reaction conditions. This control allows for many of the variables to be altered independently of one another, effectively determining what changes to the catalyst are affecting catalyst performance.[2-10]

The other advantage to using model catalysts for fundamental research is that the experiments are oftentimes performed under ultrahigh vacuum (UHV) conditions. Since all of the chemistry that takes place in heterogeneous catalysis occurs at the catalyst surface, understanding the surface properties of the catalyst is critical, with the ultimate goal of connecting fundamental properties of the catalytic system, such as physical and electronic structure, to their respective catalytic activity and performance. Using *in situ*

surface analysis tools, such as those afforded when researching model catalysts in UHV, allows for careful and controlled measurements to be made of the surface under different conditions. The ability to precisely control model catalyst construction as well as the reaction conditions, coupled with access to a multitude of detailed surface analysis techniques, makes UHV model catalyst research an effective approach to studying catalysts on a fundamental level. Recent improvements in computational methods and hardware have also allowed for a nice wedding of experimental and theoretical results, making model catalyst research an even more attractive approach.[11-22]

With the rise of model catalyst research, it quickly became evident that even small changes to the catalyst construction can have a significant impact on overall catalyst performance.[23-25] Improvements to surface imaging techniques, such as scanning tunneling microscopy (STM) and transmission electron microscopy (TEM), led to the discovery that many of these small changes can be attributed to changes in cluster size.[23, 26-30] Traditionally, it was thought that the active sites for the catalytic reactions were evenly spread across the surface and occurred anywhere the noble metal was present, regardless of cluster size. The reason for decorating them on a metal oxide support was simply to increase the surface area of the catalyst, thus increasing the density of available active sites. Changes to applied catalyst and model catalyst construction could change the average size of the clusters, and it was concluded that varying the average size also varies the surface area of the catalyst, thus tuning the performance of the catalyst. Later, with the improved ability to see clusters on the nanometer scale, it became obvious that many of the large, macro-size clusters are simply spectators, and the catalyst active sites are actually clusters only nanometers in size.

This was of particular interest in catalytic systems involving gold as the active sites since bulk gold is a generally inert metal, and not known to be catalytically active.[31-35] It turns out that as gold clusters become very small (on the order of a few nanometers or a few hundred atoms), their reactivity changes drastically. Many groups, such as the Haruta[23] and Goodman groups,[28, 30] found that there is in fact an optimal cluster size range of about 2-3 nm for these gold clusters when operating under carbon monoxide (CO) oxidation conditions. Further physical and electronic study of the model catalysts, using the wide array of surface analysis tools at their disposal, revealed the clusters in this size range are beginning to behave as if they are nonmetallic. In fact, when analyzing the catalytic activity of a wide array of cluster sizes, where the clusters begin to become nonmetallic in nature (cease to behave as bulk, inactive gold), the catalyst activity is at a maximum. The shift to nonmetallic clusters was concomitant with the clusters only being one or two atomic layers thick. This introduced the new idea that perhaps the story is not just about improved surface area; instead, as these clusters get very small and their surface areas increase, there electronic structure also changes, playing an important role in changing catalyst behavior.

Other studies have shown similar behavior for a wide array of model catalyst systems.[7, 22, 27, 36-41] The vital importance of cluster size not only lends critical information directly applicable to improving catalyst performance, but it also provides another variable to control and change when studying model catalyst systems. Conventional model catalyst construction methods provide only little control over cluster size. Typically, clusters are deposited onto the surface via either wet chemistry techniques or vapor deposition in vacuum. Wet chemistry techniques often involve

organic ligands which then must be burned off if to be studied in vacuum with surface analysis techniques. During the process of heating the surface to decompose the ligands, the clusters have a chance to sinter, losing the initial cluster size distribution. Vapor deposition uses a heat source to evaporate metal in vacuum with the sample positioned near the vaporization source. Since the metal evaporates and is deposited onto the surface as metal atoms, the only way to control cluster size is changing the temperature of the surface during deposition, as well as the anneal time after deposition. Varying the evaporation conditions ultimately affects the amount of sintering that occurs on the surface, thus giving control to how large or small the clusters are. These two conventional techniques will often result in a large cluster size distribution, and the ability to investigate very small clusters (< 100 atoms) or very small changes in cluster size, a different method must be employed.

With the motivation for more control over cluster size to not only determine which clusters perform best under different conditions, but also to elucidate reactant binding site information as well as what surface properties affect catalytic activity, the unique field of size-selected model catalyst research emerged. Here, gas phase metal atoms, produced via laser vaporization or magnetron sputtering, are cooled in a high pressure of noble gas to allow clustering to occur. Once the clusters are formed in the gas phase, their size can then be selected with atomic resolution using a mass spectrometer before deposition onto the support. The resulting model catalyst will ostensibly have the narrowest of size distributions possible with the ability to control the cluster size one atom at a time. Fundamental investigation of binding sites, physical and electronic structure, as well as catalyst activity can then be performed in order to precisely

determine what properties change with cluster size. Work using size-selected model catalysts has effectively shown unexpected behavior for only small variations in size for clusters in this size range (< 100 atoms) with clear correlations being drawn to the physical and electronic structure and the corresponding reactant binding sites.[7, 16, 22, 31, 40, 42-44] The research presented in this dissertation provides results from studying the $Pd_n/TiO_2(110)$ (n < 26 atoms) and $Pt_n/Al_2O_3/Re(0001)$ (n < 19 atoms) size selected model catalyst systems for the CO oxidation reaction. The emphasis of the work investigates the reactant binding sites as well as the interplay between physical and electronic structure, and ultimately shows how these properties affect catalyst activity with changing cluster size.

1.2 Experimental Setup

The instrument used for the experiments to be presented in this dissertation is comprised of two main components: the cluster beamline and the UHV chamber.[45, 46] The drawing in Figure 1.1 shows these two parts, with the beamline along the top connecting to the UHV chamber shown on the bottom. The beamline begins with the source region where laser ablation is used to produce metal atoms in the gas phase, and a helium pulse valve cools the atoms to allow clustering and propels them forward through the remainder of the beamline. After passing through several ion guides and focusing elements, the clusters are mass selected at a quadrupole mass selector and are finally guided into the UHV chamber where they are deposited on the surface. The energy of deposition can be controlled by varying the potential of the beamline relative to the grounded sample, and for all systems studied here the clusters were "soft landed" at ~ 1

eV/atom. The coverage was monitored by measuring the discharge current on the sample as the clusters neutralize upon deposition. In order to ensure adequate spacing between deposited clusters (minimizing cluster agglomeration), only 10% of a monolayer (ML) was deposited. This amount refers to the total number of metal atoms on the surface, not the number of clusters, in order to effectively normalize the reactivity and binding site measurements to metal coverage.

The UHV chamber consists of several surface analysis techniques which allows for *in situ* measurement of the size selected surface properties, such as low energy ion scattering spectroscopy (ISS) for physical structure, X-ray and ultraviolet photoelectron spectroscopy (XPS/UPS) for electronic structure, and temperature programmed reaction/desorption (TPR/TPD) for binding site and reactivity measurements. Surface cleaning and preparation techniques are also present including an ion gun for sputter cleaning the surface and electron bombardment to heat the sample to temperatures near 2200 kelvin. During the course of the research for this dissertation, a metal evaporation source was developed and tested to allow for epitaxially grown thin films. For the experiments described here, it was used exclusively for the growth of Al_2O_3 films up to 6 nm thick to be used as a model catalyst support. The source was designed to fit on the load lock chamber (see Figure 1.1) where the high pressure of background oxygen necessary to grow the films does not affect the pressure in the main UHV chamber.

Another addition to the experimental setup, which was designed and developed exclusively as a key component of this thesis work, is a vacuum ultraviolet (VUV) lamp for ultraviolet photoelectron spectroscopy (UPS). With only XPS available for analysis of the surface electronic structure, the data were limited to photoelectrons originating

from the core levels of the surface atoms. In order to measure the valence levels (which are the levels directly involved in chemical reactions), a source of ultraviolet photons was necessary, motivating the design of a VUV lamp suitable for the job. The details of the lamp design and functionality have several novel components worthy of publication as a note in *Review of Scientific Instruments* and comprise the second chapter of this dissertation.

1.3 References

1. Z. Ma and F. Zaera, in *Encyclopedia of Inorganic Chemistry* (John Wiley & Sons, Ltd, 2006).

2. U. Heiz and W.-D. Schneider, J. Phys. D: Appl. Phys. **33** (11), R85-R102 (2000).

3. D. W. Goodman, Surf. Rev. Lett. **2** (1), 9-24 (1995).

4. D. R. Rainer, C. Xu and D. W. Goodman, J. Mol. Catal. A: Chem. **119** (1-3), 307-325 (1997).

5. C. R. Henry, Surf. Sci. Rep. **31** (7-8), 235-325 (1998).

6. C. T. Campbell, A. W. Grant, D. E. Starr, S. C. Parker and V. A. Bondzie, Topics in Catalysis **14** (1-4), 43-51 (2001).

7. D.-C. Lim, C.-C. Hwang, G. Gantefoer and Y. D. Kim, Phys. Chem. Chem. Phys. **12** (46), 15172-15180 (2010).

8. V. Habibpour, Z. W. Wang, R. E. Palmer and U. Heiz, Journal of Applied Sciences **11** (7), 1164-1170 (2011).

9. F. Gao and D. W. Goodman, Annual Review of Physical Chemistry **63**, 265-286 (2012).

10. U. Heiz, A. Sanchez, S. Abbet and W.-D. Schneider, Chem. Phys. **262**, 189-200 (2000).

11. C. C. Chusuei, X. Lai, K. Luo and D. W. Goodman, Topics in Catalysis **14** (1-4), 71-83 (2001).

12. P. S. Bagus, F. Illas, G. Pacchioni and F. Parmigiani, J. Electron. Spectrosc. Relat. Phenom **100**, 215-236 (1999).

13. M. A. Omary, M. A. Rawashdeh-Omary, C. C. Chusuei, J. John P. Fackler and P. S. Bagus, J. Chem. Phys. **114** (24), 10695-10701 (2001).

14. T. Bredow and G. Pacchioni, Chem. Phys. Lett. **355** (5-6), 417-423 (2002).

15. C. Di Valentin, A. Del Vitto, G. Pacchioni, S. Abbet, A. S. Woerz, K. Judai and U. Heiz, Journal of Physical Chemistry B **106** (46), 11961-11969 (2002).

16. B. Yoon, U. Landman, V. Habibpour, C. Harding, S. Kunz, U. Heiz, M. Moseler and M. Walter, J. Phys. Chem. C **116** (17), 9594-9607 (2012).

17. C. Harding, V. Habibpour, S. Kunz, A. N.-S. Farnbacher, U. Heiz, B. Yoon and U. Landman, J. Am. Chem. Soc. **131** (2), 538-548 (2009).

18. H. Haekkinen, B. Yoon, U. Landman, X. Li, H.-J. Zhai and L.-S. Wang, J. Phys. Chem. **107** (32), 6168-6175 (2003).

19. B. Wang, B. Yoon, M. Koenig, Y. Fukamori, F. Esch, U. Heiz and U. Landman, Nano Letters **12** (11), 5907-5912 (2012).

20. S. Abbet, U. Heiz, H. Häkkinen and U. Landman, Phys. Rev. Lett. **86** (26), 5950-5953 (2001).

21. X. Lai and D. W. Goodman, J. Mol. Catal. A: Chem. **162** (1-2), 33-50 (2000).

22. U. Heiz and E. L. Bullock, Journal of Materials Chemistry **14** (4), 564-577 (2004).

23. G. R. Bamwenda, S. Tsubota, T. Nakamura and M. Haruta, Catalysis Letters **44** (1,2), 83-87 (1997).

24. M. Okumura, S. Nakamura, S. Tsubota, T. Nakamura, M. Azuma and M. Haruta, Catalysis Letters **51** (1,2), 53-58 (1998).

25. M. A. Newton, J. Evans and B. E. Hayden, Journal of Physical Chemistry B **104** (35), 8548 - 8553 (2000).

26. M. Chen, Y. Cai, Z. Yan and D. W. Goodman, J. Am. Chem. Soc. **128** (19), 6341-6346 (2006).

27. D. C. Meier and D. W. Goodman, Journal of the American Chemical Society **126** (6), 1892-1899 (2004).

28. M. S. Chen and D. W. Goodman, Science **306** (5694), 252-255 (2004).

29. M. Valden, S. Pak, X. Lai and D. W. Goodman, Catalysis Letters **56** (1), 7-10 (1998).

30. M. Valden, X. Lai and D. W. Goodman, Science **281** (5383), 1647-1650 (1998).

31. M. Haruta, Catalysis Today **36** (1), 153-166 (1997).

32. F. Cosandey and T. E. Madey, Surface Review and Letters **8** (1 & 2), 73-93 (2001).

33. M. Arenz, U. Landman and U. Heiz, ChemPhysChem **7** (9), 1871-1879 (2006).

34. U. Landman, B. Yoon, C. Zhang, U. Heiz and M. Arenz, Topics in Catalysis **44** (1-2), 145-158 (2007).

35. Y. Iizuka, H. Fujiki, N. Yamauchi, T. Chijiiwa, S. Arai, S. Tsubota and M. Haruta, Catalysis Today **36** (1), 115-123 (1997).

36. A. Kulkarni, R. J. Lobo-Lapidus and B. C. Gates, Chem. Commun. **46** (33), 5997-6015 (2010).

37. N. Isomura, X. Wu, H. Hirata and Y. Watanabe, J. Vac. Sci. Technol., A **28** (5), 1141-1144 (2010).

38. B. Ingham, M. F. Toney, S. C. Hendy, T. Cox, D. D. Fong, J. A. Eastman, P. H. Fuoss, K. J. Stevens, A. Lassesson, S. A. Brown and M. P. Ryan, Physical Review B: Condensed Matter and Materials Physics **78** (24), 245408/245401-245408/245405 (2008).

39. M. A. Roettgen, S. Abbet, K. Judai, J.-M. Antonietti, A. S. Woerz, M. Arenz, C. R. Henry and U. Heiz, J. Am. Chem. Soc. **129** (31), 9635-9639 (2007).

40. A. S. Woerz, K. Judai, S. Abbet and U. Heiz, J. Am. Chem. Soc. **125** (26), 7964-7970 (2003).

41. S. Abbet, A. Sanchez, U. Heiz and W.-D. Schneider, Journal of Catalysis **198** (1), 122-127 (2001).

42. S. Proch, M. Wirth, H. S. White and S. L. Anderson, J. Am. Chem. Soc. **135**, 3073−3086 (2013).

43. W. E. Kaden, T. Wu, W. A. Kunkel and S. L. Anderson, Science **326**, 826-829 (2009).

44. Y. Watanabe, X. Wu, H. Hirata and N. Isomura, Catalysis Science & Technology **1** (8), 1490-1495 (2011).

45. K. J. Boyd, A. Lapicki, M. Aizawa and S. L. Anderson, Review of Scientific Instruments **69**, 4106-4115 (1998).

46. M. Aizawa, S. Lee and S. L. Anderson, Surf. Sci. **542** (3), 253-275 (2003).

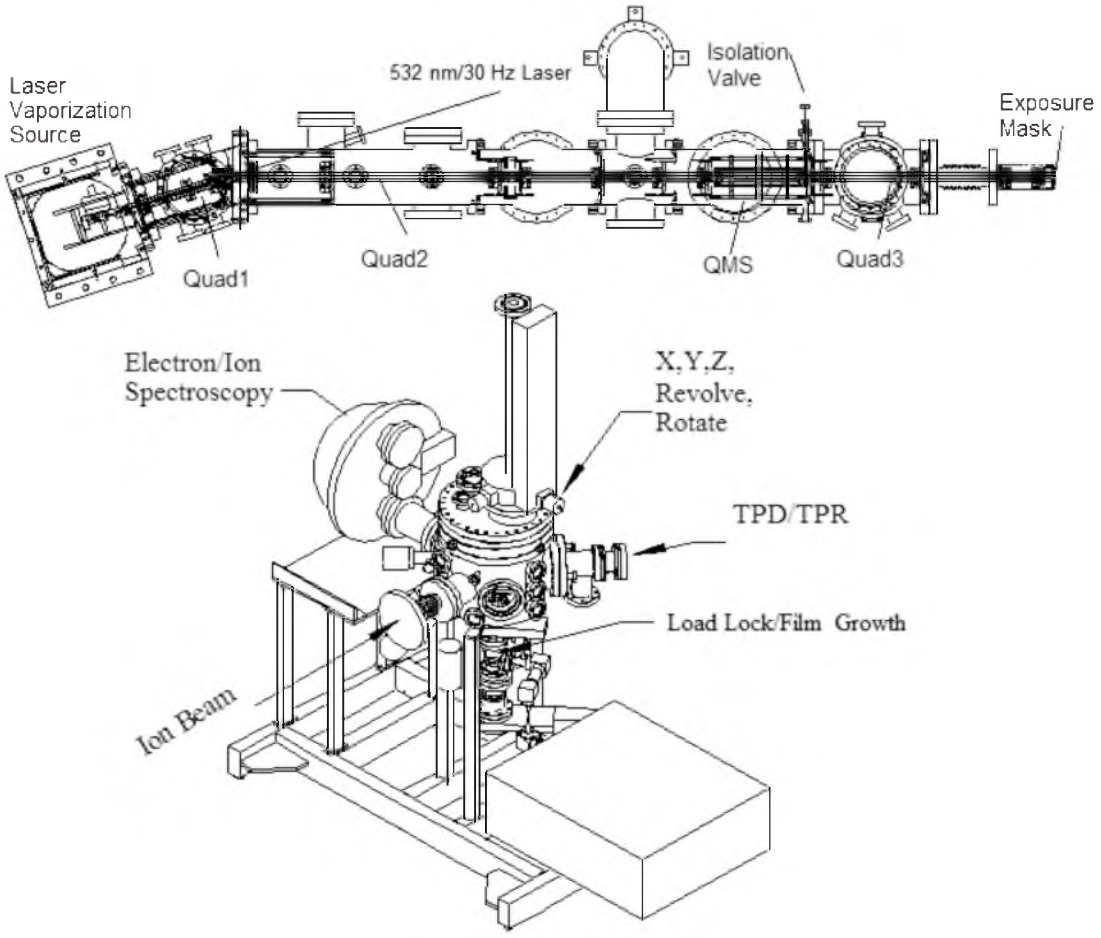

Figure 1.1 The experimental setup with the cluster deposition beamline along the top, and the UHV surface analysis chamber on the bottom.

CHAPTER 2

HOLLOW CATHODE LAMP WITH INTEGRAL, HIGH OPTICAL EFFICIENCY ISOLATION VALVE: A MODULAR VUV SOURCE

2.1 Introduction

Vacuum ultraviolet (VUV) Photoionization (PI) is a useful soft-ionization method, and VUV photoelectron spectroscopy (UPS) is a valuable tool to investigate the electronic structure of molecules in the gas phase, as well as the valence structure of surfaces and adsorbates. Simple windowless discharge lamps are common laboratory VUV sources, comprising a hollow capillary with hollow cathode and anode structures that can be filled to a few mbar with the discharge gas (typically a rare gas), with appropriate differential pumping to allow connection to high or ultrahigh vacuum systems. A discharge through the gas is maintained by a DC or RF potential applied across the anode and cathode, and depending on the discharge gas and pressure, photons of different energies can be obtained (e.g., HeI = 21.2 eV, HeII = 40.8 eV, NeI = 16.8, ArI = 11.8 eV, KrI = 10.0 eV). Since most of the energy range of interest is above the LiF cutoff, an important feature of such lamps is the use of grazing angle reflections off the internal surfaces of the capillary to guide photons from the discharge to near the sample position, greatly increasing the photon intensity. The capillary is also important in pumping, presenting a low conductance to the discharge gas, while guiding photons into the vacuum system, and to allow differential pumping, the capillary is typically cut in one or more locations.

A number of designs of such lamps have been reported over the years.[1–5] Most of these have hollow cathodes, with quartz or sapphire capillaries, depending on the required heat dissipation. Light from the discharge capillary passes into a wave-guiding capillary which extends into the vacuum chamber. These two capillaries are kept separate because the discharge capillary runs at high temperatures, and also needs to be

replaced periodically due to build-up of contaminants. Especially for UHV work, it is highly desirable to insert a UHV-compatible isolation valve between the discharge and wave guide capillaries, to allow the discharge section to be serviced without venting the UHV system. For example, Rowe et al.[5] reported a design including a UHV-compatible isolation valve; however, the valve used was relatively thick, and therefore required a large gap (~50 mm) between the discharge and wave guide capillaries, thereby resulting in a photon intensity loss across the gap. It is possible to at least partly compensate for transmission losses by increasing the lamp discharge power; however, this approach may complicate the design by requiring water cooling,[2] or use of high temperature construction materials.[3]

Here we report the design details of a small, easily constructed lamp with two stages of differential pumping, and incorporating a UHV-compatible slide valve at the second differential pumping stage. The valve is operated by a standard pneumatic linear motion feedthrough, and is used both to isolate the lamp for maintenance, and to protect the UHV system in case of accidental over pressure. The valve is thin, requiring only a 7 mm break in the capillary guide system, thus the transmission efficiency is improved compared to that reported by Rowe et al., allowing a simple air-cooled quartz discharge capillary to be used. The design, constructed on a standard 2-3/4" (DN-40) ConFlat flange, is simple to build and requires only common materials and construction methods. We have used this lamp successfully for both ultraviolet photoemission studies of surfaces in UHV, and for gas phase photoionization mass spectrometry.

2.2 Design

The assembled lamp is shown in Figure 2.1. There are two main sections, each holding a single capillary, which we will call the "discharge" and "waveguide" capillaries. The discharge capillary, which also serves differential pumping and waveguide functions, protrudes from the top of a stack of four cylindrical parts, which are clamped together by external screws that run between the "Screw Cap" and a modified 2-3/4" (DN-40) ConFlat flange. The capillary is held by three Viton o-rings that fit in conical sealing glands formed in between each component of the stack. As the stack is clamped together, the o-rings seal the stack together and to the capillary, as well as providing a strain-free, self-centering support for the capillary. The design allows the discharge capillary and o-rings to be replaced easily.

The 2nd differential pumping section holds the isolation valve and waveguide capillary. It is constructed from a 2-3/4" (DN-40) ConFlat nipple, with two mini-ConFlat (DN-16) side ports for differential pumping and operation of the isolation valve. The valve rides on a support pedestal that is screwed to the base flange of this section, and at the junction between the base flange and pedestal, there is another o-ring in a conical sealing gland that holds and seals the waveguide capillary. This is a vacuum-vacuum seal, and therefore a single o-ring is sufficient.

To allow the pumping and gas inlet arrangement to be seen more clearly, Figure 2.2 shows a detailed view of the discharge region, with gas flows and pressures for different regions of the capillaries indicated. Figure 2.3 shows details of the slide valve. Dimensioned construction drawings are included as supporting online information. With

the exception of the quartz capillaries and Viton o-rings, the valve is constructed from stainless steel.

2.2.1 Discharge Section

The discharge capillary is constructed from fused silica tubing of 2 mm ID and 8 mm OD. The outer end of the discharge capillary is capped with a cathode, constructed by welding a plug into an Ultra-Torr® fitting (Part# SS-6-UT-A-8BT). The cathode is simply attached to the end of the capillary by tightening the cap on the Ultra-Torr fitting, which compresses the internal Viton o-ring against the outside of the capillary. One obvious limitation of this approach is that the Viton o-ring may fail if the cathode temperature exceeds ~150 °C. The discharge region of the capillary is encased in a box constructed of UV-absorbing plastic, with a small fan fitted to the end of the box to cool the cathode. Some kind of enclosure is essential for safe operation, because the cathode is at high voltage during operation, and potentially hazardous UV light is emitted from the capillary.

The discharge capillary is clamped and sealed by three Viton o-rings compressed between the four parts that make up the discharge section of the lamp. These three o-rings logically break the capillary into four regions. The discharge region extends outside the lamp body, and the length of this section can be increased to increase the photon flux, albeit at the cost of greater lamp bulk and needing higher discharge voltage. For UPS, we have settled on a 50 mm discharge region as a good compromise between intensity and convenience.

Between the first two o-rings in the lamp body, the capillary wall is pierced by a 1.5 mm hole, drilled using an inexpensive diamond bit available from jewelry supply dealers. This hole size was chosen as a reasonable compromise between maintaining structural strength of the capillary, and having reasonable conductance to the inner bore. The discharge gas, e.g., Helium, is leaked into the lamp through a tube, thereby filling the discharge section of the capillary. The gas inlet is also the first point where the discharge can reach ground, and therefore serves also as an anode for the discharge. The capillary has a second 1.5 mm hole drilled in its wall, 22 mm from the first, and this hole connects to an annular volume that is defined by the 2nd and 3rd o-rings, and evacuated by a small rotary vane mechanical pump, equipped with a molecular sieve trap. To avoid conductance limits on pumping in this section, the central part of this annular volume has an inside diameter much larger than that of the capillary. The 22 mm distance between the gas inlet and the 1st stage pumping holes provides a significant conductance restriction, allowing the discharge region pressure to be considerably higher than the pressure in the first differential pumping stage. The discharge capillary extends 65 mm beyond the 1st pumping hole, and this region serves as a waveguide and conductance limiter, reducing the load on the 2nd differential pumping region.

2.2.2 Isolation Valve and Waveguide Section

The discharge capillary extends to just before the isolation valve, which is mounted on a support pedestal that is screwed to the base flange of the lamp. To allow for the isolation valve, a gap is necessary between the discharge and waveguide capillaries, which is minimized by making the valve thin. The gap also allows for much more

effective differential pumping than would result from simply drilling a hole in a continuous capillary. The valve itself (details in Figure 2.3) is simply a stainless steel slide with two angled surfaces which contact matching angled surfaces in a pair of valve guides, such that the valve slide is forced into contact with a Viton o-ring on the pedestal. The valve slide is attached to a pneumatically operated linear motion feedthrough, mounted on a min-ConFlat (DN-16) side port. The length of the actuator is adjusted so that the slide is actively held closed by air pressure on the actuator, ensuring a good seal. To minimize wear on the o-ring, the slide does not contact the o-ring until it is forced into contact by the rather steeply angled guide surfaces. To prevent the o-ring from twisting out of its groove by the closing/opening action of the slide, a dove-tail groove is used. Although the mechanism is relatively crude, we have never experienced a seal failure.

The valve pedestal is a cylinder that is screwed to the lamp's base flange. The joint between the pedestal and base includes another conical o-ring gland that seals the pedestal, base flange, and wave guide capillary together. The waveguide capillary extends into the UHV system to within ~18 mm of the sample surface, and because low energy electrons are quite sensitive to stray electric fields, it is important to avoid charging of the quartz capillary. To avoid charging, and to help keep the capillary concentric with the base flange, there is a metal shroud attached to the UHV side of the base flange, extending ~ 1 mm beyond the end of the capillary with the waveguide itself held in place simply by a tight bore tolerance through the end of the shroud.

Because the waveguide capillary is not subject to any mechanical stresses, we use a capillary with the same inside diameter (2 mm) but smaller outside diameter (4 mm),

compared to the discharge capillary. The smaller waveguide capillary allows use of a smaller diameter o-ring in the isolation valve, and also a smaller shroud.

2.3 Lamp Operating Conditions

The operating conditions for the discharge lamp are similar to those typically found in the literature as well as commercially available VUV lamps. For our application, a 3 kV, 75 mA power supply is used in series with a 50,000 Ohm (two 100,000 Ohm Ohmite resistors in parallel) ballast resistor in order to limit the discharge current to a maximum of 60 mA at 3 kV. This helps to provide a stable, reproducible electrical discharge to flow through the discharge capillary region. This voltage (positive polarity) is applied to the stainless steel cathode cap, and the discharge flows through the gas filled quartz capillary to the nearest electrical ground, which is the gas inlet ring. With helium as the discharge gas, it is possible to get emission on two VUV lines: HeI at 21.2 eV and HeII at 40.8 eV. In the following section, the conditions for maximum HeI emission are discussed.

In operation, the helium pressures were monitored at various points; the first and second differential pumping stages, as well as the final pressure in the UHV chamber. When leaking in increasing pressures of He while applying 3 kV to the cap, the discharge typically ignites at a pressure of ~ 1.30 mbar (1 Torr) at the first differential pumping stage, with pressure drops of three and seven orders of magnitude in the 2^{nd} pumping stage and UHV chamber, respectively. Once started, the optimum discharge conditions for HeI production were ~0.877 mbar (650 mTorr) in the first differentially pumped region, corresponding to ~1.0×10^{-3} mbar (7.5×10^{-4} Torr) in the second region, and

~1.33 x 10^{-7} mbar (~1.0 x 10^{-7} Torr) in the UHV chamber. The photocurrent on a sample ~18 mm from the end of the waveguide capillary was ~ 5.0 nA, corresponding to ~ 3 x 10^{10} photons/sec. Figure 2.4 shows example HeI UPS spectra of TiO_2(110) and Ta(110), in good agreement with literature results.[6,7] The spectra were taken using a hemispherical analyzer at a pass energy of 2.95 eV with the sample biased to -15.0 V in order to resolve the work function cutoff at high binding energy. Each spectrum had a three-minute collection time in order to obtain the desired signal to noise ratio as seen in Figure 2.4. As expected, the Ta(110) sample shows a sharp rise at the Fermi level (the zero of the binding energy scale), while the TiO_2(110) sample shows a band gap, along with states near the Fermi level due to bulk and surface oxygen vacancies.

Typical lamp maintenance and care consists mainly of cleaning/replacing the discharge capillary, when it becomes contaminated with metal sputtered from the electrodes, resulting in loss of photon intensity due to reduced wave guiding efficiency. In our application, the lamp is typically used less than 20 minutes at a time, and under these conditions, air cooling with a small fan is sufficient to prevent damage to the discharge capillary and its o-ring seals.

2.4 Conclusion

What has been described is a homebuilt hollow cathode discharge lamp for the production of VUV radiation suitable for UHV systems due to the gate valve between the discharge and waveguide regions allowing for quick maintenance without breaking UHV conditions. The lamp is simple enough to be designed and constructed by standard university machine shops, and the time and money invested is minimal compared to

traditional commercial VUV lamps. Beside the materials needed for the physical construction of the lamp (quartz tubing, raw stainless steel, bellows, o-rings), the only other required equipment are a power supply, ballast resistor, and pumps for the two stages of differential pumping. These materials are generally common items already present in a typical physical chemistry laboratory, and reusing them or buying previously used equipment is another money saver. It has been shown that the lamp is suitable for conducting ultraviolet photoelectron spectroscopy of surfaces as well as soft ionization of gas phase molecules.

2.5 References

1. J.E. Rowe, Rev. Sci. Instrum. **44**, 1675 (1973).

2. G. Schonhense and U. Heinzmann, J. Phys. E **16**, 74 (1983).

3. T. Durakiewicz, A. Arko, J.J. Joyce, D.P. Moore, and K. Graham, Rev. Sci. Instrum. **73**, 3750 (2002).

4. T.V. Vorburger, B.J. Waclawski, and D.R. Sandstrom, Rev. Sci. Instrum. **47**, 501 (1976).

5. J.E. Rowe, S.B. Christman, and E.E. Chaban, Rev. Sci. Instrum. **56**, 5 (1985).

6. S. Krischok, J. Guenster, D.W. Goodman, O. Hoefft, and V. Kempter, Surf. Interface Anal. **37**, 77 (2005).

7. S.-C. Li, Y. Losovyj, V.K. Paliwal, and U. Diebold, J. Phys. Chem. C **115**, 10173 (2011).

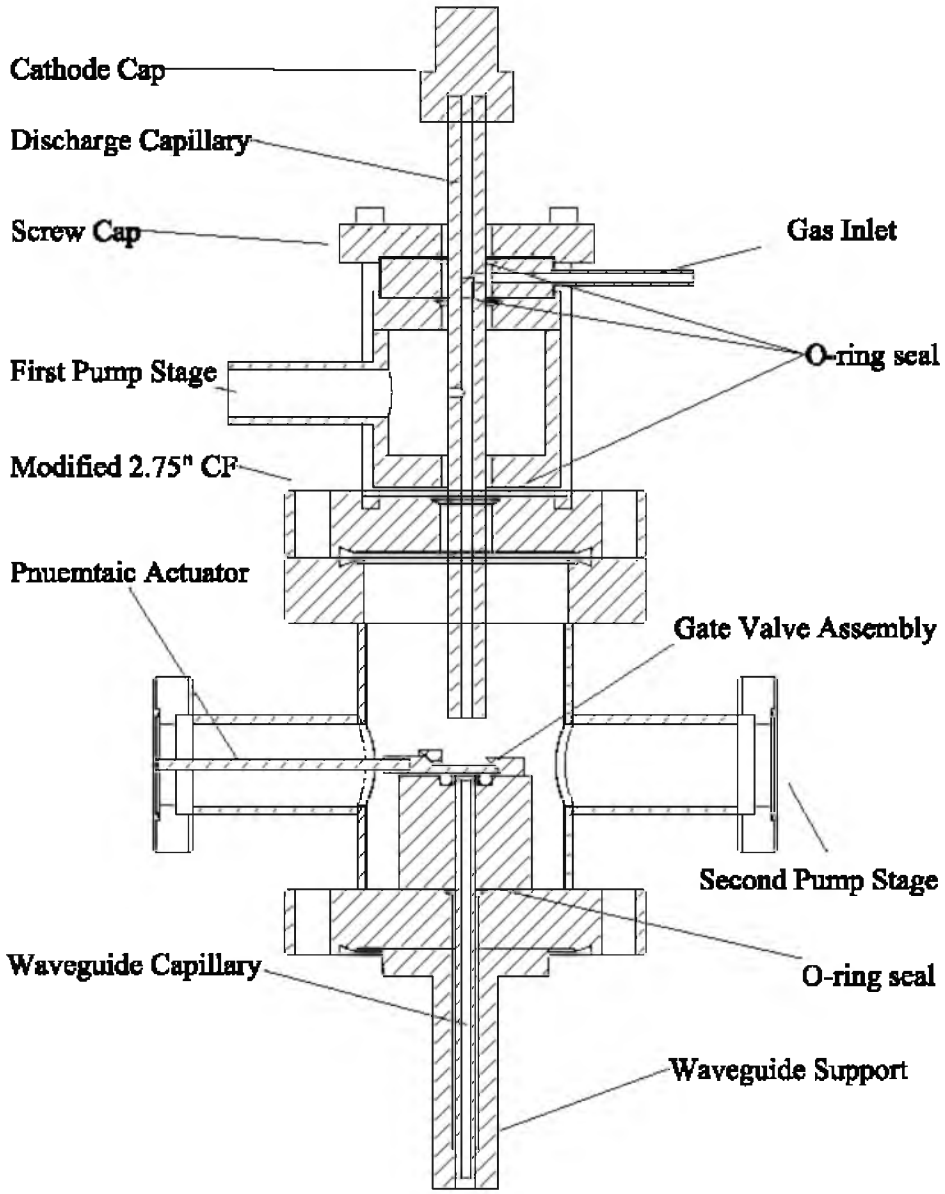

Figure 2.1 Cross-sectional view of the lamp highlighting the major components of the lamp, and how it is assembled.

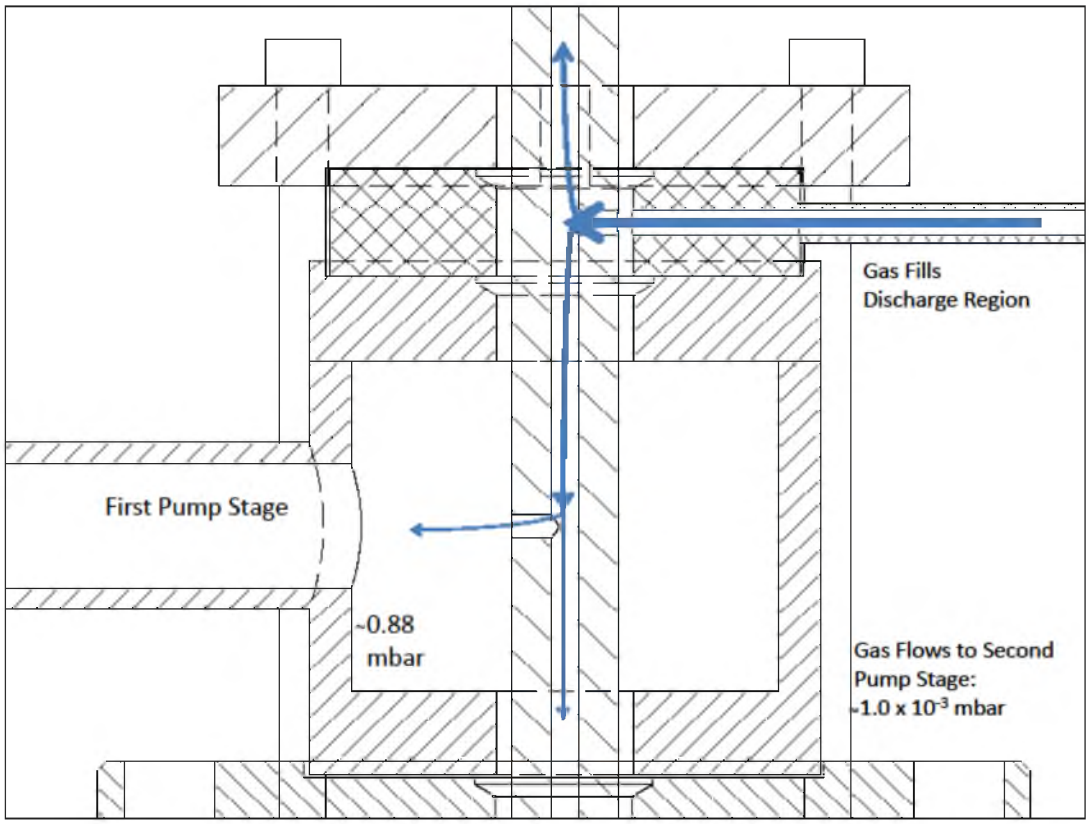

Figure 2.2 Cross-sectional detail of the discharge region describing the helium flow through the discharge capillary. Helium enters through the inlet ring and a 1.5 mm hole drilled in the discharge capillary, filling both the discharge region above the inlet, as well as being pumped out through the first stage of differential pumping before continuing to the second stage of pumping.

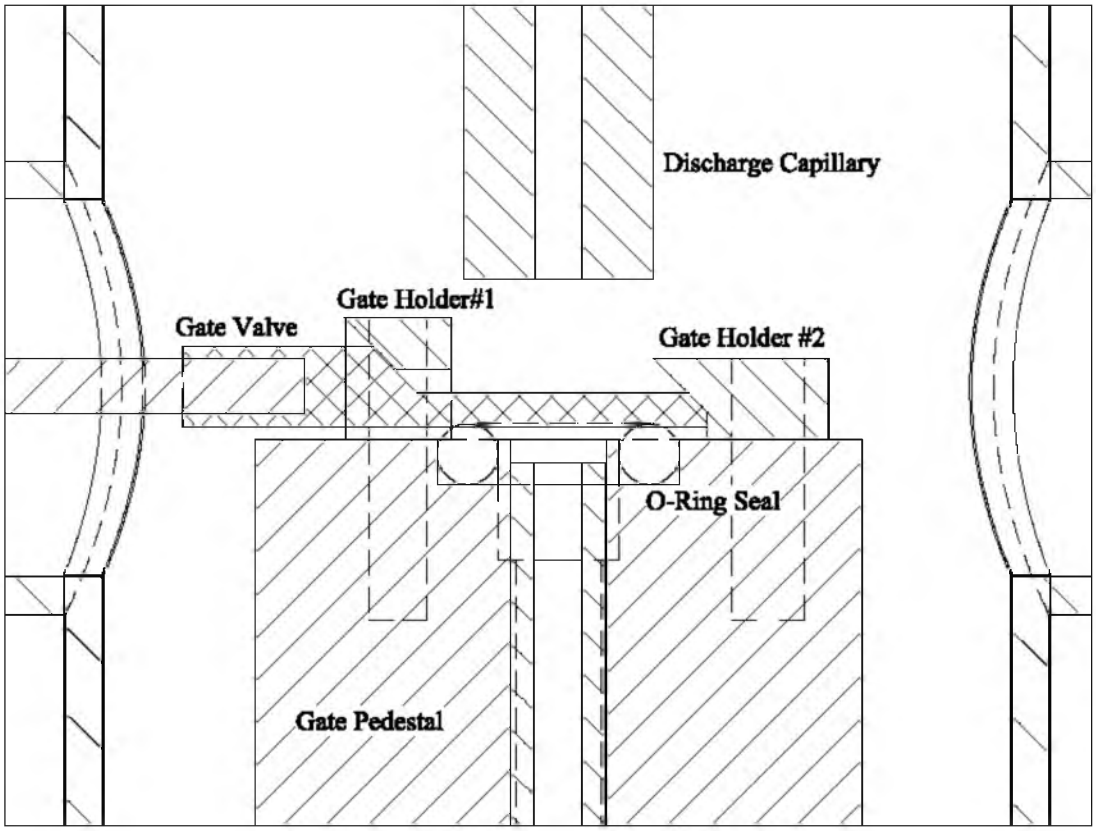

Figure 2.3 Detailed rendering of the gate valve apparatus. The gate is shown in the closed position, pushed firmly against the two angled stops. As the gate is opened, it relaxes upwards, releasing the seal against the o-ring.

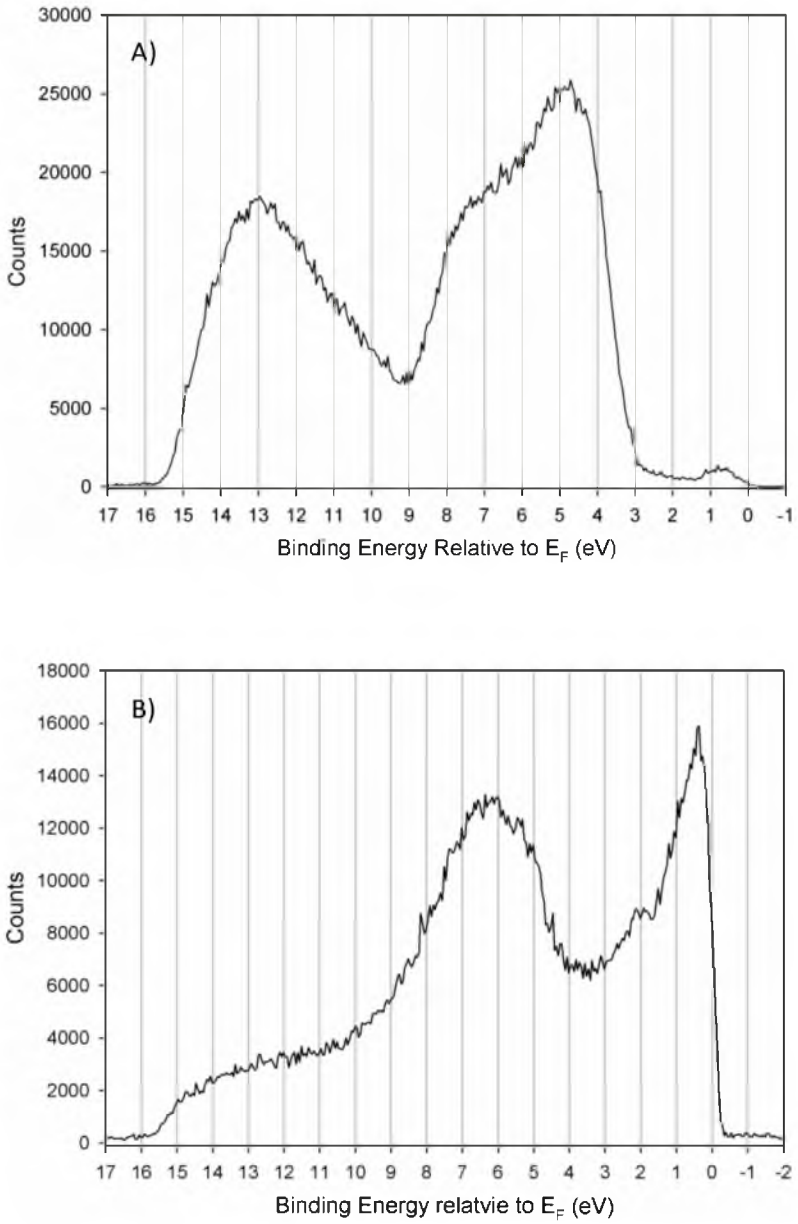

Figure 2.4 UPS spectra of TiO2(110) (a) and Ta(110) (b). Both spectra collected with a pass energy of 2.5 eV, and a -15.0 V sample bias.

CHAPTER 3

THE EFFECT OF CLUSTER SIZE, CO EXPOSURE, AND OXIDATION ON THE PHOTOELECTRON SPECTROSCOPY OF $Pd_n/TiO_2(110)$

3.1 Introduction

When investigating fundamental properties of atomically size-selected model catalysts, determining how the physical and electronic structure changes as a function of cluster size is paramount. Our group[1-3] and others[4-22] have shown that oftentimes it is the unique electronic properties of the clusters that enhance catalyst activity. A common method used to measure the electronic structure, and the technique discussed in this publication, is photoelectron spectroscopy (PES). The detailed theory and mechanism behind this surface analysis tool are well known and can be researched in the literature as well as many surface analysis textbooks[23-25]; however, difficulties remain when interpreting the experimental spectra as there are many competing variables that are not trivial to separate.[26-37] As a prelude to the work published here, which hopes to further demonstrate the importance of this problem, a brief description of initial and final state effects, and more importantly several of the experimental complications, is warranted.

During PES, the energy with which the photoelectron leaves the surface is dependent on the energy of the incident photon (i.e., how much energy is absorbed by the atom) as well as the initial binding energy (or orbital energy, according to Koopman's theorem) of that electron to the atom. Since the incident photon is generally speaking very well monochromatic, and since any given electron will at one time only possess a single, discrete binding energy (which is characteristic of the atom it belongs to), the result is a "fingerprint" spectrum with well-defined peaks relating to the different electron species and energies. This, however, is not the end of the story. Both fortunately and unfortunately, the energies of the ejected photoelectrons are complicated by other effects. Fortunately, because these effects allow us to measure such surface properties as the

chemical/oxidation state, and unfortunately because other effects, which result from the experimental process of removing an electron from the system, further complicate the spectrum and make it difficult to interpret the results.

These effects are known as initial and final state effects, and while the general theory behind PES is well understood, there is still work to be done with attempting to understand and interpret with complete detail the experimental results, mainly due to these two effects. Both of these "state" effects will shift the position of the peak in the spectrum, i.e. the measured binding energy of the photoelectron, from the expected "bulk" value. These shifts can be on the order of several electronvolts, and since it is possible to achieve energy resolution on the order of milli-electronvolts, theses shifts are quite significant. When referring to the "initial state" of the system, this is oftentimes thought of in terms on the chemical environment in which the atom is located, and the shifts are called "chemical shifts." A common example is the metal versus metal oxide system where the measured photoelectron energies from metal A in the fully metallic system will be significantly different than those from metal A in the metal oxide system. Since the metal is donating a significant amount of electron density to the oxygen in the metal oxide system, its "initial state" is relaxed, resulting in its electrons having a higher binding energy than those in the metallic system. While this does complicate the analysis of the spectrum, it is simultaneously a useful tool to determine the chemical state of the atom on the surface, and how this state changes under different conditions.

If initial state effects were the only complication to PES, then analysis would be fairly straightforward. However, there is a second effect, alluded to earlier, which is primarily an experimental effect that adds another shift to the measured energy of the

system – the final state effect. This is called the final state effect due to the fact that in order to measure the binding energy of an electron in the system, it must in fact be removed from that system, and this new state with one fewer electron is called the final state. When the electron is removed, it leaves behind a hole in the surface which it is then attracted to as it is moving into the vacuum. The extent of the photoelectron's attraction to the hole as it leaves the surface (and therefore how much energy it loses from this attraction) is determined by the ability of the surface electrons to effectively screen this hole. Also, when the electron is removed from its orbital, the energy of the remaining electrons can then relax, and if this relaxation occurs before the ejected photoelectron is completely decoupled from the system, then its energy will be affected. The change in the energy due to this new "final" state adds another shift to the spectrum. The experimental challenge comes when trying to deconvolute these effects to determine only the initial or final state contributions.

Recent work has shown that there are indeed ways to experimentally begin to separate these two effects, mainly via Auger electron spectroscopy (AES).[27, 33, 38] Like PES, this technique measures the energy of electrons that originated in surface atoms; however, it is a two electron process. As the first core level electron is ejected from the atom, a higher level electron can drop down to fill that hole, with the resulting energy gain being released by ejecting another electron. The idea is that this second photoelectron is originating from the "final state" of the first system (the system with the hole present). This is a useful technique, but can only be applied correctly to certain experimental systems.

The work presented here is yet another example of where having insight into the contributions from the initial and final states of the system would be very useful in interpretation of the data. For the atomically size-selected Pd clusters investigated here, there are expected to be significant contributions from both initial and final state effects, as it has been shown that when metal clusters are reduced below several hundred atoms, they begin to exhibit nonmetallic properties.[4, 5, 36] The main effect is the inability of the clusters to effectively screen the hole left from the emitted photoelectron, which is a final state effect. Unlike a metal that has a sea of delocalized electrons that can screen the hole (screening length on the order of 1 Å), these very small clusters instead have a finite electron density and behave as a nonmetal which is subject to this final state screening effect. When attempting to study the cluster electronic structure as related to cluster activity, which is a major focus of fundamental catalysis research, the final state contributions would ideally be removed from the spectra since these are considered experimental effects and shouldn't affect catalytic activity. Instead, the differences in the initial state of the clusters (the chemical state) are most likely controlling differences in catalytic activity, and contributions from the final state make it difficult to effectively determine what the different chemical states are.

The problem is met once more when investigating the effect adsorbates have on the photoelectron spectrum.[37] Again, obtaining the initial, chemical state of the system is what is desired; however, the adsorbates can affect the ability of the clusters to screen the resulting hole or stabilize the final state, once again changing the final state of the system and convoluting the spectrum. Past PES work from our group and others have shown the electronic structure of the clusters and their interaction with adsorbates to be a crucial

factor in predicting catalytic activity. The work presented here explores these problems from an experimental PES point of view for the $Pd_n/TiO_2(110)$ (n=1-25) system, and we show that the core and valence levels (XPS and UPS) are similarly affected, with some unexpected results when investigating oxygen and CO binding to the clusters. Theoretical work was done in order to help separate these initial and final state effects in order to better understand the experimental results.

3.2 Experimental

The cluster deposition beamline and UHV chamber (base pressure < 2.0×10^{-10} Torr) used in the following experiments have been described in detail previously,[39, 40] and the only difference with the experiments discussed here is the addition of a homebuilt VUV lamp.[41] The details of the lamp can be found in Ref 41, though a brief overview of the operating conditions used to collect the following UPS spectra will be discussed here. In addition to UPS, the UHV chamber is also equipped with X-Ray photoelectron spectroscopy (XPS), ion scattering spectroscopy (ISS), and a differentially pumped mass spectrometer positioned behind a skimmer cone for temperature programmed desorption/reaction (TPD/TPR).

Obtaining a UPS spectrum begins with igniting an electrical discharge in the hollow cathode and discharge capillary of the VUV lamp. The discharge was maintained at +3 kV and 60 mA using a 100,000 Ω ballast resistor, and ultrahigh purity helium cleaned through a liquid nitrogen cooled molecular sieve was the discharge gas, with the dominate UV emission line being the HeI line at 21.2 eV. To maximize the HeI line and minimize the weaker HeII line (40.8 eV), the pressure in the first differential pumping

region was held at 650 mTorr, with the second pumping region being about 7.0 x 10^{-4} Torr, and the pressure at the sample in the UHV chamber reaching 2.0 x 10^{-7} Torr. In order to resolve the high binding energy/low kinetic energy work function cutoff, the sample was biased to -15.0 V, effectively shifting the spectrum to high enough kinetic energy to resolve the spectral width without compromising peak resolution. Each UPS scan took about 3.5 minutes to obtain, and was collected using a hemispherical analyzer with a pass energy of 2.95 eV and 1.1 mm spot size.

The TiO_2(110) (Commercial Crystal Laboratories) support was glued to a tantalum backing plate using UHV compatible, high temperature glue (Aremco, Ceramabond 571) and initially annealed in UHV to 1050 K for 1 hour. The temperature was monitored with a K-type thermocouple glued to the top of the crystal. This heat treatment has been shown to create about 8% oxygen defects throughout the bulk of the crystal, turning it a dark blue and making it conductive enough to detect the Pd_n^+ clusters as they are deposited on the support, and perform photoelectron spectroscopy without charging.[42-44] Prior to each experiment, the TiO_2(110) support was cleaned by sputtering with 1 kV Ar^+ for 20 minutes, and then subsequently annealed to 900 K to restore surface order. XPS and UPS spectra were then collected to verify the cleanliness of the surface, i.e. no carbon, Pd, or other adsorbates were present. The number of oxygen vacancies and general surface order of the TiO_2(110) greatly affects the shape of the TiO_2(110) UPS spectrum, especially near the Fermi level (E_F) where the Pd will be present. UPS spectra were taken every day following the sputter and anneal cycles, and based on these spectra, the cycles used here were sufficient to achieve reproducible surface cleanliness and order.

Following preparation of the support, Pd_n^+ clusters ($n \leq 25$ atoms) were deposited at approximately 1 eV/atom onto the $TiO_2(110)$ crystal at room temperature with deposition currents ranging between 100 pA and 1,000 pA depending on the cluster size, corresponding to between 3- and 30-minute deposition times. Only 10% of a monolayer (ML) (1.53×10^{14} Pd atoms) was deposited in order to ensure adequate spacing between clusters, thus reducing the chance of clusters landing close enough together to agglomerate. Following deposition, XPS and UPS spectra were taken to determine the "as deposited" electronic structure of the particular supported cluster size before any gas dosing or heat treatments. The sample is then liquid nitrogen cooled to 180 K, and another UP spectrum was obtained (no XPS spectra was collected since it was previously determined there is little to no change in the spectrum after 20 minutes of cooling) to probe any change in the valence band of the surface following a 20 minute cool down time. Indeed there was little to no change in the UPS spectra upon reaching 180 K, with the only noticeable change being a possible attenuation of the entire spectrum, suggesting the presence of a ubiquitous surface adsorbate.

For samples that were only exposed to CO (not oxidized), 10 Langmuirs (1 L = 10^{-6} Torr x sec) of CO was dosed at 180 K using a calibrated direct dosing tube and a variable leak valve. At this temperature and CO exposure, the dose is considered to be saturating where every Pd atom present should have been exposed to at least one CO molecule, and given a near unity sticking coefficient for CO on Pd at 180 K, the Pd clusters can be considered completely saturated with as many CO molecules as can bind there. Following the CO exposure, another UPS spectrum was collected in order to see the effect of adsorbed CO on the Pd valence band as well as the rest of the spectrum,

including any shift in the surface work function. For samples that were oxidized, this was done at 400 K and a 10 L dose of O_2. Again, a UPS spectrum was recorded immediately following the dose in order to determine the effect of the oxygen exposure. After the CO dose, and subsequent to collecting the UPS spectrum, the sample was heated with a constant heat ramp of 3 K/sec in front of the differentially pumped mass spectrometer to desorb the CO. A final UPS spectrum was obtained after the completion of the TPD to determine the final electronic structure of the sample.

3.3 Photoelectron Spectroscopy Results

3.3.1 UPS of Clean TiO_2(110)

Before discussing the UPS data for the $Pd_n/TiO_2(110)$ model catalyst, a thorough understanding of the electronic structure of the $TiO_2(110)$ substrate is required. Figure 3.1 shows a UP spectrum of the clean (previously sputtered and annealed) $TiO_2(110)$ crystal consistent with spectra found in the literature.[45-47] There are three main areas of interest in the spectrum: 1) The region near the Fermi level between a binding energy of 0-3 eV showing a small peak present in the "band gap" region of TiO_2; 2) The region between 3-9 eV contains the O 2p band from the $TiO_2(110)$ surface, with the shape of the band dependent on the angle used to collect the spectrum since the sample has a localized periodic structure; 3) The region > 9 eV contains the secondary or scattered electron peak, as well as the sharp cutoff at high binding energy known as the work function cutoff or high binding energy cutoff. Before discussing the details of these three spectral regions, a discussion of how the binding energy scale is defined, and more specifically where the Fermi level is located (i.e. BE = 0 eV), is needed.

Since the Fermi level is defined as the energy level in which there is a 50% chance it is occupied by an electron in the system, at room temperature and in thermodynamic equilibrium, this generally means that all the states below the Fermi level are filled, and the ones above the Fermi level are unoccupied. For a metal, the valence band and conduction band are overlapping in this thermodynamic equilibrium, thus the Fermi level lies in the conduction band and is isoenergetic with the highest occupied molecular orbital (HOMO). This makes determining the energy of the Fermi level for a metal quite easy, as it is simply the highest kinetic energy electron detected in the spectrum. For an insulator or semiconductor, locating the Fermi level is not as trivial as it oftentimes lies somewhere in the band gap region where there are little to no states present. Fortunately, when two different materials come into electrical contact with one another, the Fermi levels align, with the different surface work functions now dictating the energy required to remove an electron into the vacuum level. This Fermi level alignment occurs via electron transfer from filled states in one material, to empty states in the other, thus bending the bands and aligning the Fermi levels. Experimentally, since the sample and hemispherical analyzer are in electrical contact with one another (through electrical ground), their respective Fermi levels align. Therefore, when the spectrum from a metal is measured, the inflection point of the sharp rise at highest kinetic energy is defined as the Fermi level and 0 Binding Energy. For an insulating or semiconducting sample also in electrical contact with the analyzer, such as our reduced $TiO_2(110)$ substrate, its Fermi level should align to the same energy, and should therefore be detected at the same kinetic energy in the spectrum. Because semiconductors oftentimes do not possess a significant density of states near the Fermi level (since it lies in the

pseudo-band gap), it can be difficult to determine the kinetic energy of the Fermi level using the semiconductor UP spectrum. Instead, a metallic standard in electrical contact with the system is used to calibrate the energy spectrum by fitting its rise at the high kinetic energy end of the spectrum.[48, 49] In the experiments reported here, a polycrystalline silver flag in contact with the TiO_2(110) sample holder is used to calibrate the energy scale (as discussed in Refs 48 and 49).

With the Fermi level defined and calibrated for each experiment (0 BE was determined to shift <0.05 eV from day to day), the features of the TiO_2(110) UP spectrum can now be discussed. Being an insulator turned semiconductor, the TiO_2(110) substrate has a significant band gap region that dominates the spectrum near the Fermi level (0-3 eV). Heat treating the sample results in minor decomposition of the TiO_2(110) crystal, creating oxygen vacancies in the surface as well as the bulk. The relatively electron rich oxygen vacancies and Ti^{3+} interstitials give rise to the small peak located at ~ 1.5 eV, and it is these states in the band gap region that result in the sample being slightly conductive. Following the spectrum to higher binding energy, the main peak of the UPS spectrum dominates beginning at ~ 3 eV, peaking at ~ 5 eV, and ending at ~ 9 eV. This peak is the O 2p valence band, and its position and shape is strongly dependent on the nature of the crystal, as well as the orientation relative to the hemispherical analyzer. This phenomenon is mainly due to the periodic, ordered structure of the surface[25] explaining the varied peak positions and shapes seen in the literature.[45, 46, 50, 51] Since angle resolved experiments were not performed here, there will be no more discussion of the shape of the O 2p peak. Finally, at a binding energy > 9 eV is the secondary (or scattered) electron peak. Since these electrons have undergone multiple interactions, they do not

retain information pertinent to the electronic bands of the surface and are generally uninteresting. However, the abrupt cutoff at high binding energy is dependent on the surface environment and the minimum energy required to remove an electron from the surface and into the spectrometer, effectively measuring the surface work function of the sample.

3.3.2 As Deposited Pd_n Clusters Supported on TiO_2(110)

Immediately following 0.1 ML Pd_n deposition, UP spectra were obtained for the as-deposited Pd_n clusters supported on clean TiO_2(110). Besides looking for new features in the UP spectra due to Pd being present on the surface, changes in the TiO_2 spectrum could occur due to band bending, surface dipoles, and surface work function changes.[49, 52, 53] This does not appear to be the case in this instance, presumably because UPS probes at least a depth of 3 nm, and any effects of band bending at the surface would be washed out by signal from the bulk, and the TiO_2 crystal is suitably conductive to prevent charge buildup. The most apparent difference is the appearance of significant signal at low binding energy near the Fermi level as can be seen in Figure 3.2. Since Pd is a metal with a high DOS near the Fermi level, the result shown in Figure 3.2 does not come as a surprise; however, since the clusters are on the order of a single nanometer in size, this size range tends to behave as nonmetallic in nature and can exhibit a pseudo-band gap. This is indeed the case for the Pd_n clusters deposited here, for if they were purely metallic, the signal would dominate mostly right at the Fermi level (0 BE); instead, they are shifted by ~ 0.5 eV towards higher binding energy, and their broad shape is a deviation from the comparably sharp onset typically seen for bulk metals.[54-56]

Qualitatively looking at each Pd_n UP spectrum, it becomes apparent that the energy-dependent shapes of the valence band structure can be split into two groups: "small" clusters ($1 \leq n \leq 10$) and "large" clusters ($16 \leq n \leq 25$). Figure 3.2a shows UP spectra near the Fermi level for $Pd_n/TiO_2(110)$ with n = 1,4,7,10. These "small" clusters, while having slightly different relative shifts towards higher binding energy, exhibit a very similar shape, with the signal rising relatively gradually without leveling off before the O 2p band dominates the spectrum. Figure 3.2b shows the same spectral region for $Pd_n/TiO_2(110)$ with n = 16,20,25. These three "large" clusters have a different shape with the Pd_n signal rising more sharply near the Fermi level and leveling off before meeting the O 2p band. The shape exhibited by the larger clusters, at least qualitatively, looks like what would be expected for clusters that are more metallic with the sharper rise near the Fermi level, where the smaller clusters look more nonmetallic with a gradual signal rise from the Fermi level. Since as the clusters become larger they should behave more like bulk Pd, this qualitative interpretation makes sense.

For a more quantitative picture, the clean $TiO_2(110)$ spectrum can be subtracted out of the $Pd_n/TiO_2(110)$ spectrum, with the remaining signal being entirely from the Pd_n clusters. This subtraction is made with the assumption that deposition of Pd_n clusters in no way affects the UP spectrum of the $TiO_2(110)$ substrate. With the clusters being soft landed at ~ 1 eV/atom, this should minimize any resulting surface damage, and any band bending that takes place seems to be evenly distributed through the bulk of the TiO_2 crystal and negligible. The subtraction for Pd_{20} is plotted in Figure 3.3a and the valence band onset was fit to determine exactly how far the clusters are shifted towards higher binding energy, with an example of the fit shown in Figure 3.3a. The fit consists of a

convoluted Heaviside and Gaussian function, and where the line tangent to the fit inflection point (position of the Gaussian) intersects, the baseline is determined to be the energy of the top of the Pd 4d band. For the system studied here, the onset of the Pd 4d band signal below the Fermi level shifts with different cluster sizes, with small clusters generally having a larger shift towards higher energy than large clusters.

As shown in Figure 3.3b, the onset of the Pd valence level signal below the Fermi level tracks very closely to the 3d core level shifts in binding energy as determined with XPS. Generally, as the cluster gets larger in size, the core level binding energy shifts more towards the value for bulk Pd, and the valence band shifts closer to the Fermi level, looking more metallic. The clear exception to this trend is for Pd atoms, which could sinter into large clusters, causing the abnormal shift towards lower binding energy – this is not thought the be the case, however, as it has been shown in previous publications the CO oxidation activity for atoms is virtually nonexistent, suggesting they do not sinter into large clusters which would result in CO oxidation activity.[1] Instead, the Pd atoms could very well migrate to electron rich oxygen vacancies, where accepting this extra electron density would also result in the observed electronic shift towards lower binding energy.

What is not so clear is why this abrupt change in shape occurs between Pd_{10} and Pd_{16}. Previous ion scattering spectroscopy (ISS) results published and discussed elsewhere[1, 44, 57] suggest that there is in fact a general cluster morphology change that takes place between Pd_{10} and Pd_{16}, with the small clusters being a single layer that wets the surface and the larger clusters beginning to form multilayer structure. Not only did the two cluster size regimes show different ISS results suggesting a morphology change, but CO oxidation experiments also have the larger clusters being nearly twice as active

the smaller ones.[1] Looking at the valence band shift from the Fermi level as seen in Figure 3.3b, there is not a clear discontinuity in the trend moving from the "small" clusters to the "large" clusters; however, once the clusters become multilayer ($n \geq 16$), their shifts from bulk become much more consistent and unchanging. Work by Watanabe has shown a similar effect for Pt_n clusters supported on $TiO_2(110)$,[58, 59] where once multilayer growth is reached, not only do the XPS shifts tend to flatten out, but this is also typically where catalyst activity begins to peak. As alluded to in the introduction, understanding the contribution from the initial and final state effects would help to better interpret the PES results.

3.3.3 CO Binding to $Pd_n/TiO_2(110)$

Following deposition of the Pd_n clusters, the sample was then cooled to 180 K and dosed with 10 L CO (this amount, at this temperature, will result in complete saturation of the Pd_n clusters with CO), and a UP spectrum was recorded to determine what affect CO binding has on the valence band of the Pd_n clusters. As shown in Figure 3.4, both Pd_7 (a "small" cluster) and Pd_{20} (a "large" cluster) have a significant loss of valence band signal closest to the Fermi level, suggesting this part of the band to be where CO is binding to the Pd_n cluster. While the initial shapes of the UP spectra for Pd_7 and Pd_{20} are fairly different, after CO has been dosed, their shapes are quite similar. This effect could simply be due to the fact that the dominant difference in the as deposited spectra is located closest to the Fermi level, and with this part of the spectra being attenuated due to the presence of CO, the difference can no longer be detected. It is also known that CO binding to clusters can actually cause them to physically fall apart. Since the shape of the

valence band after CO exposure resembles that of the small cluster sizes, this could imply that the clusters are breaking up and reaching the same final state. This is not believed to be the case in this experiment, however, as temperature programmed desorption data (TPD) of CO bound to the different cluster sizes result in size-dependent spectra unique to the cluster size and are described in detail elsewhere.[1, 44]

Previous XPS studies have shown that CO binding to Pd_n clusters results in a significant shift in the Pd 3d core level peak towards higher binding energy by ~ 0.6 eV.[30, 44] Since UPS measures valence bands instead of the quantized, confined core levels detected with XPS, it is not necessarily expected to see an identical "shift" in the valence band by the same energy. Instead, a rearrangement or reordering of the band structure to reflect electron density being occupied in the binding of CO is likely. It is still possible to fit the rise of the valence band post CO exposure as done for the as deposited Pd_n clusters, and those data can be seen in Figure 3.5. For all sizes, the onset of the valence band is indeed shifted towards higher binding energy, with a similar size shift for clusters n = 2-6 while the shifts are larger for clusters n > 7. Again, these shifts are in the valence band and come with a significant change in shape so it is difficult to compare them directly to those seen in the core levels of XPS.

After desorbing the CO via TPD, a UP spectrum was again collected and the details are shown for Pd_7 and Pd_{20} in Figure 3.6. While prior to CO exposure, there were distinct differences in the shapes of the spectra for the small and large clusters, post CO TPD, the shapes of the spectra are now nearly identical. As seen in Figure 3.6, Pd_7 and Pd_{20} now both look like a large cluster (compare to Pd_{20} as deposited) with more signal close to the Fermi level and a generally broader valence band. What this suggests is that

the clusters have reached some similar final electronic state post CO TPD, and for the small clusters, since their shape now resembles larger ones, they have perhaps sintered. Again, the onsets of the valence band rise near the Fermi level can be fitted, and the shifts post CO TPD are shown in Figure 3.5. As expected from the changes in shape (or lack thereof) seen for Pd_7 and Pd_{20}, the small clusters have a much smaller shift from the Fermi level and are nearly identical to that of the larger clusters which do not shift any considerable amount.

Previous XPS data[60] corroborate the evidence for reaching a similar final state post CO TPD as all of the Pd 3d binding energies are virtually identical, where the as deposited binding energies varied greatly. Detailed investigation of how the model catalysts behave with repeated use ultimately suggest that the clusters exhibit the strong metal support interaction (SMSI) with the $TiO_2(110)$ support.[60] Other studies of $Pd/TiO_2(110)$ have shown this to be the case,[61-65] with some debate about what exactly is occurring during the interaction to reduce the amount of Pd in the surface layer. Whether a combination of sintering and the growth of a TiO_x overlayer, it is clear from XPS and UPS that after a single CO TPD cycle a basic electronic final state is reached for the Pd_n clusters.

A similar experiment was done, heating the sample to 500 K (the end of the CO desorption cycle) without dosing CO to view the effect heating has on the valence electronic structure of the clusters. Since the larger clusters show no significant change in electronic structure post CO TPD (see Pd_{20} in Figure 3.5), this experiment was carried out only for Pd_7, and the resulting UP spectrum can be seen in Figure 3.7. It is clear that the change in shape of the valence band after a CO TPD can also be achieved by simply

heating the sample to the same temperature (500 K) in vacuum. Again, a similar result can be seen with XPS, as the most significant BE shift comes from heating the sample as opposed to doing a CO TPD or TPR where the shift is smaller.[60] The ISS results show no significant change, however, suggesting there is no drastic restructuring or reordering that occurs.[60] Whatever changes are taking place are either happening at the periphery of the cluster (and cannot be detected in ISS) or simply changing how or where the cluster is electronically bound to the surface.

3.3.4 Oxidation of $Pd_{20}/TiO_2(110)$

In typical CO oxidation reactions over Pd/TiO_2, the surface is generally oxidized first as CO tends to poison the active sites,[66, 67] preventing enough reactive oxygen to be present to initiate CO oxidation. It has been shown that oftentimes the activation of oxygen on the clusters is in fact the limiting step in the reaction, and the oxygen activation efficiency of the clusters is what ultimately controls the reactivity.[57] The oxidation of $Pd_{20}/TiO_2(110)$ and the effect it has on the UP spectrum is shown in Figure 3.8. Here, immediately following the collection of the as deposited UP spectrum, the sample was heated to 400 K and dosed with 10 L O_2. These conditions have shown significant activity towards CO oxidation for Pd_{20} in the past[1, 2] and are used here for comparison. One major difference immediately seen is a shift in the entire UP spectrum, notably the high binding energy cutoff (signifying a change in the surface work function) as well as the O 2p band shifting from about 4.8 eV to 4.5 eV. The valence band of Pd_{20} only has a small change, and again it is attenuation in signal near the Fermi level, with the details shown in Figure 3.9. When looking at the oxidation of pristine $TiO_2(110)$, and

seeing the loss of the oxygen vacancy peak near the Fermi level (~ 1.5 eV), it becomes clear that the change seen in oxidizing the Pd_{20}/TiO2(110) surface is simply a change in the oxidized TiO_2(110) substrate, and not the Pd_{20} valence band. Comparing the subtractions of as deposited Pd_{20}/TiO_2(110) minus pristine TiO_2(110) with oxidized Pd_{20}/TiO_2(110) minus oxidized TiO_2(110), it becomes obvious that the Pd_{20} valence band is indeed not showing major change after oxidation (see Figure 3.9b).

The lack of change in the valence level upon oxidation is surprising as it is clear the Pd_n clusters are necessary for oxygen activation in the CO oxidation reaction. Perhaps the presence of the Pd_{20} clusters creates a new O_2 binding site on the TiO_2(110) surface that "activates" it for the CO oxidation reaction, but does not greatly affect the electronic structure of the Pd_n cluster itself. Or since UPS is sensitive to the work function of the surface (where XPS is not), it is possible the majority of the oxidation effect is partially "canceled" by an equal and opposite shift in the work function. Another more likely explanation of the different shifts seen for CO and O_2 exposure is that they affect the initial and final states of the system (as measured with PES) differently. As mentioned earlier, combining these experimental results with theoretical work could give a better understanding of what effects are ultimately controlling the PE spectra under different conditions.

3.4 Conclusion

The detailed investigation of the core and valence level electronic structure of the Pd_n/TiO_2(110) system revealed size dependent electronic changes for the pristine model catalyst surface as well as the effects of CO exposure, heating, and oxidation. As the

clusters increase in size, their core and valence levels shift closer to the bulk value (by the same amounts) consistent with other studies in the literature. The size range can be split into two groups that have similar valence band shapes, with the groups corresponding to single and multilayer structure as determined with ISS. Exposure to CO results in significant changes in the valence level structure for all the cluster sizes studied, showing an attenuation of the signal nearest the Fermi level, as well as an overall band shift towards higher binding energy. After a CO TPD, the size-dependent nature of the valence band shifts are largely nonexistent as they are all located closer to the Fermi level and resemble a "large" cluster. Surprisingly, oxidation results in little to no change in the valence level of Pd_{20} even though it is thought the Pd_n is directly involved in activating the oxygen for CO oxidation. Theoretical work to help separate initial and final state effects would be ideal for this system, and could help explain the major differences in the measured PES as a function of cluster size. Theory could also be used to explore the effect adsorbates (such as differing amounts of CO and O) have on the initial and final states of the Pd_n clusters in order to better understand why CO and O_2 exposure result in such a different experimental changes in electronic structure.

3.5 References

1. W. E. Kaden, T. Wu, W. A. Kunkel and S. L. Anderson, Science **326**, 826-829 (2009).

2. M. D. Kane, F. S. Roberts and S. L. Anderson, Faraday Disc. **162**, 323 - 340 (2013).

3. S. Proch, M. Wirth, H. S. White and S. L. Anderson, J. Am. Chem. Soc. **135**, 3073−3086 (2013).

4. M. Valden, X. Lai and D. W. Goodman, Science **281** (5383), 1647-1650 (1998).

5. M. S. Chen and D. W. Goodman, Science **306** (5694), 252-255 (2004).

6. J. R. Kitchin, J. K. Norskov, M. A. Barteau and J. G. Chen, Physical Review Letters **93** (15), 156801/156801-156801/156804 (2004).

7. S. V. Ong and S. N. Khanna, J. Phys. Chem. C **116** (4), 3105-3111 (2012).

8. J. Zhang and A. N. Alexandrova, J. Chem. Phys. **135** (17), 174702/174701-174702/174710 (2011).

9. R. Dietsche, D. C. Lim, M. Bubek, I. Lopez-Salido, G. Gantefoer and Y. D. Kim, Appl. Phys. A: Mater. Sci. Process. **90** (3), 395-398 (2008).

10. I. Aruna, B. R. Mehta, L. K. Malhotra and S. M. Shivaprasad, J. Appl. Phys. **104**, 064308-064301-064305 (2008).

11. M. Arenz, S. Gilb and U. Heiz, Chemical Physics of Solid Surfaces **12** (Atomic Clusters), 1-47 (2007).

12. H. Yasumatsu, T. Hayakawa and T. Kondow, J. Chem. Phys. **124** (1), 014701/014701-014701/014707 (2006).

13. U. Heiz and E. L. Bullock, Journal of Materials Chemistry **14** (4), 564-577 (2004).

14. S. Arrii, F. Morfin, A. J. Renouprez and J. L. Rousset, J. Am. Chem. Soc. **126** (4), 1199-1205 (2004).

15. K. Judai, A. S. Woerz, S. Abbet and U. Heiz, NATO Science Series, II: Mathematics, Physics and Chemistry **116** (Metal-Ligand Interactions), 153-192 (2003).

16. M. A. Omary, M. A. Rawashdeh-Omary, C. C. Chusuei, J. John P. Fackler and P. S. Bagus, J. Chem. Phys. **114** (24), 10695-10701 (2001).

17. I. Meusel, J. Hoffmann, J. Hartmann, J. Libuda and H.-J. Freund, Journal of Physical Chemistry B **105** (17), 3567 -3576 (2001).

18. S. Minemoto, A. Terasaki and T. Kondow, Journal of Electron Spectroscopy and Related Phenomena **106** (2-3), 171-178 (2000).

19. G. Pacchioni, N. Lopez and F. Illas, Faraday Discuss. **114** (Surface Science of Metal Oxides), 209-222 (1999).

20. C. P. Vinod, G. U. Kulkarni and C. N. R. Rao, Chem. Phys. Lett. **289** (3,4), 329-333 (1998).

21. X. Lai, T. P. St. Clair, M. Valden and D. W. Goodman, Prog. Surf. Sci. **59** (1-4), 25-52 (1998).

22. H. V. Roy, J. Boschung, P. Fayet, F. Patthey and W. D. Schneider, Z. Phys. D: At., Mol. Clusters **26** (1-4), 252-254 (1993).

23. J. F. Moulder, W. F. Stickle, P. E. Sobol, K. D. Bomben and J. J. Chastain & R. C. King, eds., *Handbook of X-ray Photoelectron Spectroscopy*. (Physical Electronics, Eden Prarie, MN, 1995).

24. J. A. R. Samson, *Techniques of Vacuum Ultraviolet Spectroscopy*. (Wiley, New York, 1967).

25. D. P. Woodruff and T. A. Delchar, *Modern Techniques of Surface Science, 2nd Ed.* (Cambridge U. Pr., Cambridge, 1994).

26. M. G. Mason, Phys. Rev. B **27**, 748-762 (1983).

27. G. Hohlneicher, H. Pulm and H.-J. Freund, J. Electron. Spectrosc. Relat. Phenom **37**, 209-224 (1985).

28. S. L. Qiu, X. Pan, M. Strongin and P. H. Citrin, Phys. Rev. B: Condens. Matter **36** (2), 1292-1295 (1987).

29. G. K. Wertheim, Z. Phys. D **12**, 319-326 (1989).

30. G. Comelli, M. Sastry, G. Paolucci, K. C. Prince and L. Olivi, Phys. Rev. B **43** (18), 14385–14389 (1991).

31. P. S. Bagus, F. Illas, G. Pacchioni and F. Parmigiani, J. Electron. Spectrosc. Relat. Phenom **100**, 215-236 (1999).

32. A. Howard, D. N. S. Clark, C. E. J. Mitchell, R. G. Egdell and V. R. Dhanak, Surf. Sci. **518** (3), 210-224 (2002).

33. J. G. Tao, J. S. Pan, C. H. A. Huan, Z. Zhang, J. W. Chai and S. J. Wang, Surf. Sci. **602** (16), 2769-2773 (2008).

34. B.-H. Mao, R. Chang, S. Lee, S. Axnanda, E. Crumlin, M. E. Grass, S.-D. Wang, S. Vajda and Z. Liu, J. Chem. Phys. **138**, 214304-214311 (2013).

35. S. Peters, S. Peredkov, M. Neeb, W. Eberhardt and M. Al-Hada, Surf. Sci. **608**, 129-134 (2013).

36. N. Martensson and A. Nilsson, Journal of Electron Spectroscopy and Related Phenomena **75**, 209-223 (1995).

37. A. Nilsson, Journal of Electron Spectroscopy and Related Phenomena **126**, 3-42 (2002).

38. C. D. Wagner and J. A. Taylor, J. Electron. Spectrosc. Relat. Phenom **28**, 211-218 (1982).

39. K. J. Boyd, A. Lapicki, M. Aizawa and S. L. Anderson, Review of Scientific Instruments **69**, 4106-4115 (1998).

40. S. Lee, C. Fan, T. Wu and S. L. Anderson, J. Am. Chem. Soc. **126** (18), 5682-5683 (2004).

41. F. S. Roberts and S. L. Anderson, Review of Scientific Instruments (2013).

42. M. Li, W. Hebenstreit and U. Diebold, Phys. Rev. B **61** (7), 4926-4933 (2000).

43. M. Li, W. Hebenstreit, U. Diebold, A. M. Tyryshkin, M. K. Bowman, G. G. Dunham and M. A. Henderson, Journal of Physical Chemistry B **104** (20), 4944-4950 (2000).

44. W. E. Kaden, W. A. Kunkel, F. S. Roberts, M. Kane and S. L. Anderson, J. Chem. Phys. **136**, 204705/204701-204705/204712 (2012).

45. M. Brause and V. Kempter, Surface Science **490**, 153-159 (2001).

46. S. Krischok, J. Guenster, D. W. Goodman, O. Hoefft and V. Kempter, Surface and Interface Analysis **37** (1), 77-82 (2005).

47. S. Krischok, O. Hoefft, J. Guenster, J. Stultz, D. W. Goodman and V. Kempter, Surface Science **495**, 8-18 (2001).

48. L. N. Kantorovich, A. L. Shluger, P. V. Sushko, J. Günster, P. Stracke, D. W. Goodman and V. Kempter, Faraday Discussions **114**, 173-194 (1999).

49. R. Schlaf, P. G. Schroeder, M. W. Nelson, B. A. Parkinson, C. D. Merritt, L. A. Crisafulli, H. Murata and Z. H. Kafafi, Surf. Sci. **450**, 142-152 (2000).

50. S. Krischok, O. Hofft, J. Gunster, J. Stultz, D. W. Goodman and V. Kempter, Surf. Sci. **495**, 8-18 (2001).

51. S. Krischok, O. Hofft and V. Kempter, Surf. Sci. **507-510**, 69-73 (2002).

52. R. A. Bennett, J. S. Mulley, M. A. Newton and M. Surman, J. Chem. Phys. **127** (8), 084707/084701-084707/084707 (2007).

53. L. Zhang, R. Persaud and T. E. Madey, Phys. Rev. B **56**, 10549 (1997).

54. J. Guenster, M. Brause, T. Mayer, A. Hitzke and V. Kempter, Nucl. Instrum. Methods Phys. Res., Sect. B **100** (2,3), 411-416 (1995).

55. W. Maus-Friedrichs, M. Wehrhahn, S. Dieckhoff and V. Kempter, Surf. Sci. **237**, 257-265 (1990).

56. D. J. Alberas, J. Kiss, Z.-M. Liu and J. M. White, Surf. Sci. **278** (1-2), 51-61 (1992).

57. W. E. Kaden, W. A. Kunkel, M. D. Kane, F. S. Roberts and S. L. Anderson, J. Am. Chem. Soc. **132**, 13097–13099 (2010).

58. N. Isomura, X. Wu, H. Hirata and Y. Watanabe, J. Vac. Sci. Technol., A **28** (5), 1141-1144 (2010).

59. Y. Watanabe, X. Wu, H. Hirata and N. Isomura, Catalysis Science & Technology **1** (8), 1490-1495 (2011).

60. W. E. Kaden, W. A. Kunkel, F. S. Roberts, M. Kane and S. L. Anderson, Surface Science **621** (0), 40-50 (2014).

61. J. Sa, J. Bernardi and J. A. Anderson, Catalysis Letters **114** (1-2), 5 (2007).

62. M. Bowker, P. Stone, R. Bennett and N. Perkins, Surf. Sci. **497** (1-3), 155-165 (2002).

63. R. A. Bennett, C. L. Pang, N. Perkins, R. D. Smith, P. Morrall, R. I. Kvon and M. Bowker, Journal of Physical Chemistry B **106** (18), 4688 -4696 (2002).

64. R. A. Bennett, P. Stone and M. Bowker, Catalysis Letters **59** (2-4), 99-105 (1999).

65. J. M. Herrmann, Journal of Catalysis **89** (2), 404-412 (1984).

66. H. Conrad, G. Ertl and J. Kueppers, Surface Science **76** (2), 323-342 (1978).

67. T. Engel and G. Ertl, Chemical Physics Letters **54** (1), 95-98 (1978).

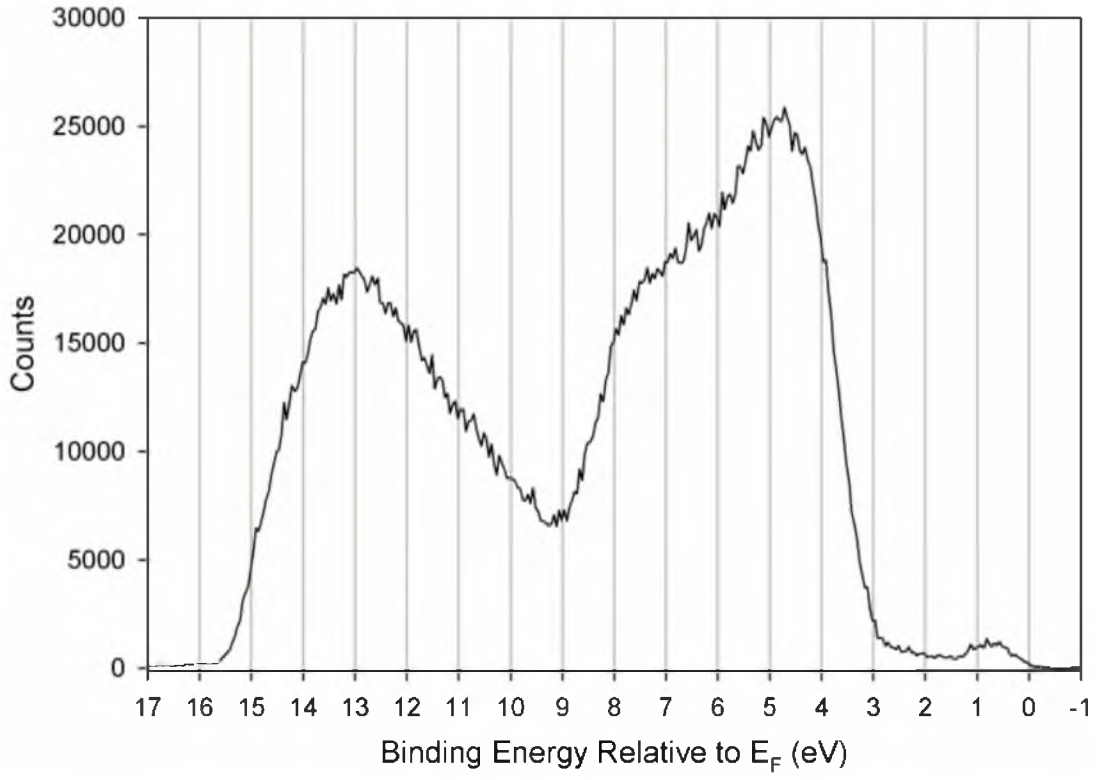

Figure 3.1 UP spectrum for clean TiO_2(110) after the anneal process described in the text.

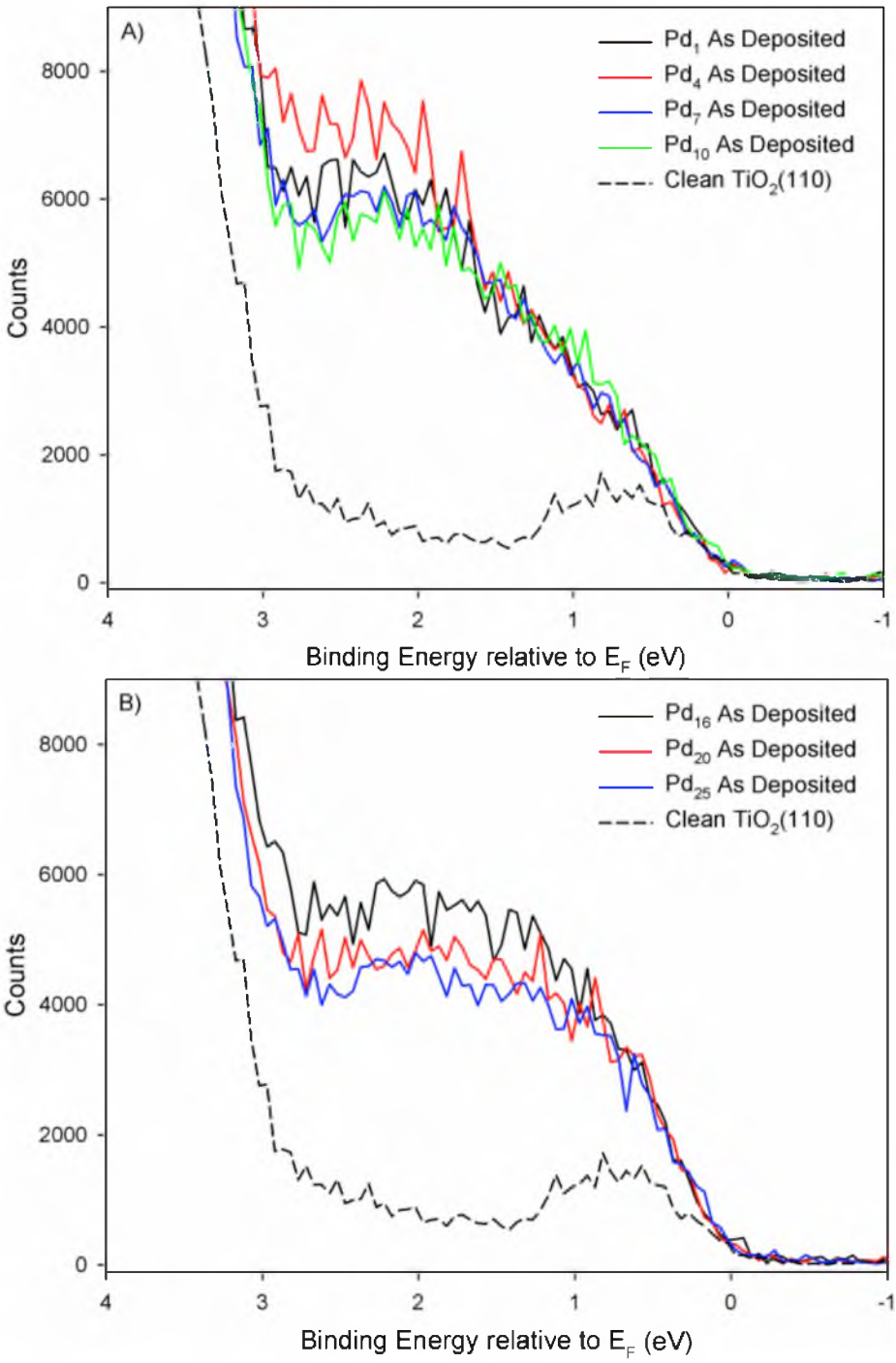

Figure 3.2 UP spectra of as deposited Pd_n clusters. There are two different size ranges that give the two distinct shapes: the "small" clusters (n = 1-10) shown in (a) have a more gradual rise from the Fermi level with higher density between 2-3 eV, while the "large" clusters (n = 16-25) shown in (b) have a sharper rise near the Fermi level with weaker density between 2-3 eV.

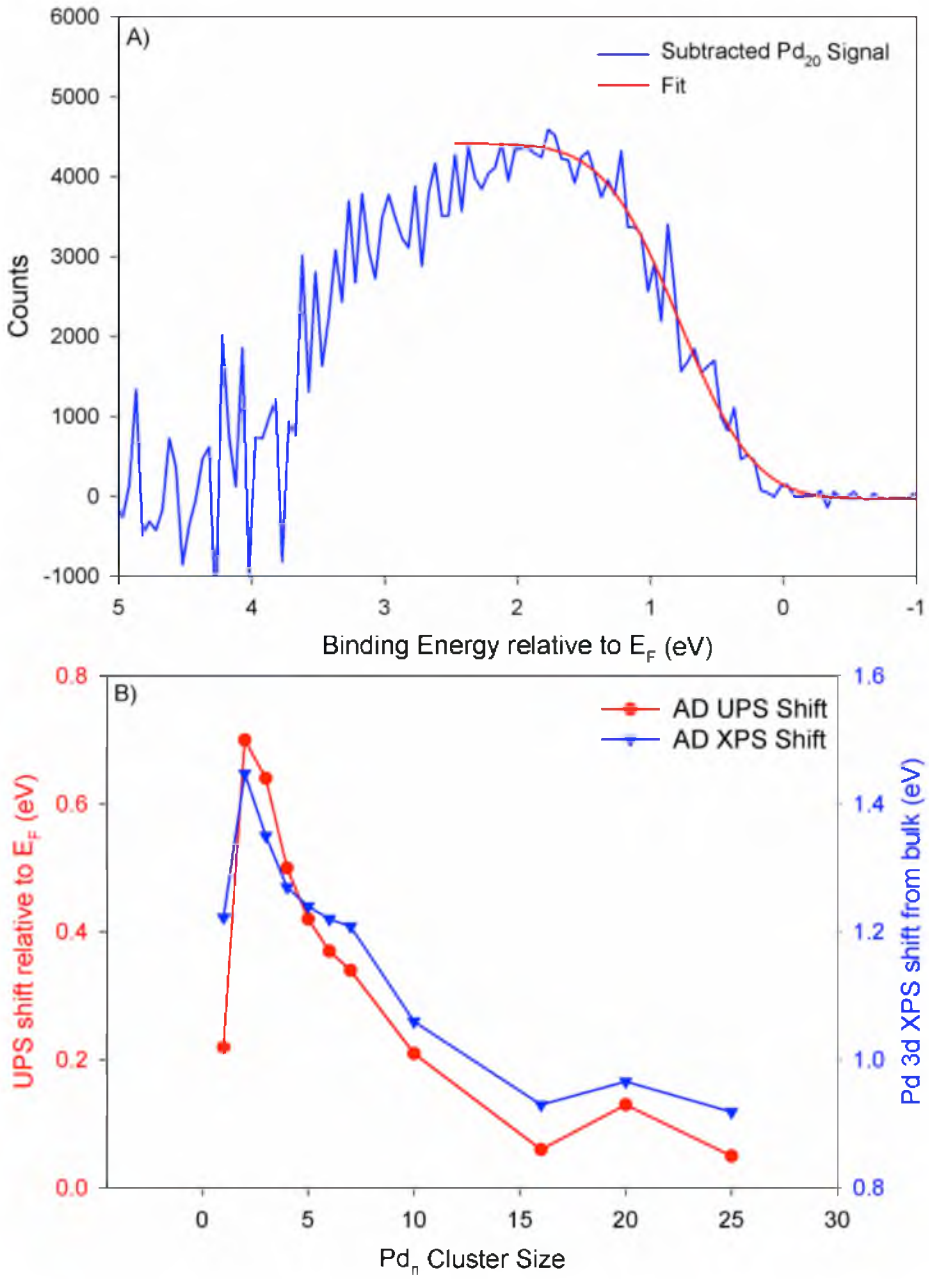

Figure 3.3 With the TiO_2(110) UP spectrum subtracted out of the Pd_n/TiO_2(110) UP spectrum, the remaining signal from the Pd cluster can then be fit (a) in order to determine the shift of the band below the Fermi level. The valence and core level shifts are plotted together in (b) showing a similar trend between the two, with the shifts moving towards the Fermi level until cluster n = 16 where the shifts level off.

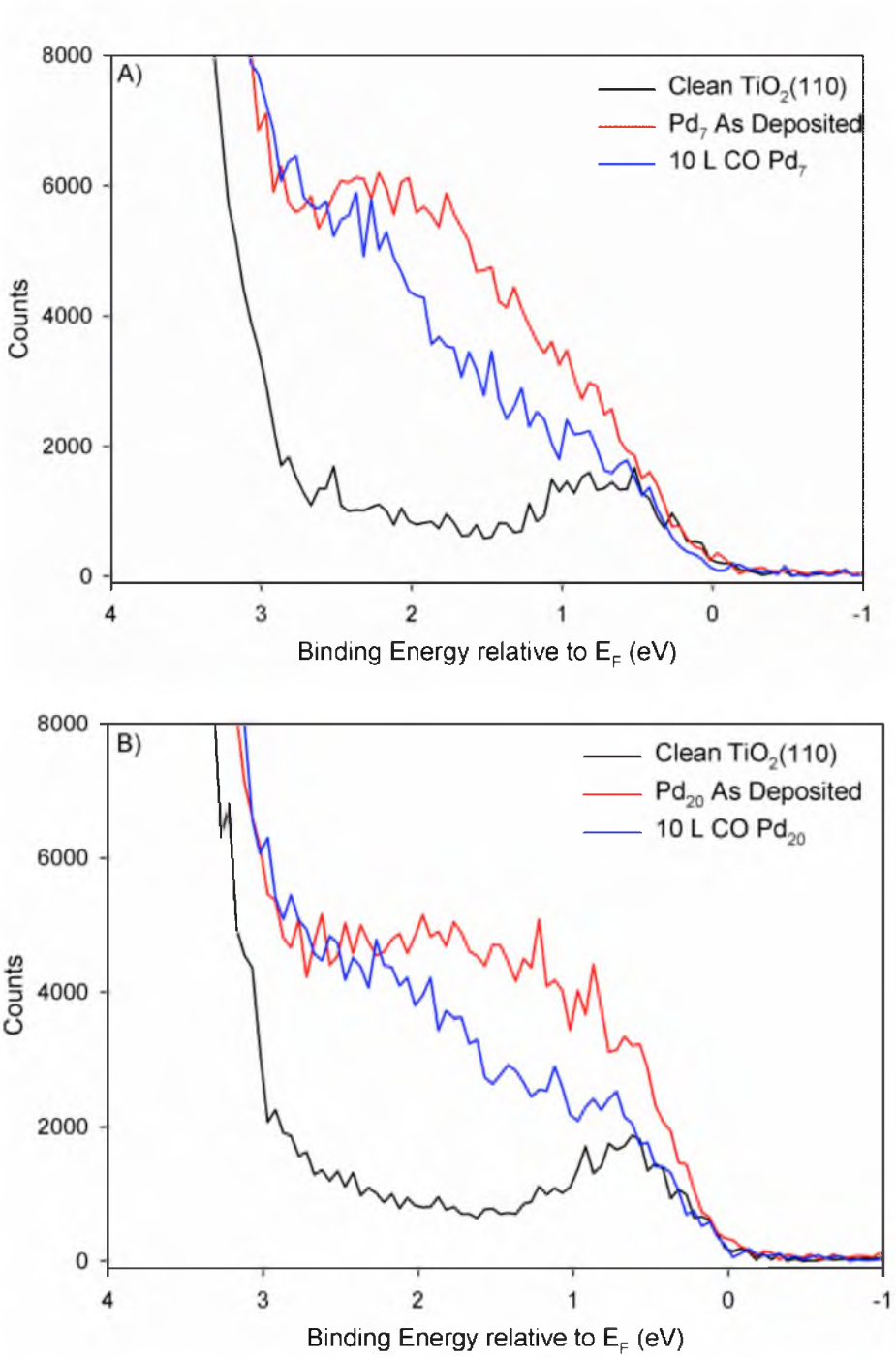

Figure 3.4 UP spectra of as deposited Pd_7 and after a 10 L CO exposure are shown in (a), with the CO dose causing an attenuation of the signal nearest the Fermi level. A similar result for Pd_{20} is shown in (b), and in both cases, the Pd DOS is only affected at energies less than 2.5 eV.

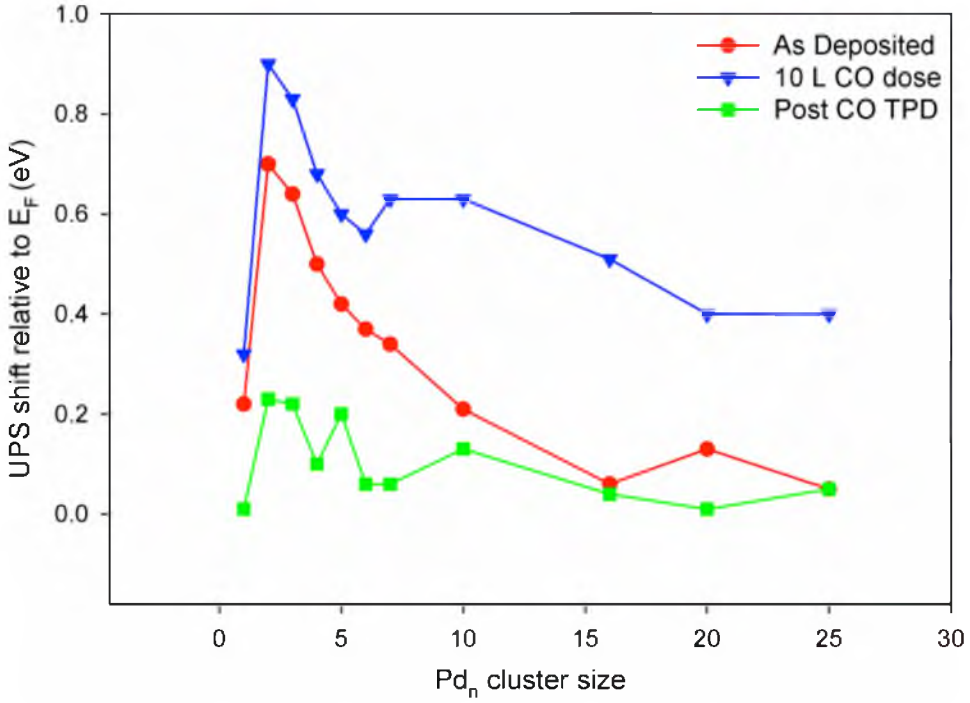

Figure 3.5 UPS shifts below the Fermi level for the as deposited clusters (red), the clusters after a 10 L CO dose (blue), and post CO TPD (green).

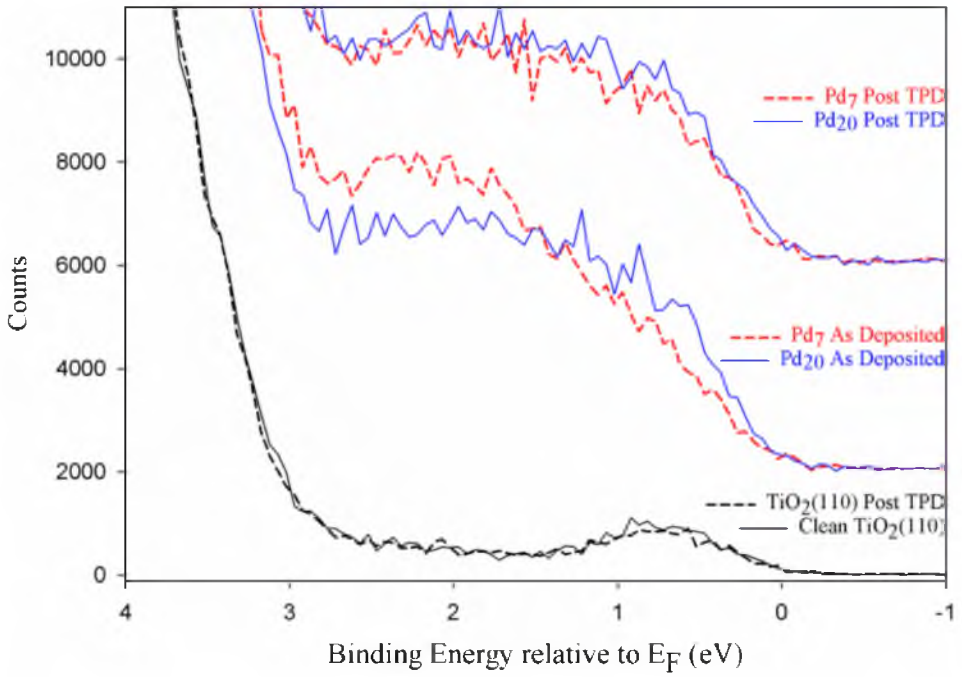

Figure 3.6 UP spectra for Pd_{20} (solid blue) and Pd_7 (dashed red) as deposited and after a CO TPD. The solid black and dashed black lines in the bottom set of spectra are for pristine TiO_2(110) before and after a CO TPD, respectively.

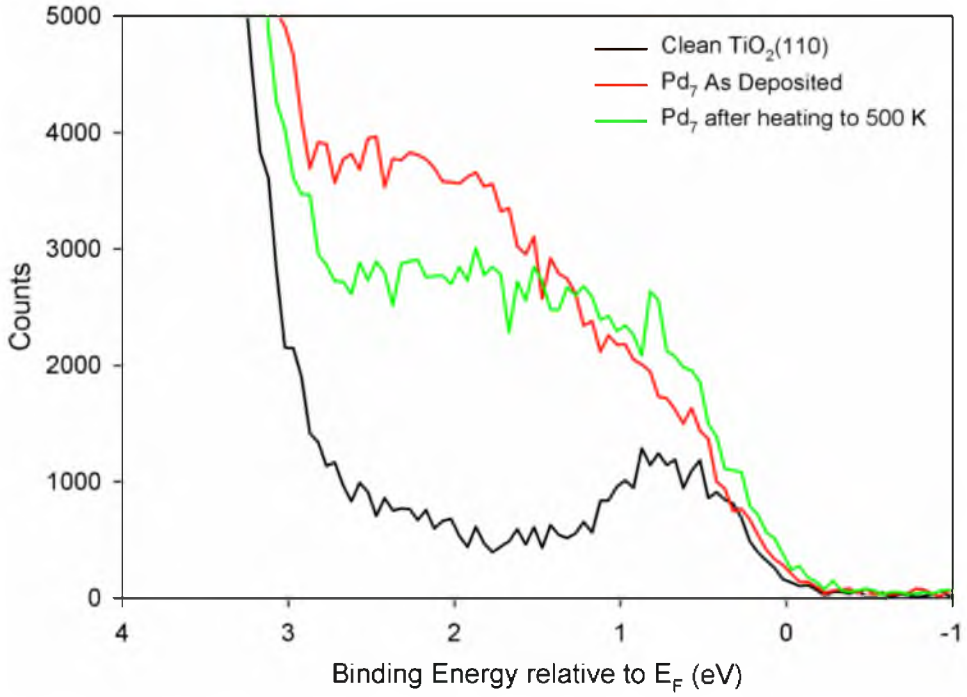

Figure 3.7 UP spectra for clean $TiO_2(110)$ (black), Pd_7 as deposited (red), and Pd_7 after heating to 500 K at 3 K/sec (green). Notice the change in shape to resemble a "larger" cluster after heating.

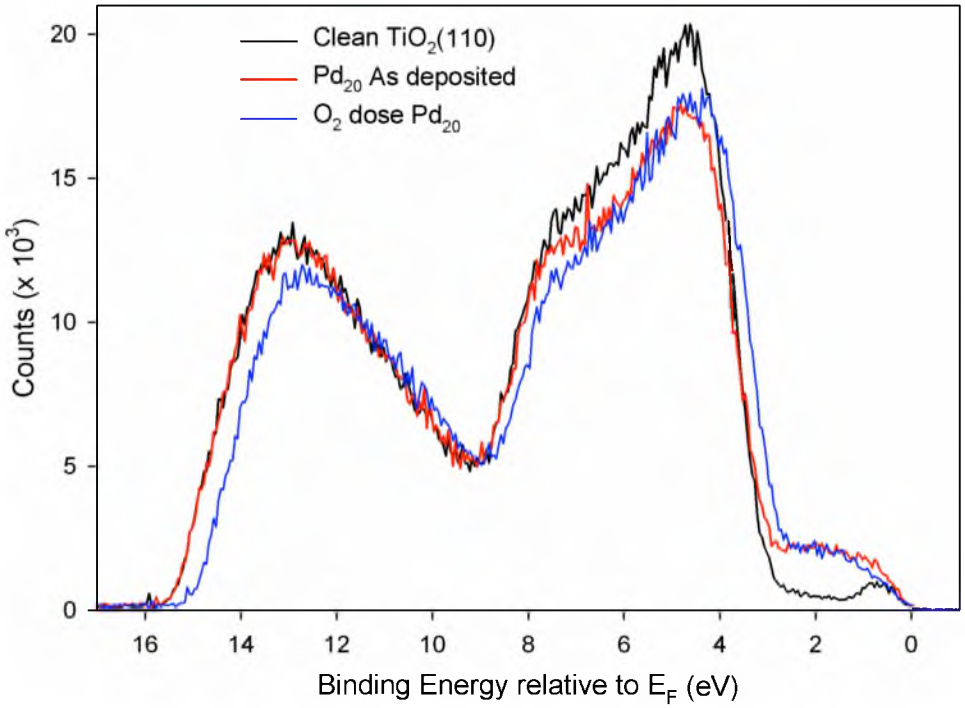

Figure 3.8 UP spectra showing the effect of oxidation on $Pd_{20}/TiO_2(110)$. The clean $TiO_2(110)$ spectrum is shown in black with the as deposited Pd_{20} shown in red followed by oxidation at 400 K with the subsequent spectrum shown in blue. Notice the shift in the high binding energy cutoff and O 2p feature after oxidation.

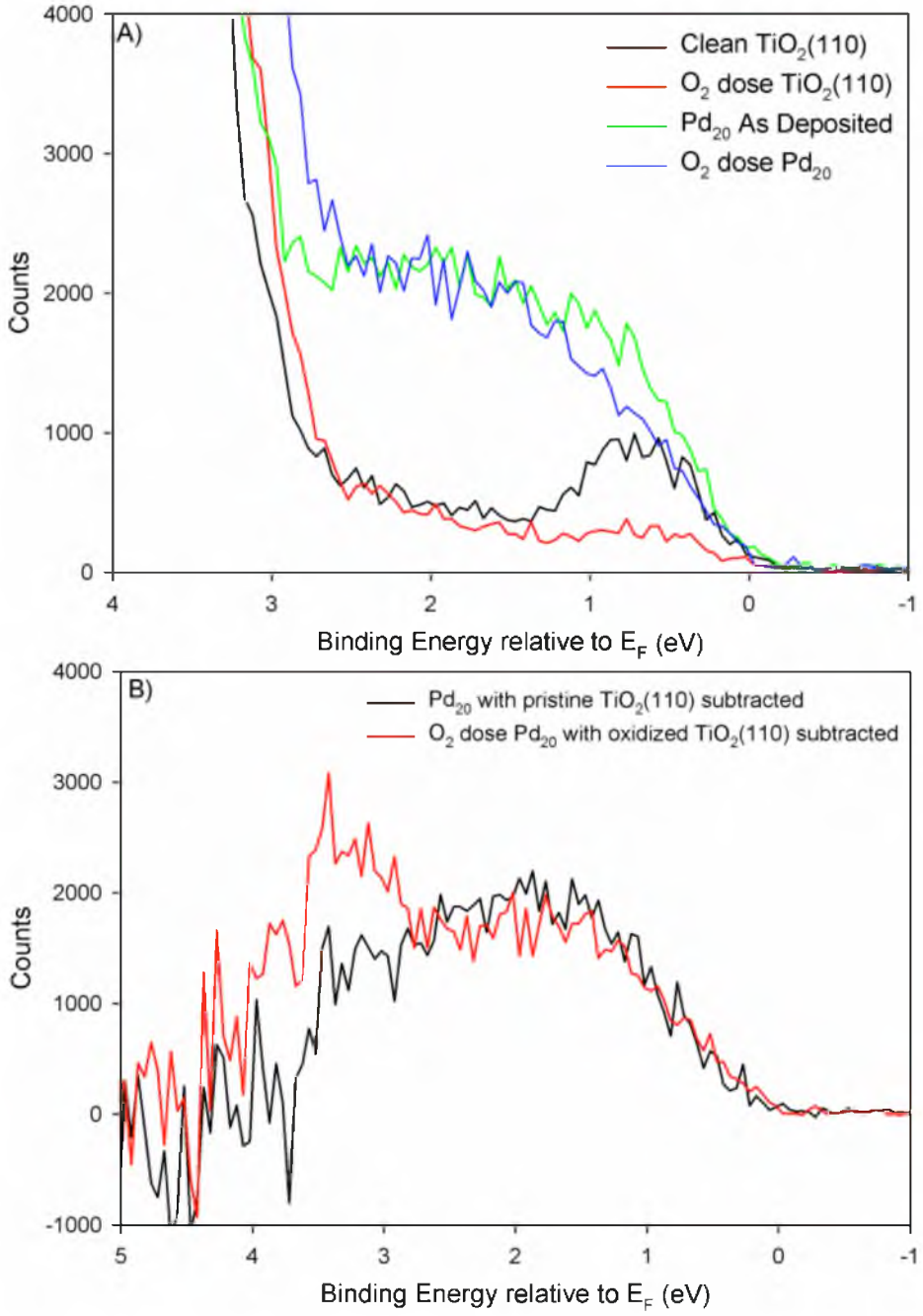

Figure 3.9 UP spectra of Pd_{20} and $TiO_2(110)$ before and after oxidation are shown in (a). The subtractions are shown in (b) with the pristine $TiO_2(110)$ subtracted from the unoxidized Pd_{20}, and the oxidized $TiO_2(110)$ subtracted from the oxidized Pd_{20}. The signal at about 3.5 eV in the oxidized subtraction is due to a slight shift in position of the O 2p valence band as shown in Figure 3.8.

CHAPTER 4

THE IMPORTANCE OF VALENCE ELECTRONIC STRUCTURE FOR THE CO OXIDATION REACTION EFFICIENCY OVER SIZE-SELECTED $Pt_n/Al_2O_3/Re(0001)$ MODEL CATALYSTS

4.1 Introduction

Fundamental research in heterogeneous catalysis focuses on answering the basic question of what controls catalyst reactivity. It is well known that different noble metals catalyze reactions differently in terms of efficiency, selectivity, etc., but varying the size of the *same* metal clusters also plays a very important role in the catalyst behavior.[1-6] Oftentimes fundamental research tries to study these phenomena by simplifying the system and solving the problem piecewise using "model" catalysts. Model catalysts typically consist of small noble metal clusters (ideally with a narrow size distribution) deposited on a well-characterized single crystal support. With the surface well controlled and ordered, standard surface analysis techniques can then be used to determine attributes of the catalyst such as the location of binding/active sites, the physical/electronic structure of the clusters, etc. Since the CO oxidation reaction has been extensively studied[7-31] and is a relatively simple reaction, it is a good system to use in order to probe the chemical properties of different catalytic systems, and it allows for easy comparison between model catalysts.

While there have been many studies on the catalytic activity of Pt group metals, including both applied[18, 21, 32-38] and fundamental[1, 3, 38-54] research, questions still remain. The most interesting and pertinent questions arise when considering the effect cluster size plays in determining reactivity. There have been many fundamental studies on Pt group single crystals and supported nanoparticles, but there is some evidence showing the most active and interesting cluster regime is < 1nm in size where small size fluctuations have a large impact on catalyst activity. Our group and others have shown that metal clusters in this size range exhibit some interesting and unexpected catalytic behavior, mainly

improved catalytic activity compared to the bulk.[4, 6, 39, 42, 44, 47, 55-66] Furthermore, in attempting to unravel the effects that make this size range behave so differently, it is starting to become clear that there is an important interplay between the electronic structure controlling not only the physical structure of the cluster on the surface, but also the ability of that cluster to catalyze reactions.

Here we report a study of a model catalyst system consisting of small Pt_n (n=1,2,4,7,10,14,18) clusters supported on thin alumina films grown on Re(0001). Controlling the size of the noble metal catalyst with atomic resolution allows us to investigate how even the smallest size step affects catalyst activity. X-Ray/ultraviolet photoelectron spectroscopy (XPS/UPS) were used to determine the electronic structure of the alumina film and the Pt_n clusters, and temperature-programmed reaction/desorption (TPR/TPD) was used to determine the availability and density of binding sites. Recently, our group has shown that fluctuations in core level binding energies of Pd clusters supported on TiO_2(110) correlate strongly with the reactivity in the CO oxidation reaction.[6] Additional work on the same system suggested that oxidation was an "activated" process and the electronic structure fluctuations seen with XPS are actually determining how efficiently the clusters activate oxygen.[59]

4.2 Experimental Methodology

The ultrahigh vacuum (UHV) chamber (base pressure < ~2 x 10^{-10} Torr) and cluster deposition beamline have been described previously.[55, 67] Briefly, the UHV chamber allows for *in situ* sample preparation and is equipped with several surface analysis techniques such as mass spectrometry for temperature-programmed

reaction/desorption (TPR/TPD), low energy ion scattering (ISS), X-Ray photoelectron spectroscopy (XPS), and ultraviolet photoelectron spectroscopy (UPS). Our model catalyst is constructed on a rhenium(0001) single crystal (Marketech International) that is attached to a liquid nitrogen-cooled cryostat with a C-type thermocouple spot welded to the back of the crystal to monitor the temperature. The sample can be cooled to 100 K, and heated to 1200 K resistively, or to >2200 K via electron bombardment from the back side.

The high temperatures needed to clean and anneal the Re(0001) sample require use of a type C thermocouple; however, the sensitivity of type C thermocouples below 200 K is poor. Our experience with commercially available type C vacuum feedthroughs, which are made using "extension" alloy rather than the actual W-5%Re/W-26%Re thermocouple composition, was poor at low sample temperatures. Therefore, we fabricated our own feedthrough by drilling out the extension alloy pins, and cementing in 1 mm diameter pins made from actual type C material. Eliminating the extension alloy feedthrough substantially improved the repeatability of the low temperature measurements; nonetheless, we feel that temperature measurements below 200 K may have absolute error of up to ~10 K.

Typical sample preparation first involves cleaning and annealing the Re(0001) single crystal by heating to high temperatures to decompose and desorb any adsorbates, as well as creating a well-ordered crystal surface. Our procedure, adapted from those developed in the Goodman[68-70] and Madey[71, 72] groups, is to heat the sample via electron bombardment to 1850 K for 4.5 minutes, followed by a flash to 1950 K for 0.5 minutes. XPS and ISS show a surface free of contaminants (save for a very small amount of

oxygen), and low energy electron diffraction (LEED) analysis by Goodman and Madey have determined that the resulting surface is well ordered.

After annealing the crystal and ensuring its cleanliness, the sample is inserted and sealed into an antechamber where the Al_2O_3 thin film is grown. The antechamber (base pressure ~5 x 10^{-10} Torr) allows procedures requiring high pressures to be carried out without affecting the pressure in the main surface analysis chamber. The method used here follows very closely to those used by Goodman[68-70] and Madey[71, 72] which were shown to result in epitaxial alumina films with crystalline structure as shown by LEED. The Re(0001) substrate is resistively heated to 970 K and 5 x 10^{-6} Torr of O_2 is leaked into the antechamber, resulting in no measureable change in the main chamber pressure. A resistively heated 99.999% purity alumina crucible filled with aluminum (ESPI Metals, 5N purity) is mounted normal to the Re(0001) surface and brought to the desired temperature for aluminum evaporation. Once the evaporation rate is established, the sample is lowered into position in front of the aluminum source. Growth rates were typically between 0.2 and 0.3 nm/minute, as determined by XPS analysis of the Al/Re intensity ratio, and films were grown to thicknesses between 3 and 6 nm, also determined via XPS. We have previously shown that for films in this thickness range, both the electronic structure of the film (i.e., Al and O XPS binding energies), and the catalytic activity and valence band structure of clusters deposited on it, are independent of thickness.[63] In all experiments, XPS was performed after alumina growth both to measure the film thickness, and to verify that the Al and O binding energies appeared normal for alumina.

To minimize contamination or damage effects, studies of reactivity were performed on separately prepared samples from those examined by UPS or ISS. For the reactivity experiments, the sample was cooled to ~140K immediately after XPS of the alumina film, then flashed to 650K to desorb any species that might have adsorbed during the ~20-minute cool-down time (mainly water). As the sample cooled after the flash, deposition of Pt_n was started as soon as the sample reached room temperature (<3 min), continuing until the desired coverage was reached (3 – 15 min). Deposition was started during cooling in order to minimize the exposure of the cold sample to adventitious adsorbates, as discussed below. The cluster neutralization current was measured continuously during deposition, and used to determine when deposition should be terminated to give consistent Pt coverage. For all the experiments here, the coverage was 1.50×10^{14} Pt atoms/cm^2 (10% of a close-packed Pt monolayer) deposited in the form of different size Pt_n, at a deposition energy of ~ 1 eV/atom. During deposition, the sample was positioned just behind a 2 mm diameter exposure mask, in order to have consistent spot diameters.

To study CO oxidation, the freshly prepared Pt_n/alumina sample was positioned 2.0 mm away from the 2.5 mm diameter orifice in the skimmer cone of our differentially pumped mass spectrometer. The surface was then exposed to 10 L of $^{18}O_2$ at $T_{oxidation}$ of either 300 K or 180 K, and then exposed to 10 L of ^{13}CO at 180 K, before cooling to the 140 K starting temperature for TPR. The 180 K CO dose temperature was chosen to minimize reaction with pre-adsorbed oxygen during the CO dose, and also to allow comparison of the results for Pt_n/alumina/Re(0001) with previous studies of $Pd_n/TiO_2(110)$[6] and Pd_n/alumina/Ta(110)[63]. In those systems, CO binding to the oxide

support becomes a problematic source of background if the CO dose is done at lower temperature. This issue is discussed in detail below.

To improve sensitivity for desorbing species, the sample was moved to a position 1.0 mm from the skimmer cone, and then its temperature was then ramped at 3 K/sec to 650 K while signals were monitored for the $^{13}C^{18}O^{16}O$ product, the unreacted ^{13}CO, and for species such as water, unlabeled CO, or CO_2 isotopologs that might form from reaction with adventitious CO or ^{16}O from the alumina film. This same process (oxidation, CO dose, heat ramp) was carried out two more times to observe the effects of multiple TPRs on the clusters, and then followed by a final CO TPD (no intermediate oxidation step) as a probe of the density of CO binding sites remaining after the series of TPR runs as well as to determine if any active oxygen remains after reaction. The $T_{oxidation}$ = 300 K and 180 K series of TPR/TPD experiments were done on separately prepared sets of samples, and another fresh set of Pt_n/alumina samples was used for a series of CO TPD experiments to probe the density of CO binding sites on the as-deposited clusters. In those experiments, the same protocol was followed for alumina film growth, cooling, and cluster deposition, but the samples were dosed only with ^{13}CO (10 L at 180 K) with no prior oxidation step.

The electronic properties of the as-deposited clusters were probed by a combination of XPS and UPS, done on yet another separate set of Pt_n/alumina samples, to avoid effects on the reactivity studies from X-ray or UV damage, or from adventitious contaminants. In these studies, both XPS and UPS were performed immediately after alumina film growth, and then the samples were cooled to 140 K, flashed to 650 K, and decorated with Pt_n using the same protocol used in the reactivity studies. XPS and UPS

were recorded again immediately after deposition to probe the electronic properties of the freshly deposited Pt_n. The UP spectra were collected using a homebuilt VUV light source that has been described elsewhere,[73] and the sample was biased to -15.0 volts in order to resolve the high binding energy cutoff (low kinetic energy electrons) for sample work function determination. In the figures below, the binding energy (BE) scale is referenced to the Fermi level (E_F) of the clean rhenium sample, with zero BE taken as the inflection point of the steeply rising rhenium signal. The effects of charging on the Al, O, and Pt spectra appear to be small, as judged by peak widths that are essentially independent of alumina thickness, for the 3 – 6 nm range used here. Charging becomes obvious for thicker films.

As shown below, the UP spectrum of the clean alumina has only weak signal in the energy range between E_F and the onset of the O 2p band at ~ 4 eV (i.e., in the bandgap). Therefore, Pt-derived signal in this energy range is easily extracted by subtracting the small and featureless contribution from alumina. The resulting subtracted Pt signal is well fit using a step function, convoluted with a Gaussian, and the onset of the Pt signal is estimated by extrapolating the slope at the inflection point to baseline, similar to procedures used by Parkinson and Schlaf.[74, 75] Samples prepared with these small Pt clusters have no density of states (DOS) at E_F, thus one point of interest is comparing the size-dependent shifts in the Pt band onset energy with CO oxidation activity, i.e., looking for correlations between metal electronic and chemical properties. Such correlations have been shown using XPS to probe core levels for Pd_n/TiO_2[6] and Pd_n/alumina[63] and we have also shown that the valence and core level shifts are similar in Pd_n/TiO_2.[76]

It is useful mechanistically to be able to relate the ion signals observed during TPD and TPR experiments, to the absolute number of the corresponding molecules desorbing from the surface. The following approach was used. The sample was moved away from the mass spectrometer skimmer orifice, and various pressures of gases of interest (CO, CO_2, Ar), were leaked into the main chamber via a leak valve that is remote from the mass spectrometer, with pressures measured using two different ionization gauges in the main chambers. The ion gauge readings were corrected using molecular sensitivity factors provided by the manufacturer to obtain estimates of the actual pressures. Given the 2.5 mm diameter skimmer orifice, it is straightforward to calculate the flux of molecules effusing into the TPD/TPR mass spectrometer, and the ratio of this flux to the corresponding ion count rate gives the overall detection efficiency for each of the molecules of interest. Because molecules effusing through the orifice should have cosine angular distributions, which are also typical of molecules thermally desorbing from surfaces (unless there is repulsion as the product desorbs along the dissociation coordinate), we need only account for some geometric factors in order to obtain the equivalent detection efficiency for molecules desorbing form the surface.

Because the cluster spot (2 mm dia.) is smaller than the 2.5 mm orifice, the effective source area for the cluster sample is ~40% smaller than that in the gas phase calibration experiment. In addition, however, to avoid any possibility of scratching the single crystal sample, we normally do TPR/TPD with the sample positioned 1 mm from the skimmer orifice. As a result, some molecules desorbing from the cluster spot will tend to miss the orifice, adding another geometric factor to the calibration. A few CO TPD measurements were made with the sample carefully moved forward until it nearly

touched the orifice, resulting in a near-doubling of the desorption signal. Both the spot size and sample-orifice distance factors are included in the conversion from ion signal to molecular fluxes, discussed below. Finally, to correct for factors such as drifting electron multiplier gain that might cause day-to-day variations in sensitivity, we perform a simplified version of this calibration every day, using only argon. We estimate that desorption fluxes determined from the calibration should be within ± 50% of the true values, with uncertainty due to a combination of factors such as ion gauge absolute calibration, and deviation of the actual desorption angular distributions from the assumed cosine form. The calibration is in reasonable agreement with a previous desorption flux calibration done using desorption of saturated monolayers from Ni (100) or Pd(111).

4.3 Results

4.3.1 Size-dependent CO_2 Production

For the $^{18}O_2$ + ^{13}CO reactants used in these experiments, the two main desorption channels are $^{13}C^{18}O^{16}O$, i.e., the expected CO oxidation product, and unreacted ^{13}CO. Typical desorption spectra for these two mass channels are shown in Figure 4.1 for both alumina/Re(0001), and Pt_7/alumina/Re(0001). In both cases, the samples were first exposed to 10 L $^{18}O_2$ at $T_{oxidation}$ = 300 K, and then to 10 L ^{13}CO at 180 K. From the comparison, it is clear that there is no significant background at either the reactant or product masses from adsorption/reaction on the alumina film. We also looked for desorption of residual $^{18}O_2$; however, none was observed in the temperature range up to 700 K for any of the samples. Slight water contamination (both mass 18 and 20) from the background vacuum was detected during the TPDs. The amount is small (less than half

the amount of CO_2 produced) and independent of Pt_n coverage or size as the same amount is present on a bare alumina film and Pt_n/alumina. The only other isotopomer detected was $^{13}CO_2$ (mass 45) as a second reaction product which will be discussed later.

Desorption of residual, unreacted ^{13}CO from the Pt_7/alumina sample is bimodal, with a relatively small and sharp peak at ~190 K which will be referred to as the *low temperature* (LT) peak, and a larger and broader peak at ~520 K which will be referred to as the *high temperature* (HT) peak. ^{13}CO desorption is observed immediately upon starting the heating ramp at ~140 K, even though the CO dose was delivered at 180 K. This low temperature desorption reflects adsorption of background ^{13}CO remaining after termination of the CO dose, during cooling to the 140 K TPR/TPD starting temperature. The integrated exposure during cool down is estimated to have been only 0.3 L; however, sticking under these conditions can be quite efficient due to substrate-mediated adsorption (i.e., reverse spillover).[56, 61, 78, 79] Because the CO desorption *below 180 K* is expected to be strongly dependent on amount and temperature profile of the ^{13}CO exposure during sample cooling,[63] we restrict our discussion of the LT CO desorption peak only to the desorption occurring above 180 K.

CO_2 production is detected over a wide range over temperatures, with the majority desorbing around 300 K, in between the bimodal ^{13}CO desorption features. The onset of CO_2 desorption is at ~180 K, i.e., at the CO dose temperature. The absence of CO_2 desorption at temperatures below the CO dose temperature is expected, because any adsorbed oxygen and CO capable of reacting at lower temperatures should have reacted away during the CO dose. To test this conclusion, we compared the CO_2 product desorption temperature dependence for identical Pt_7/alumina/Re(0001) samples, where

the CO exposure was done at either 180 K, or 140 K. As expected, in the latter case, during the TPR heat ramp, CO_2 product desorption started at ~140 K. Also, as expected, the magnitude of the LT CO desorption peak was substantially larger.

The question, therefore, is how much CO_2 production occurs during the CO exposure, i.e., how much is missed in the TPR results. During all ^{13}CO (and $^{18}O_2$) exposures, the sample is positioned 2 mm from the mass spectrometer skimmer orifice, and signals for all masses of interest, including $^{13}C^{16}O^{18}O$, are monitored during reactant exposures. As the above results suggest, $^{13}C^{16}O^{18}O$ signal is observed during the ^{13}CO exposure, but only during the first ~ 100 msec of the 1 minute 40 second exposure time, indicating that there is a small amount of adsorbed ^{18}O that is reactive at 180 K, but that it is quickly reacted away. Because this $^{13}C^{16}O^{18}O$ signal duration is so short, it is difficult to estimate the amount produced during the 180 K CO dose; however, it is clearly < 5% of the amount $^{13}C^{16}O^{18}O$ produced during the subsequent TPR heat ramp. The 180 K CO dose temperature was chosen to allow direct comparison of the Pt_n/alumina/Re(0001) results with analogous results for Pd_n/alumina/Ta(110),[63] and Pd_n/TiO_2(110).[6] In the latter system, use of a lower CO dose temperature would have resulted in a large background from CO adsorbing on the oxide support.

Figure 4.2 shows how desorption of both unreacted ^{13}CO and $^{13}C^{18}O^{16}O$ product vary with deposited cluster size. These data are for the first TPR run made after 10 L $^{18}O_2$ exposure at $T_{oxidation}$ = 300 K, followed by 10 L ^{13}CO exposure at 180K. Analogous data for ^{13}CO and $^{13}C^{18}O^{16}O$ desorption in the first TPR run taken on a separately prepared set of samples, where 180 K was used for both the $^{18}O_2$ and ^{13}CO exposure temperatures, show very similar results which will be discussed later. Residual ^{13}CO

(Figure 4.2a) desorbs with a bimodal temperature dependence in all cases; however, the relative intensities of the LT and HT peaks are size-dependent. In particular, samples prepared with Pt_1 and Pt_2 have high LT peak intensities, and relatively low HT peak intensities. For larger clusters, the LT intensities are generally smaller, and the HT peaks are similar, and significantly larger than those for Pt_1 and Pt_2. These could be due to differences in the distribution of CO binding sites, or to size-dependent differences in reactivity to form CO_2.

The $^{13}C^{18}O^{16}O$ production is indeed strongly dependent on cluster size (Figure 4.2b). For all sizes, $^{13}C^{18}O^{16}O$ is observed in a broad peak between 180 and 600 K, reaching a maximum at ~350 K, which is near the minimum between the two CO desorption peaks. The breadth suggests that reaction occurs with a wide range of activation energies, which is not surprising considering that these supported cluster samples presumably have a variety of CO and oxygen binding sites, that site hopping/diffusion may be necessary to bring the reactants together, and that the coverage of one or both reactants varies substantially during the TPR. It is interesting that while the peak intensity is strongly dependent on cluster size, the temperature dependence is essentially independent of size. This suggests that it is the number density of binding sites that changes with cluster size (peak intensity), not how strongly the CO and O is bound to the cluster (peak temperature/energy). Quantitative estimates of the amounts of CO and CO_2 desorbing are discussed below.

We also monitor desorption of other CO_2 isotopomers during the $^{18}O_2$ and ^{13}CO exposures, and during the subsequent TPR runs. Weak signal for $^{12}C^{16}O^{18}O$ (mass 46) is observed during the $^{18}O_2$ dose, which we attribute to $^{18}O_2$ reacting with adventitious

normal CO adsorbed on surfaces in the instrument, including the walls of the mass spectrometer differential pumping cone, the inside of the oxygen dosing tube, as well as the sample itself. In fact, because the samples were flashed to remove CO just before cluster deposition, the time available for adventitious CO adsorption, prior to the $^{18}O_2$ dose, was only 3 to 15 minutes, thus we believe that wall reactions were the dominant source of mass 46 signal. We separately investigated sticking and desorption of CO_2 on several Pt_n/alumina/Re(0001) samples, and saw no sticking in the temperature range of interest (140 K to 700 K). Therefore, the small exposure of the sample to $^{12}C^{16}O^{18}O$ during the $^{18}O_2$ dose should have no effect, and as expected, mass 46 is not observed during TPR.

On the other hand, the $^{13}C^{16}O^{16}O$ isotopic product (mass 45), is observed to desorb during each TPR, with temperature dependence identical to that for the main product, $^{13}C^{18}O^{16}O$, and with intensity that ranges from 13% to 28% of the total CO_2 product intensity. The dependence of this mass 45 signal on cluster size is also quite similar to the dependence of the main mass 47 peak, thus we believe that this mass corresponds to real reaction of adsorbed ^{13}CO with ^{16}O on the surface. From the 2-5% ^{16}O impurity level in the $^{18}O_2$, we would expect a similar fraction of mass 45 in CO_2 product, but there obviously must be some other source of ^{16}O, accounting for the rest of this product. The alumina film is grown with ^{16}O, and is an obvious source. In addition, the high O_2 pressures used for alumina growth result in an elevated $H_2{}^{16}O$ background, however, since the alumina is grown in a separate chamber, the effect on the main chamber is minimal. Furthermore, the amount of mass 45 signal is not correlated with the exposure time of the sample to the UHV background, thus it appears that there is

some ^{16}O available from the alumina support. In this regard, we note that the amount of mass 45 signal is roughly constant in sequential TPRs, and that ISS shows no evidence ^{18}O remaining on the surface after the series of experiments, suggesting that ^{16}O-^{18}O exchange in the alumina film is not significant, unlike what is observed under similar conditions for Pd_n/TiO_2. Regardless of the source, because the cluster size and temperature dependence of the mass 45 desorption is similar to those for the main mass 47 product, we simply add the small mass 45 contribution to the mass 47 signal in calculating the integrated production.

Figure 4.3a shows this integrated residual CO desorption as a function of cluster size for $T_{oxidation}$ = 300 K, and Figure 4.3b gives analogous results for CO_2 production (mass 45 + 47). There is no obvious size dependence for the total amount of residual CO desorbing during a TPR as the integrated area only fluctuates by ~20%. There are some other interesting features, such as the difference in intensities between the 1st and 2nd TPR and the effect of oxidation; these will be discussed in more detail later. For now, the focus is on the CO_2 production in order to determine if Pt_n cluster size plays a role in controlling CO oxidation activity. When looking at the CO_2 production in Figure 4.3b, it is obvious that there is indeed strong cluster size dependence for CO oxidation efficiency as the areas differ by as much as an order of magnitude between clusters for the first TPR. With the exception of samples prepared by deposition of Pt atoms, the trend is for CO oxidation activity to increase with increasing deposited Pt_n size, leveling off or perhaps decreasing slightly for the largest size studied. Both the magnitude of the CO_2 production and its dependence on cluster size, are quite similar for $T_{oxidation}$ = 180K and 300 K. The small fluctuations in the cluster size trend (e.g., Pt_9 for 2nd and 3rd TPR) are

not thought to be significant, and are attributed to the effects of small variations in experimental conditions. To that point, it is worth noting that given the complexity and time consumption of performing these experiments, the activity of each cluster size was only measured once for each temperature. The very small change in CO_2 production between the 2nd and 3rd TPRs gives us confidence in our reproducibility for TPRs performed on the same day, and the two different oxidation temperatures (taken on different days, and in a different cluster size order) shows the overall activity trend is reproducible.

It is interesting to compare the CO oxidation behavior over Pt_n/alumina/Re(0001) with other systems we have studied under identical conditions, including Pd_n/alumina/Ta(110) system,[63] and $Pd_n/TiO_2(110)$.[6] The three systems are similar in that desorption of unreacted CO has a bimodal temperature dependence, while CO_2 is largely evolved in a broad feature at intermediate temperatures. The CO oxidation activities and dependences on cluster size and $T_{oxidation}$ all vary considerably between the three systems, however. For the Pt_n/alumina/Re(0001) system, between 8 % and 50 % of the adsorbed CO is oxidized to CO_2, with activity generally increasing with cluster size, with the exception of the samples prepared with Pt_1. For Pd_n/alumina/Ta(110), the oxidation efficiency ranges from 25 to 35%, with weak but nonmonotonic dependence on cluster size, peaking at Pd_6; and for $Pd_n/TiO_2(110)$, the efficiencies range from 0 to ~10%, with nonmonotonic size dependence with local maxima at Pd_2 and Pd_{20}, and Pd_1 being totally unreactive. For the Pd_n/TiO_2 system, the activity and size dependence are strongly dependent on $T_{oxidation}$, with all but Pd_1 active for $T_{oxidation}$ = 400K, only select sizes active for $T_{oxidation}$ = 300 K, and none active at 200 K.[6] This pattern suggested that there were

significant, and size-dependent energy barriers for O_2 activation on Pd_n/TiO_2. For Pd_n/alumina/Ta(110) system,[63] the CO oxidation activity was significantly lower for $T_{oxidation}$ = 180 K, compared to 400 K, but with weak size dependence. In the present, Pt_n/alumina system, the activities and size dependence are nearly identical for $T_{oxidation}$ = 180 K and 300 K, suggesting that there are not significant energy barriers to O_2 activation.

Figure 4.3 also shows how the integrated CO oxidation activity changes in the second and third TPR run on each sample, under identical conditions. Note that the cluster size dependence is substantially flattened in the second TPR, compared to the first, but that there is little additional change in the third run. The activity for the smaller, initially less active clusters increases so that these samples are nearly as active as those prepared with large clusters. Such behavior suggests that adsorbate binding and heating of the samples may cause sintering, restructuring, or broadening of the initially deposited cluster size distribution.

The obvious exception to the trend of increasing activity with increasing deposited cluster size are the samples prepared by deposition of Pt_1, which are significantly more active than the trend would suggest. The CO oxidation activity for Pt_1 is similar to that of samples prepared by deposition of medium size clusters in the Pt_7 size range. This high activity for samples prepared by atomic ion deposition is in contrast to most other systems where we have studied CO oxidation under conditions similar to those used here, where deposited atoms have been found to be completely inactive, or at least less active than any of the larger clusters.[5, 6, 55, 80, 81] Again, the unexpectedly high activity of deposited atoms may imply that they sinter to form clusters, even in the

sample with $T_{oxidation}$ = 180 K, where the deposition and reactant exposures were all carried out below room temperature. Enhanced sintering of isolated atoms (compared to preformed clusters on the surface) is common and reflects the fact that for a preformed cluster to diffuse, more bonds must be broken simultaneously than are required for diffusion of ad-atoms on a support. As shown below, samples prepared by atom deposition also show other anomalous behavior; however, only some of this anomalous behavior can be rationalized by assuming that deposited atoms sinter readily.

4.3.2 CO Desorption Trends

Investigating the integrated area of the residual CO desorption, it is clear the size dependence does not follow that for CO_2 production. For each cluster size, there is more CO desorbing during the first TPR and decreases slightly to the 2nd and 3rd TPR, while the CO_2 production increases for the small clusters and remains unchanged for the large clusters. These different desorption trends suggest the CO_2 production is not being controlled by the amount of CO the system can adsorb. Looking at the details of the integrated area and temperature dependence for CO desorption, it becomes clear that the CO desorption changes drastically under different conditions. This is especially true of oxidation, oxidation temperature, and TPR cycle (as mentioned above) and the details will be presented below.

The integrated area of the unreacted CO desorbing from the surface (see Figure 4.3) does not show a very strong size-dependent trend and the area as a function of cluster size only fluctuates by about 15-20%. For all clusters, the first TPR shows the most amount of CO desorbing as compared to the second and third TPR cycles, and the

final CO TPD is even stronger by about 20%. The most notable change is the relative ratios of the LT and HT CO desorption peaks. The unreacted CO desorbing during the second TPR sees the HT peak decrease in intensity while the LT peak remains fairly constant to where the two peaks are now nearly equal in size. The third TPR sees no real change in the CO desorption pattern, as is the case with the CO_2 production. If the intensity of the LT and HT peaks are plotted as a function of cluster size, there is a very clear inverse relationship between the size of the HT and LT peaks, and the loss of the HT peak intensity between TPR runs is very clear (see Figure 4.4). The change in the HT CO peak along with changing CO_2 production upon multiple cycles points to the importance of this peak, and more analysis of the relationship between the HT CO peak and CO_2 reveals some interesting results which will be discussed later. Following the three TPR cycles, a final CO TPD was conducted to determine the availability of the final state CO binding sites. Compared to the residual CO desorbing in the final (third) TPR, the overall amount of CO desorbing is increased by about 20%, with the majority of this increase coming in the HT peak. As with unreacted CO desorbing during a TPR, the CO TPD exhibits the same inverse behavior between the size of the HT and LT peaks, with the larger clusters having the largest HT peaks, and the small clusters having the largest LT peaks.

Changes in CO desorption during a sequence of CO TPD runs (without O_2 exposure) gives insight into how the Pt_n/alumina surface (and the HT CO desorption peak) is changing under different conditions. The first CO TPD on the pristine Pt_n/alumina surface gives a measure of the density of CO binding sites as a function of cluster size. As shown in Figure 4.5, the trend is similar to that seen when the samples

are preoxidized, including the increasing relative intensity of the HT desorption feature with increasing cluster size. One major difference is the relative amount of CO desorption occurring *between* the LT and HT CO peak (~250-300K). For the oxidized surface, this amount was fairly constant for all cluster sizes, but for the unoxidized surface, the larger clusters have much less desorbing in this region than the small clusters. It is important to note that the overall CO desorbing from the unoxidized surface is greater than when the surface is oxidized by about a factor of ~2 (see unreacted CO desorbing during TPR in Figure 4.2 compared to Figure 4.5). This difference between the amount of CO desorbing for an unoxidized and oxidized surface is too large (especially for the small, unreactive clusters) to attribute the difference to CO lost in the reaction to CO_2, suggesting some other effect that will be discussed later. Also, the lack of strong size dependence for total integrated CO desorption during a CO TPD suggests the ability for the clusters to bind CO does not determine CO_2 production, otherwise the size dependence should be similar.

A second CO TPD done immediately after the first shows a drastic difference in the availability of CO binding sites for all clusters studied. The most obvious change is the decrease in intensity of the HT CO peak for all of the clusters, as well as an increase in the CO desorbing *between* the LT and HT CO peaks. In fact, this increase is so great that the small clusters have essentially lost any real peak separation. What does remain is the clear distinction between small and large clusters with Pt 2,4,7 and Pt 10,14,18 having distinctly different shapes. Overall, the distribution of binding sites has gotten much broader for all of the clusters as it appears the two distinct peaks are merging together, and possibly a third growing in between. A third CO TPD did not deviate from the 2nd

CO TPD spectra shown, so the change occurs after just one CO TPD and is stable thereafter. This same "deactivation" behavior seen for sequential TPRs suggests a similar mechanism of change is occurring for both a CO TPD and a TPR. For small clusters such as those studied here, sintering can be a concern and could explain the behavior seen for the small clusters since they increase in activity for the second TPR. The large clusters, however, either remain unchanged or decrease in activity. It is possible the clusters all sinter to a much larger aggregate that exhibits very similar activity, explaining why the size dependence is largely lost between the first and second TPRs; however, there does appear to be some memory of the initial cluster size, as the overall trend in activity reminiscent of the initial size dependence. Also, if a large cluster was being formed, one might expect the HT CO peak to increase in size since this is usually assigned to CO binding to three-fold hollow sites (see discussion below). In order to fully observe what change is occurring at the surface, imaging technology would be very beneficial, and the best we can do is speculate.

4.3.3 Valence Band Measurement with UPS

In order to investigate the electronic structure of the catalytic surface, X-Ray and Ultraviolet Photoelectron Spectroscopy (XPS/UPS) were employed. Since the main XPS peak for Pt (Pt 4f) overlaps with a significant shake-up feature from the Re 4f peak, we were unable to obtain any core level spectroscopy information about the Pt clusters. Therefore, the only pertinent XPS data collected were of the Al 2s and O 1s peaks from the alumina film. A full discussion about the electronic structure of the film, and how it changes under various reaction conditions, is beyond the scope of this paper and will be

discussed in a separate publication. Here, the focus will be on the as-deposited electronic structure of the Pt_n clusters as in the past this has been shown to correlate closely with catalyst activity.[6, 62] Figure 4.6 shows UP spectra near the Fermi level for a clean alumina support, and the same support with Pt_7 deposited. The clean alumina shows a band gap in the majority of this near Fermi level region until 4 eV where there is sharp rise in the spectra due to the O 2p band. Upon Pt_7 deposition, there are clearly new states that appear in the band gap region of the alumina support, and the spectra shown in Figure 4.6 is representative of all the cluster sizes, save for different shifts in the band below the Fermi level. The shapes of the bands are also slightly different and can be split into two groups. Pt_2 and Pt_4 both show a very slow rise in the density of states (DOS) from the Fermi level and the DOS do not level off before being lost in the O 2p band, while Pt 10, 14, and 18 all rise more quickly and flatten out significantly before meeting the O 2p band. Pt_7 has a shape that is somewhere in between the two extremes for the smaller and larger clusters. The details of the valence band shapes will be discussed in a later chapter.

The inset in Figure 4.6 shows the subtracted Pt_7 spectrum along with the fit to determine how far the valence band is shifted below the Fermi level with the onset being determined at the point where a line tangent to the fit inflection point intersects the baseline intensity. When the shift below the Fermi level is plotted as a function of cluster size (see Figure 4.7), it becomes clear that each cluster has a significantly different electronic structure. The shift below the Fermi level is the largest for Pt_2 and decreases significantly as the cluster gets larger (note inverted scale) until Pt_{10} where the shift becomes quite constant through Pt_{18}. Pt atoms again exhibit behavior that looks like a

larger cluster, such as Pt_7, as its valence shift below the Fermi level is small compared to the trend seen for Pt_2 and Pt_4. When the valence band shifts are plotted against the CO_2 production as a function of cluster size, it becomes apparent that there is in fact a strong correlation between the amount the valence band shifts and the catalyst activity (see Figure 4.7), the details of which can be found in the discussion section.

4.4 Discussion

4.4.1 Correlating HT CO Desorption to CO_2 Production

Past model catalyst and single crystal studies in our lab[59] and others[82-88] have shown the limiting step in the CO oxidation reaction to be the activation of oxygen. While it is not clear what the "active" form of oxygen is under these conditions, in the past, it has been shown that temperature and O_2 dose amount can greatly affect catalyst activity.[59] The results reported here for CO oxidation under 300 K and 180 K oxidation suggest that there is no significant dependence on oxidation temperature for the amount of CO_2 produced. Typically, oxidizing at this low temperature results in a drastic decrease in catalyst activity, and this is taken to mean there is a lack of activated oxygen present on the surface to initiate the reaction -- presumably because the catalyst is inefficient at dissociating molecular oxygen at these lower temperatures. For Pt_n/alumina however, since the CO_2 production is very similar at both temperatures, either oxygen dissociation is equally efficient or inefficient at both temperatures (thus not an "activated" process) and still limiting the catalyst activity, or there is a different factor controlling activity.

Following oxygen activation, the next step in the reaction cycle is CO adsorption. As shown earlier, reactivity does not seem to depend simply on the total amount of available CO binding sites (see lack of size dependence in integrated CO, Figure 4.3), but instead how much CO can adsorb to the HT binding site without prior oxidation (see Figure 4.7). From the CO desorption channels, it is clear the two main CO binding sites differ fairly significantly in binding energy based on their different desorption temperatures. Work in the literature showing CO desorbing from Pt single crystals (111,112) suggest the HT peak is CO bound in three-fold hollow sites of the Pt.[38, 89-91] Other work has shown that as Pt nanoparticles are decreased in size another lower temperature peak forms, presumably due to the lack of available three-fold hollow sites with CO now binding atop or at metal-support periphery sites.[90, 92] These atop and periphery sites are therefore thought to makeup the LT CO binding site measured in this study. To better understand the role of the two CO binding sites, their behavior should be investigated under different conditions.

Desorption of residual CO is slightly different for $T_{oxidation}$ = 180 K and 300 K oxidation. There is a similar variation with cluster size in the relatively intensities of the LT and HT peaks; however, the total integrated residual CO desorption is ~10 % lower when the samples are oxidized at the higher temperature. Furthermore, this decrease in the residual CO desorption is due to a reduction in the HT peak, with essentially no effect of $T_{oxidation}$ on the LT peak. The cluster size dependence of the integrated intensities for the LT and HT CO desorption peaks are compared in Figure 4.8 for $T_{oxidation}$ = 180K and 300 K. CO desorption intensity reflects two factors: the number of available binding sites, and the loss of CO to reaction with adsorbed O. Since the amount of CO_2 produced

is similar for 300 K and 180 K oxidation, the higher CO desorption at 180 K suggests that there are more available HT binding sites for CO when $T_{oxidation}$ is reduced. The binding site concentration is presumably affected by the cluster structure; however, another factor is that oxygen adsorbing during the initial $^{18}O_2$ exposure will tend to block binding sites that might otherwise be occupied by CO. This result is tentatively attributed to variation in the different levels of oxygen competition with this HT CO binding site for the different oxidation temperatures, or perhaps the different oxidation environments restructure the clusters in such a way that more CO can stick when oxidized at 180K. When comparing the intensity of CO desorbing from an unoxidized surface with residual CO desorbing during the first 300K TPR cycle, there is about 50% more HT CO desorbing from the sample that was unoxidized. Again, the largest contributor to the reduction in the amount of CO binding between an oxidized and unoxidized sample is a drastic reduction in the HT CO peak (see Figure 4.4). This again points to oxidation preferentially affecting this HT CO binding site, either blocking it or restructuring it to prevent CO adsorption. With the HT CO desorption temperatures (and therefore binding energies) being virtually identical, oxidation (and temperature) seems to affect the overall number of available HT binding sites during TPR studies. The fact that the CO_2 production does not change drastically between oxidation temperatures even though the amount of HT CO desorbing is different suggests the amount of CO_2 produced does not directly depend on how much CO can bind at the HT binding site during a reaction.

As mentioned earlier, when comparing the HT CO desorption peak from a CO TPD on a pristine surface and one performed after a series of three TPRs with the CO_2 production, there is a strong correlation present (see Figure 4.7). This would suggest that

the amount of CO adsorption to this binding site could be the controlling step in the reaction. From the amount of CO_2 produced for different oxidation temperatures (no significant change), and the differing amounts of CO that desorbs during the respective TPRs as described above, we know reactivity does not depend on how much CO is binding to the HT binding site during a reaction alone. What we can conclude instead is that the number density of those binding sites available prior to (and immediately following) oxidation and a reaction can determine the reactivity. It is possible that this binding site not only binds CO, but it also is the site that binds and activates oxygen. If this is true, then the reaction is still limited by how much active oxygen is present, with oxygen dissociation not being an "activated" process.

This idea is illustrated very clearly with the unexpected behavior exhibited by Pt atoms. Specifically, for either oxidation temperature, Pt atoms produce a significant amount of CO_2, suggesting it behaves like a larger cluster. However, when looking at the residual CO desorbing during the first TPR, it has the smallest HT CO peak and looks very much like the smallest cluster. Even though the amount of residual CO desorbing during a reaction does not directly correlate to CO_2 production, we would still expect the amount of residual CO desorbing from Pt_1 to be more similar to a cluster like Pt_7 due to their similar CO_2 production. This CO desorption trend changes very differently when looking at the final CO TPD after the three sequential TPRs. Here, the HT CO desorption peak for Pt atoms is larger than both Pt_2 and Pt_4, correlating very nicely with the amount of CO_2 produced, suggesting that pre-oxidation of the surface significantly changes the availability of this HT CO binding site. And since there is an excess of CO

desorbing during a reaction cycle, catalyst activity does still seem to be dependent on oxygen activation at this HT CO binding site.

4.4.2 Correlating Electronic Structure with CO_2 Production

Since oxygen activation appears to once again control the CO oxidation reaction for Pt_n/alumina model catalysts, and knowing that oxygen activation also might occur at the HT CO binding site, we can now attempt to determine what controls the number of these binding sites between clusters. Our attention now turns to what effect the position of the top of the valence band has on reactivity. As seen in Figure 4.7, the valence band shift below the Fermi level correlates very strongly with the first round of CO_2 production as a function of cluster size. It has been shown by our group and others that changes in electronic structure as measured with PES can indeed reflect the reactivity of catalytic clusters.[6, 42, 63] For the Pt_n/alumina system studied here, a combination of surface dipoles between the alumina/rhenium interface and the Pt/alumina interface as well as initial/final state effects are all convoluted together to determine the measured electronic structure of the clusters. This "structure" is measured with UPS as a shift in the valence band below the Fermi level (0 BE), essentially measuring the deviation from bulk Pt that the small metal clusters are behaving.

For the trend seen here, the clusters that have a very large shift from the Fermi level (a larger pseudo-band gap) are very unreactive (Pt 2,4,7), while a smaller shift has a much greater reactivity (Pt 10,14,18). What we are interested in from a chemical point of view are the changes of the *initial* (chemical) state of the clusters, as it is this electronic structure that is involved in the catalytic reaction. Unfortunately, photoelectron

spectroscopy measures both the initial and final state of the system (the final state being the electronic energies after the orbitals relax as a result of removing an electron and a lack of hole screening), and separating these two contributions to the spectrum is not trivial. Recent work has shown that Auger spectroscopy can be used to do this; however, the system studied here does not allow for this method to be applied. Other work has shown that qualitative interpretation of the PES shifts can give some insight into more than just the electronic structure of the clusters, but also the physical structure. For example Watanabe and coworkers, looking at Pt_n (n= 4,7-10,15) supported on TiO_2(110), observed that shifts in the XPS reach a stable, nearly unchanging state at the same size where the clusters were seen to change from single layer to multilayer with STM.[39, 42] They also found this transition point to multilayer to correspond to the CO oxidation catalyst activity peaking and leveling off. For the results reported here, the shifts from the Fermi level reach a similar, steady state starting at Pt_{10}, and this also happens to be where the cluster activity levels off (especially for 300K oxidation). ISS results (not shown here, but discussed in detail in a later chapter) appear to show a transition from single layer to multilayer that takes place between Pt_7 and Pt_8 which falls in line with the results from Watanabe, and effectively explains the electronic structure and reactivity trends shown here. Since what seems to control cluster reactivity is oxygen activation, it is reasonable to conclude that the initial electronic structure (and concomitant physical structure) is what determines how efficiently the clusters activate oxygen. Also, since the HT CO binding site as measured with a CO TPD trends with CO_2 production, it is this binding site that is important in the reaction, and the availability of this binding site could depend on the initial electronic structure as well.

4.5 Conclusion

We have shown that for the Pt_n/alumina model catalyst system, there is a very strong Pt_n cluster size dependence (n=1,2,4,7,10,14,18) for efficient CO oxidation where the amount of CO_2 produced varies with cluster size by nearly an order of magnitude. Following the first reaction cycle, much of this size dependence is washed out resulting in a final state reactivity that is high, stable, and no longer very size-dependent. Probing the CO binding sites shows a correlation between CO oxidation activity and the ability to bind CO in the HT binding site on the unoxidized surface. This binding site seems to be important in not only binding the largest amount of CO, but also very well could be the same site where oxygen binds and is "activated." Oxidation temperature can slightly control how much these HT CO binding sites are blocked for CO adsorption, but this does not play a very important role in the CO_2 production as there is always an excess of CO present and the system is still limited by oxygen activation. The oxidation temperatures studied here suggest the Pt_n/alumina system is extremely efficient at activating oxygen as compared to other model systems studied under similar conditions. While it is oxygen activation that controls reactivity between the cluster sizes, it appears that initial cluster electronic structure is controlling how efficiently oxygen is activated by each cluster size. This is seen with the shifting Pt_n valence band correlating strongly with CO_2 production (during the first TPR) as measured with UPS, which relates to the physical nature of the clusters. The drastic differences in reactivity and electronic structure for the different cluster sizes in this size range give some insight into how clusters of the same metal, but of a slightly different size can behave so differently under the same reaction conditions.

4.6 References

1. U. Heiz, A. Sanchez, S. Abbet and W.-D. Schneider, J. Am. Chem. Soc. **121** (13), 3214-3217 (1999).

2. M. Mathes, M. Grass, Y. D. Kim and G. Gantefor, Surf. Sci. **552** (1-3), L58-L62 (2004).

3. S. Vajda, M. J. Pellin, J. P. Greeley, C. L. Marshall, L. A. Curtiss, G. A. Ballentine, J. W. Elam, S. Catillon-Mucherie, P. C. Redfern, F. Mehmood and P. Zapol, Nat. Mater. **8** (3), 213-216 (2009).

4. M. Arenz, S. Gilb and U. Heiz, Chemical Physics of Solid Surfaces **12** (Atomic Clusters), 1-47 (2007).

5. S. Lee, C. Fan, T. Wu and S. L. Anderson, J. Am. Chem. Soc. **126** (18), 5682-5683 (2004).

6. W. E. Kaden, T. Wu, W. A. Kunkel and S. L. Anderson, Science **326**, 826-829 (2009).

7. U. Heiz, A. Sanchez, S. Abbet and W. D. Schneider, Journal of the American Chemical Society **121** (13), 3214-3217 (1999).

8. S. Abbet, U. Heiz, H. Häkkinen and U. Landman, Phys. Rev. Lett. **86** (26), 5950-5953 (2001).

9. L. D. Socaciu, J. Hagen, T. M. Bernhardt, L. Woeste, U. Heiz, H. Haekkinen and U. Landman, Journal of the American Chemical Society **125** (34), 10437-10445 (2003).

10. B. Yoon, H. Haekkinen, U. Landman, A. S. Woerz, J.-M. Antonietti, S. Abbet, K. Judai and U. Heiz, Science (Washington, DC, United States) **307** (5708), 403-407 (2005).

11. C. J. Harding, S. Kunz, V. Habibpour and U. Heiz, Phys. Chem. Chem. Phys. **10** (38), 5875-5881 (2008).

12. C. J. Harding, S. Kunz, V. Habibpour and U. Heiz, Chem. Phys. Lett. **461** (4-6), 235-237 (2008).

13. C. J. Harding, S. Kunz, V. Habibpour, V. Teslenko, M. Arenz and U. Heiz, Journal of Catalysis **255** (2), 234-240 (2008).

14. S. Kunz, F. F. Schweinberger, V. Habibpour, M. Rottgen, C. Harding, M. Arenz and U. Heiz, Journal of Physical Chemistry C **114** (3), 1651-1654 (2010).

15. D. R. Rainer, M. Koranne, S. M. Vesecky and D. W. Goodman, Journal of Physical Chemistry B **101** (50), 10769-10774 (1997).

16. M. Valden, X. Lai and D. W. Goodman, Science **281** (5383), 1647-1650 (1998).

17. A. Kolmakov and D. W. Goodman, Surf. Sci. **490** (1-2), L597-L601 (2000).

18. A. K. Santra and D. W. Goodman, Electrochimica Acta **47** (22-23), 3595-3609 (2002).

19. F. Gao, Y. Wang, Y. Cai and D. W. Goodman, Surface Science **603** (8), 9 (2009).

20. S. M. McClure, M. Lundwall, Z. Zhou, F. Yang and D. W. Goodman, Catalysis Letters **133** (3-4), 298-306 (2009).

21. M. S. Chen, Y. Cai, Z. Yan, K. K. Gath, S. Axnanda and D. W. Goodman, Surface Science **601** (23), 5326-5331 (2007).

22. S. M. McClure and D. W. Goodman, Chem. Phys. Lett. **469**, 1-13 (2009).

23. I. Z. Jones, R. A. Bennett and M. Bowker, Surf. Sci. **439** (1-3), 235-248 (1999).

24. J.-H. Fischer-Wolfarth, J. A. Farmer, J. M. Flores-Camacho, A. Genest, I. V. Yudanov, N. Rösch, C. T. Campbell, S. Schauermann and H.-J. Freund, Phys. Rev. B **81**, 241416 (241414 pages) (2010).

25. G. Rupprechter, Unterhalt, H., Morkel, M., Galletto, P., Hu, L., Freund, H.-J. , Surf. Sci **502-503**, 109-122 (2002).

26. H. Conrad, G. Ertl and J. Kueppers, Surface Science **76** (2), 323-342 (1978).

27. T. Engel and G. Ertl, Chemical Physics Letters **54** (1), 95-98 (1978).

28. T. Engel and G. Ertl, Journal of Chemical Physics **69** (3), 1267-1281 (1978).

29. I. Stara and V. Matolin, Surface Science **313** (1-2), 99-106 (1994).

30. I. Jungwirthovk, I. Star and V. Matolin, Surface Science **377-379** 644-649 (1997).

31. V. Matolin, V. Johánek, I. Stará, N. Tsud and K. Veltruská, Surface Science **507–510** (0), 803-807 (2002).

32. A. Boubnov, A. Gaenzler, S. Conrad, M. Casapu and J.-D. Grunwaldt, Topics in Catalysis **56** (Copyright (C) 2013 American Chemical Society (ACS). All Rights Reserved.), 333-338 (2013).

33. A. Tomita, K.-i. Shimizu, K. Kato, T. Akita and Y. Tai, J. Phys. Chem. C **117** (Copyright (C) 2013 American Chemical Society (ACS). All Rights Reserved.), 1268-1277 (2013).

34. D. N. McCarthy, C. E. Strebel, T. P. Johansson, A. den Dunnen, A. Nierhoff, J. H. Nielsen and I. Chorkendorff, J. Phys. Chem. C **116** (29), 15353-15360 (2012).

35. X. Chen, J. Chen, Y. Zhao, M. Chen and H. Wan, Cuihua Xuebao **33** (Copyright (C) 2013 American Chemical Society (ACS). All Rights Reserved.), 1901-1905 (2012).

36. G. Busca, E. Finocchio and V. S. Escribano, Applied Catalysis, B: Environmental **113-114** (Copyright (C) 2013 American Chemical Society (ACS). All Rights Reserved.), 172-179 (2012).

37. E.-Y. Ko, E. D. Park, K. W. Seo, H. C. Lee, D. Lee and S. Kim, J. Nanosci. Nanotechnol. **6** (Copyright (C) 2013 American Chemical Society (ACS). All Rights Reserved.), 3567-3571 (2006).

38. K. R. McCrea, J. S. Parker and G. A. Somorjai, Journal of Physical Chemistry B **106** (Copyright (C) 2013 American Chemical Society (ACS). All Rights Reserved.), 10854-10863 (2002).

39. N. Isomura, X. Wu, H. Hirata and Y. Watanabe, J. Vac. Sci. Technol., A **28** (5), 1141-1144 (2010).

40. L. Liu, F. Zhou, L. Wang, X. Qi, F. Shi and Y. Deng, Journal of Catalysis **274** (Copyright (C) 2013 American Chemical Society (ACS). All Rights Reserved.), 1-10 (2010).

41. S. Bonanni, K. Ait-Mansour, H. Brune and W. Harbich, ACS Catalysis **1** (4), 385-389 (2011).

42. Y. Watanabe, X. Wu, H. Hirata and N. Isomura, Catalysis Science & Technology **1** (8), 1490-1495 (2011).

43. M. J. Berr, F. F. Schweinberger, M. Doeblinger, K. E. Sanwald, C. Wolff, J. Breimeier, A. S. Crampton, C. J. Ridge, M. Tschurl, U. Heiz, F. Jaeckel and J. Feldmann, Nano Letters **12** (11), 5903-5906 (2012).

44. S. Bonanni, K. Ait-Mansour, W. Harbich and H. Brune, J. Am. Chem. Soc. **134** (7), 3445-3450 (2012).

45. M. Moses-DeBusk, M. Yoon, L. F. Allard, D. R. Mullins, Z. Wu, X. Yang, G. Veith, G. M. Stocks and C. K. Narula, J. Am. Chem. Soc. **135** (Copyright (C)

2013 American Chemical Society (ACS). All Rights Reserved.), 12634-12645 (2013).

46. K.-i. Shimizu, K. Ohshima, Y. Tai, M. Tamura and A. Satsuma, Catalysis Science & Technology **2** (4), 730-738 (2012).

47. F. J. Perez-Alonso, D. N. McCarthy, A. Nierhoff, P. Hernandez-Fernandez, C. Strebel, I. E. L. Stephens, J. H. Nielsen and I. Chorkendorff, Angewandte Chemie, International Edition **51** (19), 4641-4643, S4641/4641-S4641/4649 (2012).

48. D.-e. Jiang, S. H. Overbury and S. Dai, J. Phys. Chem. C **116** (41), 21880-21885 (2012).

49. N. Isomura, X. Wu and Y. Watanabe, J. Chem. Phys. **131** (16), 164707/164701-164707/164704 (2009).

50. H. Yasumatsu, T. Hayakawa and T. Kondow, J. Chem. Phys. **124** (1), 014701/014701-014701/014707 (2006).

51. R. E. Winans, S. Vajda, G. E. Ballentine, J. W. Elam, B. Lee, M. J. Pellin, S. Seifert, G. Y. Tikhonov and N. A. Tomczyk, Topics in Catalysis **39** (3-4), 145-149 (2006).

52. H. Yasumatsu, T. Hayakawa, S. i. Koizumi and T. Kondow, J. Chem. Phys. **123** (12), 124709/124701-124709/124709 (2005).

53. d. M. F. Buatier, M. Scherer, B. Gleich, E. Kopatzki and R. J. Behm, Surf. Sci. **411** (Copyright (C) 2013 American Chemical Society (ACS). All Rights Reserved.), 249-262 (1998).

54. K. D. Schierbaum, S. Fischer, M. C. Torquemada, J. L. de Segovia, E. Roman and J. A. Martin-Gago, Surf. Sci. **345** (3), 261-273 (1996).

55. S. Lee, C. Fan, T. Wu and S. L. Anderson, J. Chem. Phys. **123**, 124710 124713 pages. (2005).

56. W. E. Kaden, W. A. Kunkel and S. L. Anderson, J. Chem. Phys. **131**, 114701, 114701-114715 (2009).

57. T. Wu, W. E. Kaden, W. A. Kunkel and S. L. Anderson, Surface Science **603** (17), 2764-2770 (2009).

58. S. Vajda, S. Lee, K. Sell, I. Barke, A. Kleibert, V. von Oeynhausen, K.-H. Meiwes-Broer, A. F. Rodriguez, J. W. Elam, M. M. Pellin, B. Lee, S. Seifert and R. E. Winans, J. Chem. Phys. **131** (12), 121104/121101-121104/121104 (2009).

59. W. E. Kaden, W. A. Kunkel, M. D. Kane, F. S. Roberts and S. L. Anderson, J. Am. Chem. Soc. **132**, 13097–13099 (2010).

60. S. Lee, B. Lee, F. Mehmood, S. Seifert, J. A. Libera, J. W. Elam, J. Greeley, P. Zapol, L. A. Curtiss, M. J. Pellin, P. C. Stair, R. E. Winans and S. Vajda, J. Phys. Chem. C **114** (23), 10342-10348 (2010).

61. W. E. Kaden, W. A. Kunkel, F. S. Roberts, M. Kane and S. L. Anderson, J. Chem. Phys. **136**, 204705/204701-204705/204712 (2012).

62. S. Proch, M. Wirth, H. S. White and S. L. Anderson, J. Am. Chem. Soc. **135**, 3073−3086 (2013).

63. M. D. Kane, F. S. Roberts and S. L. Anderson, Faraday Disc. **162**, 323 - 340 (2013).

64. G. Kwon, G. A. Ferguson, C. J. Heard, E. C. Tyo, C. Yin, J. DeBartolo, S. Seifert, R. E. Winans, A. J. Kropf, J. Greeley, R. L. Johnston, L. A. Curtiss, M. J. Pellin and S. Vajda, ACS Nano **Just Accepted (on line)** (2013).

65. B.-H. Mao, R. Chang, S. Lee, S. Axnanda, E. Crumlin, M. E. Grass, S.-D. Wang, S. Vajda and Z. Liu, J. Chem. Phys. **138**, 214304-214311 (2013).

66. S. Abbet, A. Sanchez, U. Heiz and W.-D. Schneider, Journal of Catalysis **198** (1), 122-127 (2001).

67. K. J. Boyd, A. Lapicki, M. Aizawa and S. L. Anderson, Review of Scientific Instruments **69**, 4106-4115 (1998).

68. P. J. Chen and D. W. Goodman, Surf. Sci. **312**, L767-L773 (1994).

69. S. C. Street and D. W. Goodman, Chem. Phys. Solid Surf. **8** (Copyright (C) 2013 American Chemical Society (ACS). All Rights Reserved.), 375-406 (1997).

70. X. Lai, C. C. Chusuei, K. Luo, Q. Guo and D. W. Goodman, Chem. Phys. Lett. **330** (3,4), 226-230 (2000).

71. Y. Wu, E. Garfunkel and T. E. Madey, Surf. Sci. **365** (Copyright (C) 2012 American Chemical Society (ACS). All Rights Reserved.), 337-352 (1996).

72. Y. Wu, E. Garfunkel and T. E. Madey, J. Vac. Sci. Technol., A **14** (Copyright (C) 2012 American Chemical Society (ACS). All Rights Reserved.), 2554-2563 (1996).

73. F. Sloan Roberts and S. L. Anderson, Review of Scientific Instruments **84** (12), - (2013).

74. R. Schlaf, P. G. Schroeder, M. W. Nelson, B. A. Parkinson, C. D. Merritt, L. A. Crisafulli, H. Murata and Z. H. Kafafi, Surf. Sci. **450**, 142-152 (2000).

75. K. Manandhar and B. A. Parkinson, The Journal of Physical Chemistry C **116** (36), 19379-19384 (2012).

76. F. S. Roberts, M. D. Kane and S. L. Anderson, Unpublished results (2014).

77. S. Lee, C. Fan, T. Wu and S. L. Anderson, Surface Science **578**, 5-19 (2005).

78. M. Aizawa, S. Lee and S. L. Anderson, Surf. Sci. **542** (3), 253-275 (2003).

79. S. Lee, C. Fan, T. Wu and S. L. Anderson, Journal of Physical Chemistry B **109**, 11340-11347 (2005).

80. C. Fan, T. Wu, W. E. Kaden and S. L. Anderson, Surf. Sci. **600**, 461-467 (2006).

81. S. Lee, C. Fan, T. Wu and S. L. Anderson, J. Phys. Chem. **109**, 381-388 (2005).

82. R. Pal, L.-M. Wang, Y. Pei, L.-S. Wang and X. C. Zeng, J. Am. Chem. Soc. **134** (22), 9438-9445 (2012).

83. X. Wu, A. Selloni and S. K. Nayak, J. Chem. Phys. **120** (9), 4512-4516 (2004).

84. J. D. Stiehl, T. S. Kim, S. M. McClure and C. B. Mullins, J. Am. Chem. Soc. **126** (6), 1606-1607 (2004).

85. B. Yoon, H. Haekkinen and U. Landman, Journal of Physical Chemistry A **107** (20), 4066-4071 (2003).

86. V. A. Bondzie, S. C. Parker and C. T. Campbell, Catalysis Letters **63** (3-4), 143-151 (1999).

87. D. H. Parker and B. E. Koel, J. Vac. Sci. Technol. A **8** (3), 2585-2590 (1990).

88. M. A. Chesters and G. A. Somorjai, Surf. Sci. **52**, 21-28 (1975).

89. M. T. Paffett, S. C. Gebhard, R. G. Windham and B. E. Koel, J. Phys. Chem. **94** (17), 6831-6839 (1990).

90. U. Heiz, R. Sherwood, D. M. Cox, A. Kaldor and J. T. Yates, Jr., J. Phys. Chem. **99** (21), 8730-8735 (1995).

91. R. D. Ramsier, K. W. Lee and J. T. Yates, Jr., Surf. Sci. **322** (1-3), 243-255 (1995).

92. U. Heiz, R. Sherwood, D. M. Cox, A. Kaldor and J. T. Yates, Jr., NATO ASI Ser., Ser. C **465** (Synergy between Dynamics and Reactivity at Clusters and Surfaces), 37-47 (1995).

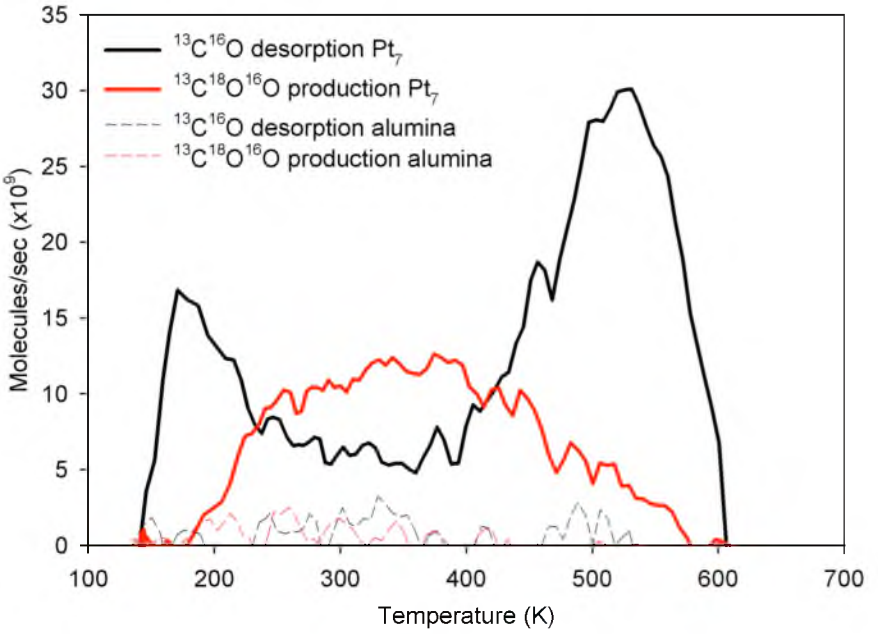

Figure 4.1 Residual ^{13}CO (black) desorption and $^{13}C^{18}O^{16}O$ production (red) for the first 300K oxidation TPR over Pt_7/alumina. There are two distinct CO desorption peaks at 175K and 525K, while the CO2 production is broad and peaks around 350K between the CO desorption.

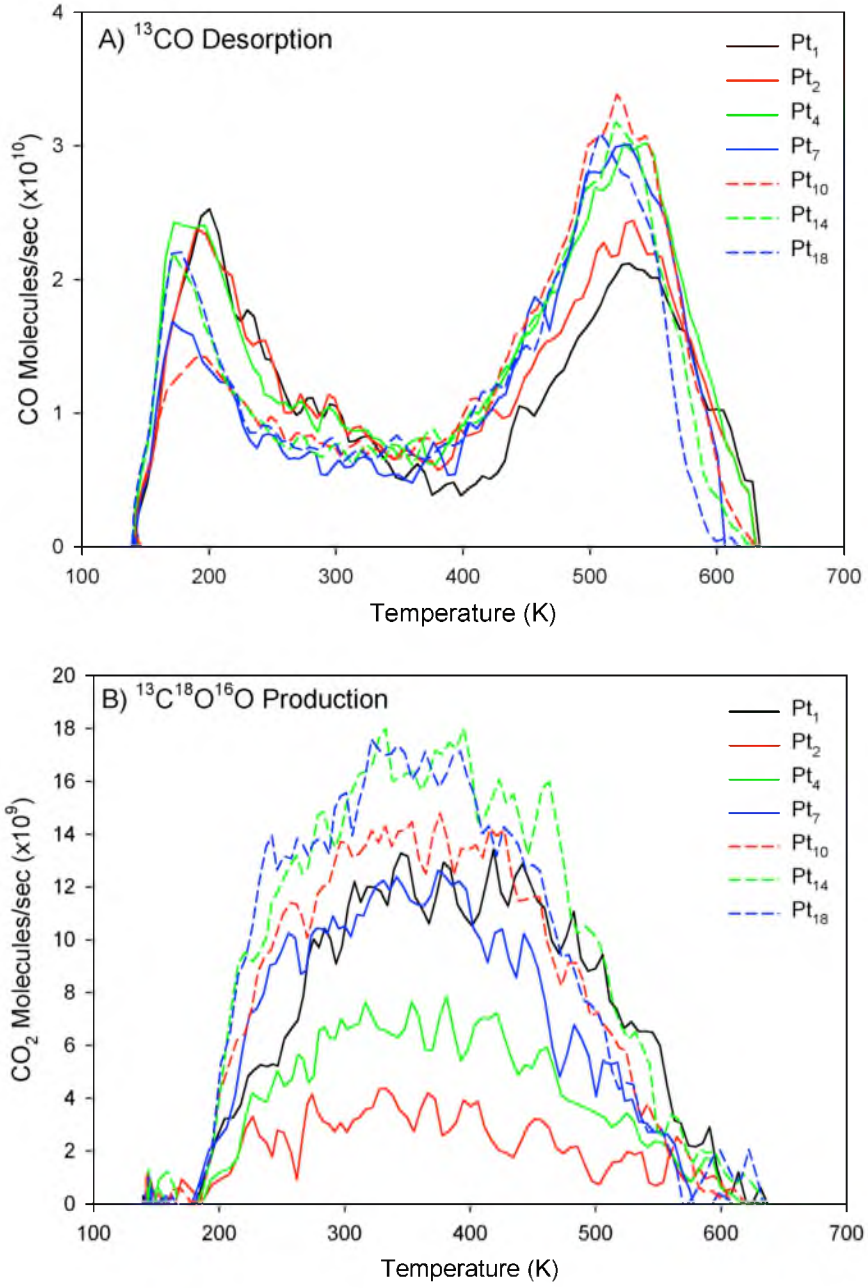

Figure 4.2 Residual ^{13}CO (mass 29) desorption from the first 300K oxidation TPR for all cluster sizes studied (a) and corresponding $^{13}C^{18}O^{16}O$ production (mass 47) (b).

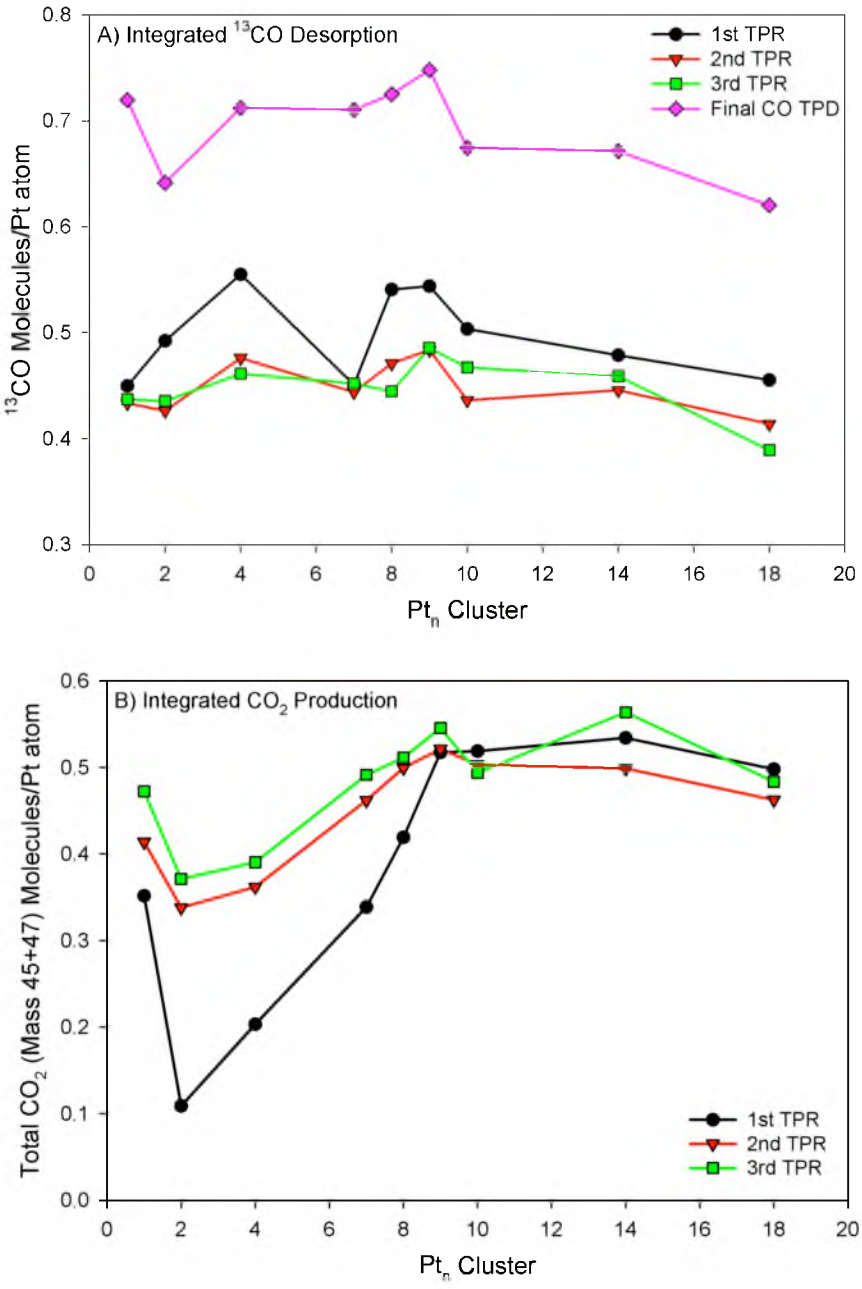

Figure 4.3 Integrated # of CO molecules desorbed (a) and CO_2 molecules produced (b) during three subsequent TPR with a T_{ox} = 300 K and a final CO TPD. Notice the lack of CO desorption variation with cluster size, where the CO_2 increases by an order of magnitude between Pt_2 and Pt_{10}. For the final CO TPD, there was no measureable CO_2 production. Note the different y-axis scales.

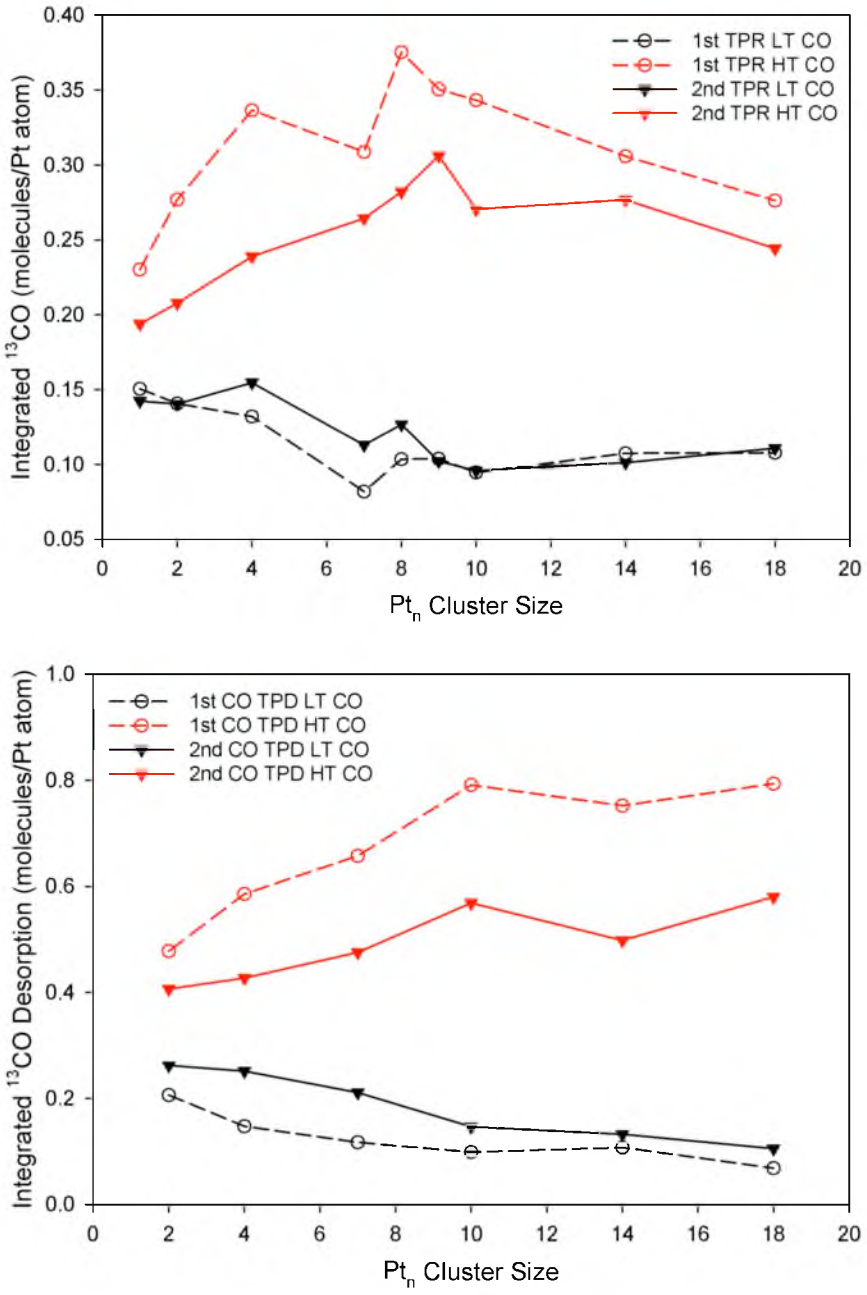

Figure 4.4 Intensities for LT (black) and HT (red) residual CO desorbing during the first (dashed) and second (solid) 300 K oxidation reactions (a). Notice the significant decrease in the HT CO desorbing during the second run, as compared to very little change for the LT CO peak. The same HT and LT desorbing CO is shown in (b) for two consecutive CO TPDs. Note: there is little to no change in the mid-temperature peak for both the 300 K oxidation TPR and the CO TPD.

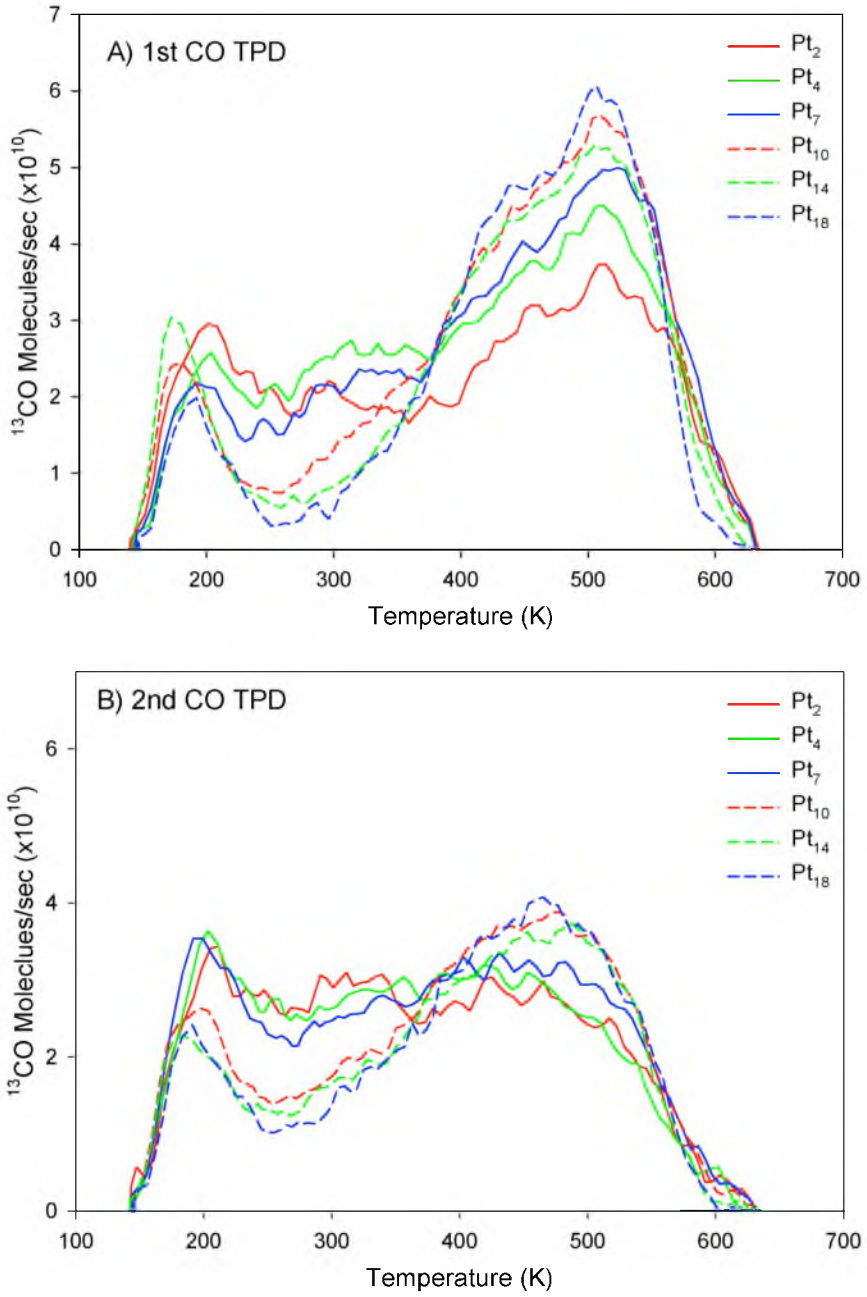

Figure 4.5 Integrated ^{13}CO (mass 29) desorbing from the unoxidized surface after 10 L ^{13}CO exposure at 180K as a function of cluster size for the first CO TPD (a) and second CO TPD on the same surface (b). Notice the distinct drop in the size of the HT CO peak between the first and second CO TPD.

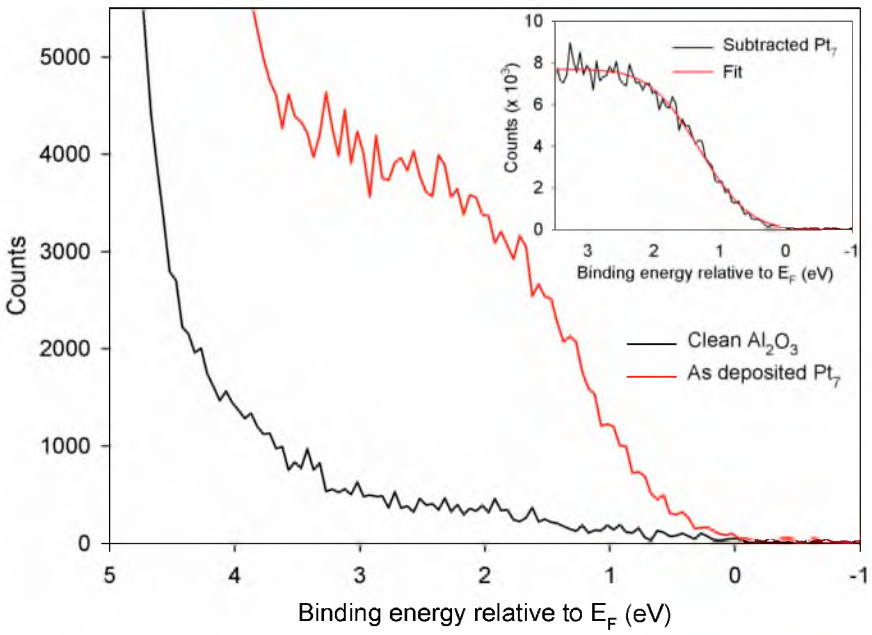

Figure 4.6 Raw UP spectra near the Fermi level for a 4.2 nm alumina film (black) and the same film with 10% ML of Pt_7 deposited (red). The sharp rise in the spectrum at >4 eV is the onset of the O 2p band. The inset shows the Pt_7 spectrum with the clean alumina spectrum subtracted out (black) along with a fit (red) to determine the onset of the Pt_7 valence band.

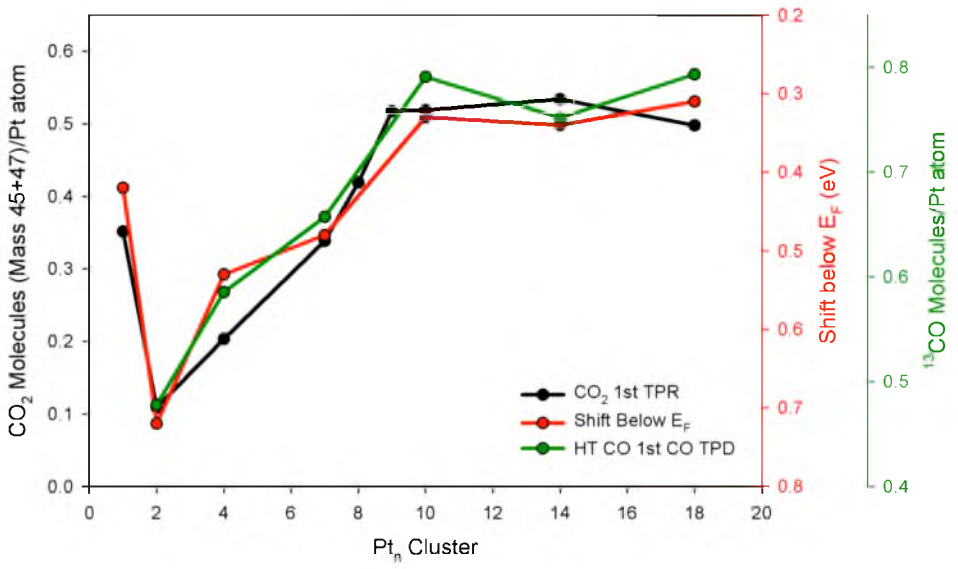

Figure 4.7 There is a strong correlation between CO_2 production (T_{ox} = 300 K, black line), the shift of the valence band below the Fermi Leve (red), and the amount of CO desorbing from the high temperature (HT) binding site during the 1st CO TPD on a fresh sample (green).

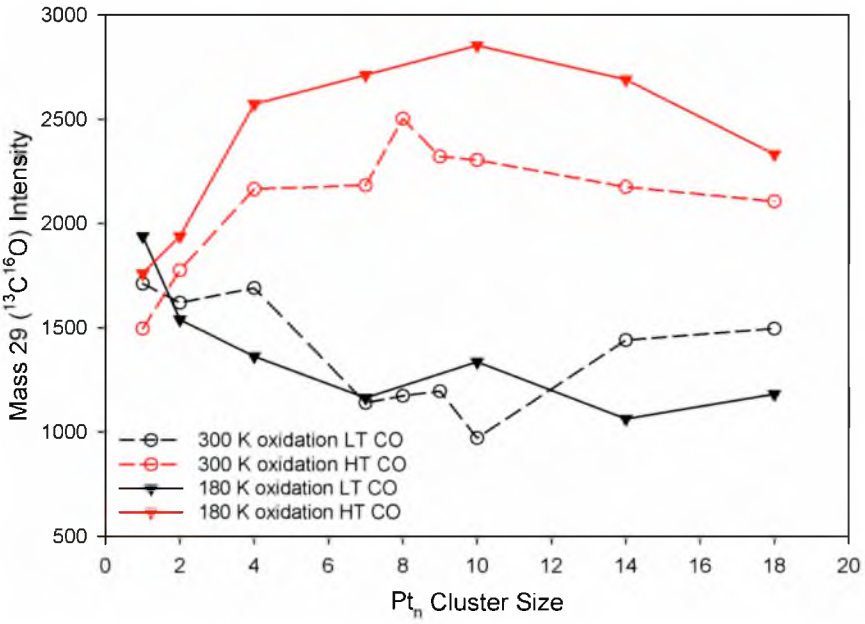

Figure 4.8 Intensities of the LT (black) and HT (red) residual CO peaks during the first TPR for 300 K oxidation (dashed) and 180 K oxidation (solid) are shown for different cluster sizes. Note the increase in the HT peak for 180 K oxidation for all clusters, where the LT peak remains fairly constant between the two temperatures.

CHAPTER 5

THE SIZE-DEPENDENT PHYSICAL AND ELECTRONIC PROPERTIES OF THE $Pt_n/Al_2O_3/Re(0001)$ MODEL CATALYST: AN ISS, PES, AND TPD STUDY

5.1 Introduction

Improving catalyst efficiency and selectivity is of growing importance with the rising cost and limited supply of many of the metals used. Part of achieving this goal is understanding, on a fundamental level, what properties are important in controlling how a catalyst functions. Oftentimes this is done using model catalysts in order to control many of the variables involved in the catalytic reaction conditions.[1-7] Many model catalysts have well-defined surfaces which allow for links to be formed between catalytic reactivity and fundamental properties that define each catalyst. More specifically, understanding the physical and electronic structure of model catalysts gives significant insight into the functionality, and ultimately the mechanism of the catalytic systems. Only after developing this knowledge base from both experimental and theoretical models can new and better catalyst systems be predicted and tested.

For experimental model catalysts, a wide array of surface analysis techniques offers a toolset for investigating not only the catalytic activity and reactant binding sites, but also the physical and electronic properties of the surface. For the work presented here, low energy ion scattering spectroscopy (ISS) can effectively probe how the physical properties of the surface change on a relativistic level. More specifically for the $Pt_n/Al_2O_3/Re(0001)$ system, the amount of Pt in the surface layer for the different cluster sizes can determine whether the clusters are single or multilayer, as well as determining any changes that occur to the Pt surface layer after a reaction. Performing ISS after exposure to adsorbates and simultaneous with heating can give information about where the adsorbates are binding. Coupling this information with that obtained from temperature programmed desorption/reaction (TPD/TPR) which ostensibly determines

adsorbate binding energy, we can then determine where the physical binding sites are for the energetically different bound adsorbates. The relative differences between the distribution of adsorption sites between cluster sizes, and under different reaction conditions, gives useful information about the potential chemical differences of the catalytic surfaces. Finally, photoelectron spectroscopy (PES) measures relative electronic structure differences between the surfaces studied, and how those surfaces change under different reaction conditions, i.e. exposure to adsorbates, the effect of heating, etc. By combining all of these techniques, a fairly complete picture of the physical and electronic properties of the $Pt_n/Al_2O_3/Re(0001)$ catalytic surfaces is constructed. How these properties change as a function of cluster size is a fundamental piece of knowledge crucial to understanding the overall mechanism and functionality of heterogeneous catalysts.

5.2 Experimental Methodology

5.2.1 Model Catalyst Preparation

The cluster beamline and ultrahigh vacuum (UHV) chamber used for the experiments has been described elsewhere[8, 9] and will not be discussed in detail here. The setup has access to several *in situ* surface analysis techniques, including X-ray photoelectron spectroscopy (XPS), low energy ion scattering spectroscopy (ISS), and temperature programmed reaction/desorption (TPR/TPD). Two new additions, which are used for the following experiments, include ultraviolet photoelectron spectroscopy (UPS) and thin film growth, both of which will be briefly introduced here. A hollow cathode VUV lamp, the details of which have been reported elsewhere,[10] was designed and

constructed to attach to our UHV chamber for *in situ* analysis of the valence level structure of the sample. Since our alumina thin film supports have a significant band gap, the position of the Fermi level was determined by referencing the kinetic energy spectra to the 0 binding energy of a silver flag spot-welded a few centimeters above our sample (in electrical contact). During UPS measurements, the sample was floated at -15.0 volts in order to accelerate the photoelectrons and separate the secondary peaks of the sample and spectrometer to allow for surface work function determination. During lamp operation, the pressure was no higher than 2×10^{-7} Torr in the UHV chamber thanks to two stages of differential pumping on the lamp.

Alumina thin film growth was performed in an attached antechamber which seals against the sample holder as the sample is transferred into the antechamber. The doubly differentially pumped seal allows the antechamber to be vented to perform sample maintenance without disturbing UHV, and also provides a convenient location to grow the alumina thin films without exposing the UHV chamber to large amounts of oxygen. The aluminum is evaporated from a homebuilt resistively heated crucible in the style of a Knudsen cell. The temperature and power of the source was monitored to ensure stable aluminum evaporation and cell stability. The procedure for thin film growth was adapted from Goodman[11-13] and Madey[14, 15] and results in a predominately gamma crystalline thin film as determined with LEED and ISS.

The model catalysts were prepared on a rhenium(0001) single crystal (Marketech International) that is spot welded to two resistive heating wires and connected to a liquid nitrogen cooled cryostat that allows temperatures as low as 100 K. The sample can be heated to 1100 K resistively, and up to 2200 K via electron bombardment. Prior to each

experiment, the Re(0001) substrate is heated to 1850 K for 4.5 minutes with a final flash to 1950 K for 30 seconds. This procedure is adapted from other groups using a Re(0001) single crystal, and LEED and XPS has shown this method to effectively decompose and evaporate any alumina film while also restoring order to the surface.[12, 14, 15] For our experiments, XPS was used after annealing to determine surface cleanliness and the heating times were increased to ensure satisfactory surface order.

Once the Re(0001) is adequately cleaned, the sample is then sealed inside the antechamber for alumina thin film growth. With the sample held at 970 K in a background of 5 x 10^{-6} Torr O_2, aluminum was evaporated from the resistively heated ceramic crucible allowing alumina to grow on the Re(0001) surface at a rate between 2-3 Å/min. Film thickness was determined with XPS by using the rhenium to aluminum core level intensity ratios and the mean free path of rhenium photoelectrons through an alumina overlayer to calculate the film thickness. Final film thicknesses were allowed to ranged between 3-6 nm where we have previously shown physical, electronic, and catalytic properties to be independent of film thickness.[16] With the film grown, 10% of a monolayer (ML) of Pt_n was deposited at ~ 1 ev/atom with the number of atoms being held constant between cluster sizes. The experimental protocol then diverges according to what properties are to be measured. Studies to measure the physical structure use low energy ion scattering spectroscopy (ISS), the electronic structure is measured with X-ray/ultraviolet photoelectron spectroscopy (XPS/UPS), and reactivity/binding site measurements are done using temperature programmed reaction/desorption (TPR/TPD). All three types of experiments are kept separate in order to keep the model catalysts as pristine as possible, and prevent any overlapping effects from different surface analyses.

5.2.2 ISS and PES Experiments

For the first set of ISS experiments, a series of spectra were recorded for each cluster size immediately after cluster deposition. The first three were considered "low flux" with a He^+ neutralization current on the sample of about 0.2 μA, followed by ten "high flux" measurements with a He^+ neutralization current of about 2.0 μA. The first few (including "low flux") measurements are meant to gently remove any adsorbates that bound during cluster deposition. The last several spectra determine the Pt removal rate in order to extrapolate back to 0 He^+ exposure, as shown in Figure 5.1 for Pt_2. Since this series of ISS experiments greatly damages our surface, no further experiments were performed on these samples.

The temperature-dependent ISS (TD-ISS) experiments were performed for only Pt_4 and Pt_{14} as representative clusters for the "small" and "large" size regimes. The Pt and CO removal rates were performed on two different samples for each cluster size, and were simply a series of "low flux" spectra to determine the Pt ISS signal as a function of He^+ exposure. For the TD-ISS experiments (both with and without a CO dose), two "low flux" measurements were recorded at each temperature shown in order to determine the Pt intensity with minimal surface damage. For the CO TD-ISS experiments, CO was first dosed at 180 K to mimic the procedure for a CO TPD.

The photoelectron spectroscopy experiments were performed on a completely separate set of samples than those used for the ISS work. Immediately after film growth, XPS and UPS were performed to measure the Al, O, and Re core levels (XPS), as well as valence structure of the film (UPS). The same XPS and UPS set was measured again after each step in the CO oxidation reaction cycle: 1) Pt_n deposition to determine the as-

deposited valence structure. 2) After oxidizing at 180 K with 10 L O_2. 3) Dosing 10 L CO at 180 K. 4) After heating the sample to 650 K at 3 K/sec.

5.3 Results and Discussion

5.3.1 ISS to Determine Physical Structure

When attempting to investigate and describe the physical structure of the $Pt_n/Al_2O_3/Re(0001)$ system, it is best to first explore differences between the pristine size selected catalytic surfaces. Following the catalyst preparation procedures detailed earlier, each different size to be studied was prepared on a new, clean alumina surface with a series of ISS spectra collected immediately following cluster deposition. Due to the possibility of adsorbates being present on the surface prior to performing the ISS spectra, a series of ISS measurements was performed to obtain surface Pt intensity as a function of He^+ exposure. What results is a downward sloping Pt signal with each spectrum acquired, and using the slope of the decline and extrapolating back to 0 He^+ exposure, we then obtain what is called the "as deposited" Pt signal. This method helps to correct the as deposited Pt ISS signal for differing amounts of adventitious adsorbates that may suppress the first few Pt ISS spectra, and also for different He^+ sputter rates from the measurement itself. The as-deposited Pt ISS signal collected separately for each cluster size is shown in Figure 5.2. The Pt intensity is plotted as a ratio to the substrate signal (Al+O) in order to account for any fluctuations in day-to-day He^+ intensity.

When analyzing the as-deposited Pt ISS signal as a function of cluster size, it becomes clear there are two different size regimes. The first, "small" cluster sizes (n= 2,4,7) all have a nominal Pt:(Al+O) ratio ranging from 0.60 to 0.64 with an average of

0.62 and an estimated uncertainty of 0.05 based on based on the standard deviation of several sets of data. There is an abrupt change in the amount of Pt ISS signal when moving from Pt_7 to Pt_8, with the signal dropping by 15% from 0.64 to 0.54. Above Pt_8, in the "large" cluster regime, the Pt ISS signal stays at this lower value ranging between 0.54 and 0.50 with an average of 0.53 up to the maximum cluster size studied of Pt_{18}. Because of the significant difference between Pt_7 and Pt_8, the ISS experiments were repeated 3 times each for these two clusters on freshly prepared samples, and the error bars plotted in Figure 5.2 reflect the standard error of the repeated runs. The obvious outlier to this trend is Pt atoms, where the value measured is 0.56 which is most similar to the value of a "large" cluster. Since Pt atoms are predicted to be the most mobile species on the surface, this low value is thought to be due to the effect of Pt atoms sintering to form larger clusters. Reactivity and UPS studies reported here support this theory as their catalytic CO oxidation and electronic structure also resemble that of a larger cluster.

Interpretation of the two different size regimes for the Pt ISS intensity is based on the fact that there are equal numbers of atoms present on the surface, and therefore, the lower relative Pt ISS signal means there is less Pt in the top most surface layer (the area that ISS probes). Since the Pt population is the same, the lower Pt ISS intensity for the "large" size regime suggests the Pt clusters are now forming 3-D clusters (multilayer) as compared to the single layer clusters in the "small" regime. This new Pt multilayer now shadows a portion of the underlying Pt, thus lowering the measured Pt ISS signal. Similar results for Pd size selected clusters supported on TiO_2(110) have shown the transition to occur between 10 and 16 Pd atoms using a similar ISS method.[2, 17]

The formation of this second layer has been shown to be important in terms of maximizing model catalyst activity as the atoms in this new layer are highly uncoordinated and are thought to play a vital role in the dissociation of oxygen.[18-22] For example, the Watanabe group has shown that with the transition of size-selected Pt clusters to multilayer as measured with STM coincides with maximum CO oxidation activity.[18, 19] The Goodman group saw a similar result studying Au clusters with the transition from single to multilayer occurring at the same size as the peak CO oxidation intensity.[21, 22] In both cases, the formation of this multilayer was accompanied by a change in the electronic structure of the clusters: for the Watanabe group, the Pt 4f XPS shifts became steady and unchanging once the second layer started growing, and the Goodman group saw a significant change in the cluster band gap as measured with STS. When applying this idea to previous work reported in our group, a similar trend is seen. For the $Pd_n/TiO_2(110)$ system, the substantial increase in CO oxidation activity occurred between clusters Pd_{10} and Pd_{16}, with the larger clusters being significantly more active than the smaller clusters. From the ISS results, it is believed that the large clusters were indeed multilayer as compared to the single layer small clusters.

The $Pt_n/Al_2O_3/Re(0001)$ model system also exhibited similar behavior in terms of the catalytic activity and electronic structure, the details of which have been recently published. Applying the fact that the transition to multilayer begins between Pt_7 and Pt_8, it again appears that the growth of this second layer is reflected in the CO oxidation activity and the electronic structure. For the reactivity studies, the maximum is reached at Pt_{10} where the transition to multilayer is complete according to Watanabe,[18, 19, 23] and

this is also where the electronic structure, as measured with UPS, stabilizes with the shifts unchanging for the large cluster sizes.

Beyond determining relative differences in physical structure between cluster sizes, ISS is also useful in measuring how the surface Pt changes under reaction conditions. For CO oxidation over the $Pt_n/Al_2O_3/Re(0001)$ system studied here, the surface Pt intensity drops off significantly after just one CO TPD cycle. In fact, the decrease in Pt ISS intensity is the same whether a single CO TPD was performed or a series of CO oxidation reactions, and the results are shown in Figure 5.2. This behavior is consistent with the TPD/TPR properties of the surface being unchanging after the second desorption/reaction cycle, suggesting some stable, final state is reached that has a decreased amount of surface Pt. The decrease could be due to restructuring or sintering of the clusters to form larger particles, or a persistent adsorbate that is bound on top of the clusters. Since the catalyst activity begins to reach a nominal value for all cluster sizes for the second reaction cycle and beyond, it is more likely that the clusters are restructuring or sintering.

Rather than just probing the physical structure of the surface before and after a reaction cycle, ISS can also be used to investigate the structure after different intermediate stages of the reaction. For example, as shown in Figure 5.3, after exposing Pt_4 and Pt_{14} to 10 L of CO, the Pt ISS signal becomes nearly negligible as the CO is binding on top of the clusters and shadowing them during the ISS measurement. Subsequent ISS spectra were obtained after heating the sample to various temperatures to determine what effect desorbing some of the CO has on the Pt signal. From the CO TPD shown in Figure 5.4, it becomes clear that even after reaching a temperature which

desorbs CO from the low temperature binding site, the Pt ISS signal has not made any recovery beyond simply CO removal from He^+ exposure. This suggests that the CO in this desorption site is not present on top of the clusters, but instead must be bound at the periphery. Once a temperature is reached where the high temperature CO is desorbed, the Pt ISS signal recovers significantly, suggesting this CO species is indeed bound on top of the Pt clusters (and is bound more strongly than the periphery CO due to the significant difference in desorption temperature). These results were not surprising as they have been shown previously by work in our lab on the $Pd_n/TiO_2(110)$ model catalyst system.[2]

One result that was surprising, however, is the distinct differences seen at high temperature for the Pt_4 and Pt_{14} clusters. Pt_4 behaves basically as expected with a nearly complete recovery of the Pt signal after complete desorption of the CO, with the final Pt signal being slightly lower than as deposited, consistent with the Pt ISS signal measured after a CO TPD for Pt_4. The larger cluster, Pt_{14}, behaves very differently and unexpectedly at temperatures above 500 K. While the CO binding behavior seems to appear the same as for Pt_4, with the low temperature CO binding to the periphery and the high temperature CO binding on top of the cluster, the effect heating has on the physical structure of the cluster is drastically different. For simply heating the Pt_{14} cluster with or without CO present, the Pt ISS signal drops significantly upon heating to 550 K with another drop occurring at 650 K. This drop in signal is significantly more severe than for Pt_4, which is surprising because it is generally thought that smaller clusters sinter more efficiently than larger ones. Either Pt_4 and Pt_{14} do not follow this trend, or the dramatic change observed for Pt_{14} is due to the cluster restructuring to more significantly 3-

dimensional, with the fact that it occurs regardless of adsorbate coverage suggesting it is just a thermal effect. The same process may be occurring for Pt_4, but since it is such a relatively small cluster, there is very little restructuring that is possible.

Overall, the ISS results give a relatively complete picture (save compared to an STM image) of the physical structure of the size-selected clusters, with a clear transition from single to multilayer structure occurring between Pt_7 and Pt_8. Post reaction, the Pt in the surface layer has decreased dramatically, presumably due to compounding effects of sintering, restructuring, and stubborn adsorbates. For CO bound to the clusters, the two CO desorption sites measured with TPD are clearly identified as peripheral for the low temperature site, and atop for the high temperature site and thermal restructuring for the large clusters appears prominent. As alluded to earlier, oftentimes physical and electronic structure are related to one another, and the next section of this paper explores that connection.

5.3.2 PES to Determine Electronic Structure

For the $Pt_n/Al_2O_3/Re(0001)$ system studied here, core level spectroscopy of the Pt clusters could not be measured due to the overlap with a prominent shakeup feature from the rhenium substrate. The main features of the alumina thin film, however, were studied with XPS to determine how the electronic structure of the film changes under different conditions. How the core levels of the film shift as a function of film thickness has been discussed in detail elsewhere.[24] Briefly, as the film grows in thickness, the core level binding energies shift towards higher binding energy by nearly 1 eV until a steady energy is reached by a thickness of about 2 nm. These shifts are thought to be due to charge

transfer between alumina film and the rhenium substrate, which charges the alumina film positively; upon Pd/Pt deposition, the binding energies shift back the other direction towards lower binding energy, presumably because the Pd/Pt is donating some electron density into the electron depleted alumina film. Since the details of the core level spectroscopy of the film are published elsewhere, the scope of this paper will focus on the valence level spectroscopy of the film as well as the size selected Pt clusters, with the main focus being on the effects of adsorbates.

Figure 5.5 shows the region the UP spectra near the Fermi level for a clean alumina film, as well as the same film with 0.1 ML Pt_7 deposited on the surface. Since the clean alumina spectrum is dominated by the band gap in this low binding energy region, the new signal that appears as a result of Pt_7 deposition can clearly be distinguished from signal originating from the support. Since such a small amount of Pt is deposited, the only signal that is clearly present in the new spectrum is that in this near Fermi level region. Even though the deposited material is a metal, with an expected DOS to appear right at the Fermi level (0 BE), these very small clusters exhibit a pseudo-band gap with the DOS beginning a few tenths of an eV below the Fermi level. With the Pt_n spectra fitted (see inset), the shifts below the Fermi level for the different cluster sizes can be compared, and this is discussed in more detail elsewhere. Here, the discussion will focus on how this Pt and alumina UPS signal changes as a result of a CO oxidation reaction cycle.

For the alumina film, the UP spectrum has two main features: the first is the band gap that extends about 3-4 eV below the Fermi level, followed by the O 2p feature beginning at 5 eV and peaking at around 7 eV before extending the rest of the spectrum.

These two features are shown in Figure 5.6 for several different surfaces, including the clean alumina and Pt_7 shown in Figure 5.5. Besides the appearance of signal near the Fermi level upon Pt deposition, the O 2p feature of the alumina film also shifts significantly to lower binding energy (towards the Fermi level). This shift is consistent with that seen for the core levels of the alumina film which also shift towards lower binding energy, and again is thought to occur due to injection of electron density from the Pt clusters into the alumina film. Since the peak of the O 2p feature remains unchanged under certain conditions but the onset still shifts, the magnitude of the shifts were determined by finding the inflection point of the onset by fitting its first derivative. The shift is on the order of about 0.4 eV and does not appear to be cluster size-dependent as the shift does not deviate more than about +/- 0.05 eV which is the size of our estimated error.

Following the as deposited UP spectrum, the surface was then oxidized at 180 K with a 10 L O_2 dose, where the $Pt_n/Al_2O_3/Re(0001)$ surface studied here has been shown to adequately activate oxygen under these conditions. The effect of oxidation on the valence level structure of the film is similar to the deposition of Pt, i.e., a significant shift of the O 2p onset to lower binding energy signifying a decrease in the dipole between the $Al_2O_3/Re(0001)$ interface. The size of this shift is again size-independent with the spectrum shifting another 0.2 eV towards lower binding energy from the location of the O 2p onset after Pt deposition, as shown in Figure 5.6 for Pt_7. The same oxidation procedure on a film without any Pt also shows a similar shift, albeit smaller in magnitude (about 0.1 eV) presumably because the presence of Pt alters the oxygen binding on the surface since the oxygen can dissociatively adsorb.

Following the oxidation UPS, the sample was then dosed with 10 L CO at 180 K which is a saturation dose at this temperature. Unlike oxidizing, adsorbing CO has no effect on the electronic structure of the alumina film as the position of both the valence and core levels remain unchanged (see Figure 5.6). This may not come as a surprise since it is thought that the oxygen dissociatively adsorbs on the Pt clusters and can spillover onto the film, thus changing its electronic structure, whereas the CO only adsorbs to Pt clusters, and this adsorption is relatively weak (and nondissociative) as compared to the oxygen. With the surface now exposed to both reactants, the sample was heating to 650 K as with a normal temperature programmed reaction, and a subsequent UPS was performed. The effect on the electronic structure of the film is very small as the film shifts back towards higher energy by 0.1 eV, correcting for about half of the shift due to oxidation, presumably because some amount of the oxygen is removed from the surface as CO_2 (no O or O_2 is every seen desorbing from the surface up to 650 K). Once again, the magnitude of this shift is independent of cluster size in relation to the electronic structure of the alumina film.

The effect this procedure has on the valence level electronic structure of the Pt clusters is quite different than that of the alumina film. First of all, it should be noted that there are two significantly different size regimes with respect to physical structure (as discussed previously), but also electronic structure. Figure 5.7 shows the as-deposited UP spectra for Pt_4 and Pt_{14} -- a "small" and "large" cluster, respectively. The main point to notice is the as deposited shapes of the valence bands for these two clusters are different, with Pt_4 having a more gradual rise from the Fermi level with a higher DOS at about 3 eV, while Pt_{14} has a sharper rise near the Fermi level with the DOS leveling off before

meeting the O 2p peak. The relative shape differences shown here are consistent for n = 2,4,7 looking similarly "small," while n = 10,14,18 look similarly "large." These differences in shapes are reflected in their different shifts below the Fermi level, which have been shown to correlate to CO oxidation activity. What is the same for the two clusters, however, is how their valence structure changes as a function of stepping through a CO oxidation reaction cycle, which will be discussed in detail below.

Upon oxidizing with 10 L O_2 at 180 K, there is a shift of the O 2p band around 0.4 eV as discussing earlier, but there is no significant change in valence level of the spectrum as shown for Pt_4 and Pt_{14} in Figure 5.8. Since the Pt is directly involved in the dissociative adsorption of oxygen, the lack of change in the Pt valence structure is quite surprising. Similarly, small core level shifts with XPS for the Pd/TiO_2 system[2, 25] tend to suggest this result is not unique to Pt/Al_2O_3, and could be a result of the oxygen spilling over to the support and therefore interacting very little with the metal cluster after the dissociation of the oxygen molecule. Or perhaps the initial and final state effects that determine the measured binding energies in photoelectron spectroscopy "balance" in such a way that there appears to be no significant shift due to oxidation.

The adsorption of CO, however, has a significant effect on the electronic structure of the Pt clusters. For both cluster sizes shown in Figure 5.8, the DOS nearest the Fermi level are significantly attenuated, and the entire valence structure for Pt is affected until the spectrum is dominated by the O 2p feature. As a result, the measured shift of the valence level for the different cluster sizes is shifted towards higher binding energy, which can be interpreted as the HOMO for the Pt clusters is now farther below the Fermi level. Unlike other shifts seen in the alumina film, the shift caused by CO adsorption is

in fact cluster size-dependent, and the magnitude of the shift as a function of cluster size is plotted in Figure 5.9. The overall trend shows that as the cluster size gets smaller, the larger the shift of the Pt DOS below the Fermi level. This increased shift for larger (and more inactive) clusters could signal a stronger overlap of the bonding orbitals and therefore a stronger bond to the smaller clusters. Temperature programmed desorption results, however, do not show any significant difference in CO binding energy between cluster sizes as the CO desorption temperatures are the same (see Figure 5.4). What is different in the CO TPD results is that the smaller clusters generally have the largest amount of periphery CO bound to the clusters. Other data from our lab,[2] as well as theoretical calculations,[26-29] suggest the CO first binds on top of the cluster and is the high temperature desorption site, and that this CO does not have a significant effect on the electronic structure of the clusters; it is only when CO begins to bind at the periphery sites does a significant change occur. Since the smaller clusters bind more at their periphery, perhaps this explains why the measured valence level shift is larger for the smaller clusters.

After heating and completing the TPR cycle, the final UP spectra show another significant change in the valence level structure of the Pt clusters. Figure 5.8 shows these details for Pt_4 and Pt_{14}, with both clusters now looking like a "large" cluster with a sharper rise from the Fermi level, and an overall flatter DOS. Since all of the CO has been removed, it is not surprising to see a general return to a shape that resembles that of as deposited clusters. The shift of the valence levels closer to the Fermi level, as well as increased CO oxidation activity in the second TPR run (detail of which can be found here[30]) suggests the "small" clusters have sintered to resemble a "large" cluster. In fact,

when plotting the shift of all the clusters after a TPR as shown in Figure 5.9, it becomes clear that all of the clusters shift, including the large ones, and reach a similar final valence electronic structure.

5.4 Conclusion

The size-dependent physical and electronic properties of the $Pt_n/Al_2O_3/Re(0001)$ model catalyst system have been investigated in detail using ISS, PES, and TPD. As deposited ISS results suggest a shift from single to multilayer occurs between Pt_7 and Pt_8, with Pt atoms having an anomalously low Pt ISS intensity possibly due to sintering. ISS performed after a CO TPD or a CO oxidation reaction have a reduced amount of Pt present in the surface layer, presumably due to compounding factors of restructuring, sintering, and adsorbates. CO TD-ISS coupled with CO TPD results show the low temperature CO is bound at the periphery of the clusters, while the high temperature CO is bound on top of the Pt clusters. These findings are similar to those for the $Pd_n/TiO_2(110)$ system previously studied in our lab.[2]

The core and valence level structure of the alumina film were found to change upon Pt deposition and a TPR cycle with the effects being independent of cluster size. The valence level structure of the as deposited Pt_n clusters show size-dependent shifts below the Fermi level and these shifts remain unchanged after 180 K oxidation. CO exposure attenuated much of the Pt signal near the Fermi level for all clusters, and shifted the onset of the valence level towards higher binding energy, with the shift being greater for the smaller clusters. After heating the sample to 650 K to complete the TPR cycle, the valence level for all cluster sizes studied shifts very near the Fermi level with a

complete loss of size-dependent electronic structure present. The ISS and UPS results following a TPR cycle suggest all cluster sizes reach some similar physical and electronic final state, which reflects a similar loss in size-dependent CO oxidation activity in sequential runs.

5.5 References

1. F. Gao and D. W. Goodman, Annual Review of Physical Chemistry **63**, 265-286 (2012).

2. W. E. Kaden, W. A. Kunkel, F. S. Roberts, M. Kane and S. L. Anderson, J. Chem. Phys. **136**, 204705/204701-204705/204712 (2012).

3. V. Habibpour, Z. W. Wang, R. E. Palmer and U. Heiz, Journal of Applied Sciences **11** (7), 1164-1170 (2011).

4. D.-C. Lim, C.-C. Hwang, G. Gantefoer and Y. D. Kim, Phys. Chem. Chem. Phys. **12** (46), 15172-15180 (2010).

5. C. T. Campbell, A. W. Grant, D. E. Starr, S. C. Parker and V. A. Bondzie, Topics in Catalysis **14** (1-4), 43-51 (2001).

6. D. R. Rainer, C. Xu and D. W. Goodman, J. Mol. Catal. A: Chem. **119** (1-3), 307-325 (1997).

7. D. W. Goodman, Surf. Rev. Lett. **2** (1), 9-24 (1995).

8. S. Lee, C. Fan, T. Wu and S. L. Anderson, J. Chem. Phys. **123**, 124710 124713 pages. (2005).

9. K. J. Boyd, A. Lapicki, M. Aizawa and S. L. Anderson, Review of Scientific Instruments **69**, 4106-4115 (1998).

10. F. S. Roberts and S. L. Anderson, Review of Scientific Instruments (2013).

11. P. J. Chen and D. W. Goodman, Surf. Sci. **312**, L767-L773 (1994).

12. S. C. Street and D. W. Goodman, Chem. Phys. Solid Surf. **8** (Copyright (C) 2013 American Chemical Society (ACS). All Rights Reserved.), 375-406 (1997).

13. X. Lai, C. C. Chusuei, K. Luo, Q. Guo and D. W. Goodman, Chem. Phys. Lett. **330** (3,4), 226-230 (2000).

14. Y. Wu, E. Garfunkel and T. E. Madey, Surf. Sci. **365** (Copyright (C) 2012 American Chemical Society (ACS). All Rights Reserved.), 337-352 (1996).

15. Y. Wu, E. Garfunkel and T. E. Madey, J. Vac. Sci. Technol., A **14** (Copyright (C) 2012 American Chemical Society (ACS). All Rights Reserved.), 2554-2563 (1996).

16. M. D. Kane, F. S. Roberts and S. L. Anderson, Faraday Disc. **162**, 323 - 340 (2013).

17. W. E. Kaden, T. Wu, W. A. Kunkel and S. L. Anderson, Science **326**, 826-829 (2009).

18. N. Isomura, X. Wu, H. Hirata and Y. Watanabe, J. Vac. Sci. Technol., A **28** (5), 1141-1144 (2010).

19. Y. Watanabe, X. Wu, H. Hirata and N. Isomura, Catalysis Science & Technology **1** (8), 1490-1495 (2011).

20. G. R. Bamwenda, S. Tsubota, T. Nakamura and M. Haruta, Catalysis Letters **44** (1,2), 83-87 (1997).

21. M. S. Chen and D. W. Goodman, Science **306** (5694), 252-255 (2004).

22. M. Valden, X. Lai and D. W. Goodman, Science **281** (5383), 1647-1650 (1998).

23. N. Isomura, X. Wu and Y. Watanabe, J. Chem. Phys. **131** (16), 164707/164701-164707/164704 (2009).

24. M. D. Kane, F. S. Roberts and S. L. Anderson, Unpublished results (2014).

25. W. E. Kaden, W. A. Kunkel, M. D. Kane, F. S. Roberts and S. L. Anderson, J. Am. Chem. Soc. **132**, 13097–13099 (2010).

26. P. Liu, J. Phys. Chem. C **116**, 25337−25343 (2012).

27. J. Zhang and A. N. Alexandrova, J. Chem. Phys. **135** (17), 174702/174701-174702/174710 (2011).

28. J. Zhang and A. N. Alexandrova, arXiv.org, e-Print Archive, Condensed Matter, 1-4, arXiv:1112 4032v1111 [cond-mat mtrl-sci] (2011).

29. S. V. Ong and S. N. Khanna, J. Phys. Chem. C **116** (4), 3105-3111 (2012).

30. F. S. Roberts, M. D. Kane and S. L. Anderson, Unpublished results (2014).

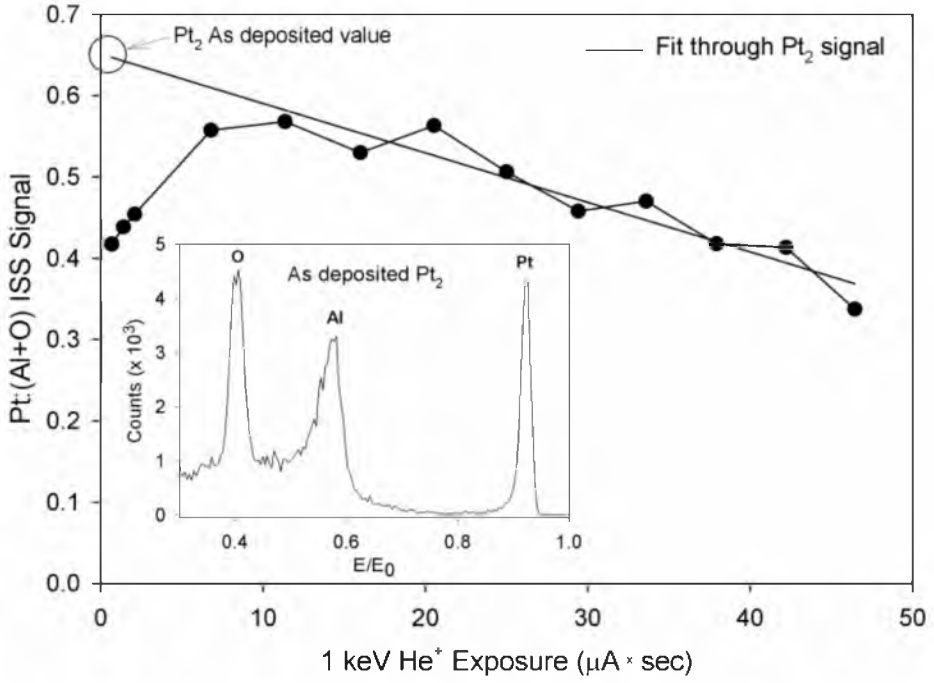

Figure 5.1 A series of 3 "low flux" ISS spectra followed by 10 "high flux" ISS spectra were performed to determine the Pt:(Al+O) intensity as a function of 1 keV He^+ exposure for the as-deposited Pt_2 model catalyst. The fit passes through the down-sloping signal only in order to extrapolate back to 0 He^+ exposure which determines the as deposited value for each cluster size. The inset shows an example of a "high flux" ISS spectrum.

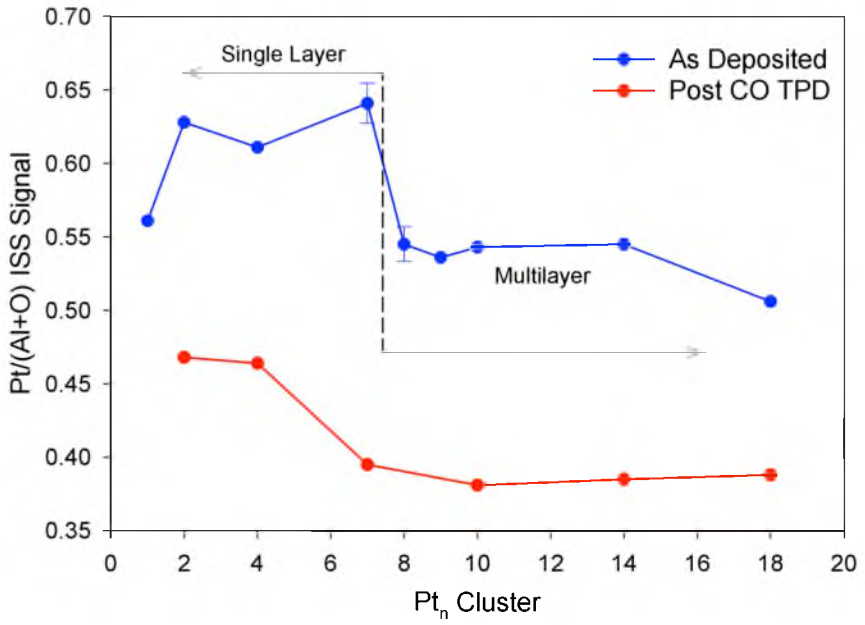

Figure 5.2 As-deposited Pt:(Al+O) values (blue) as a function of cluster size (as determined by the procedure detailed in the text and Figure 5.1). The dashed line shows the separation between the single and multilayer regimes between Pt_7 and Pt_8. The red shows the Pt:(Al+O) signal after a single CO TPD was performed.

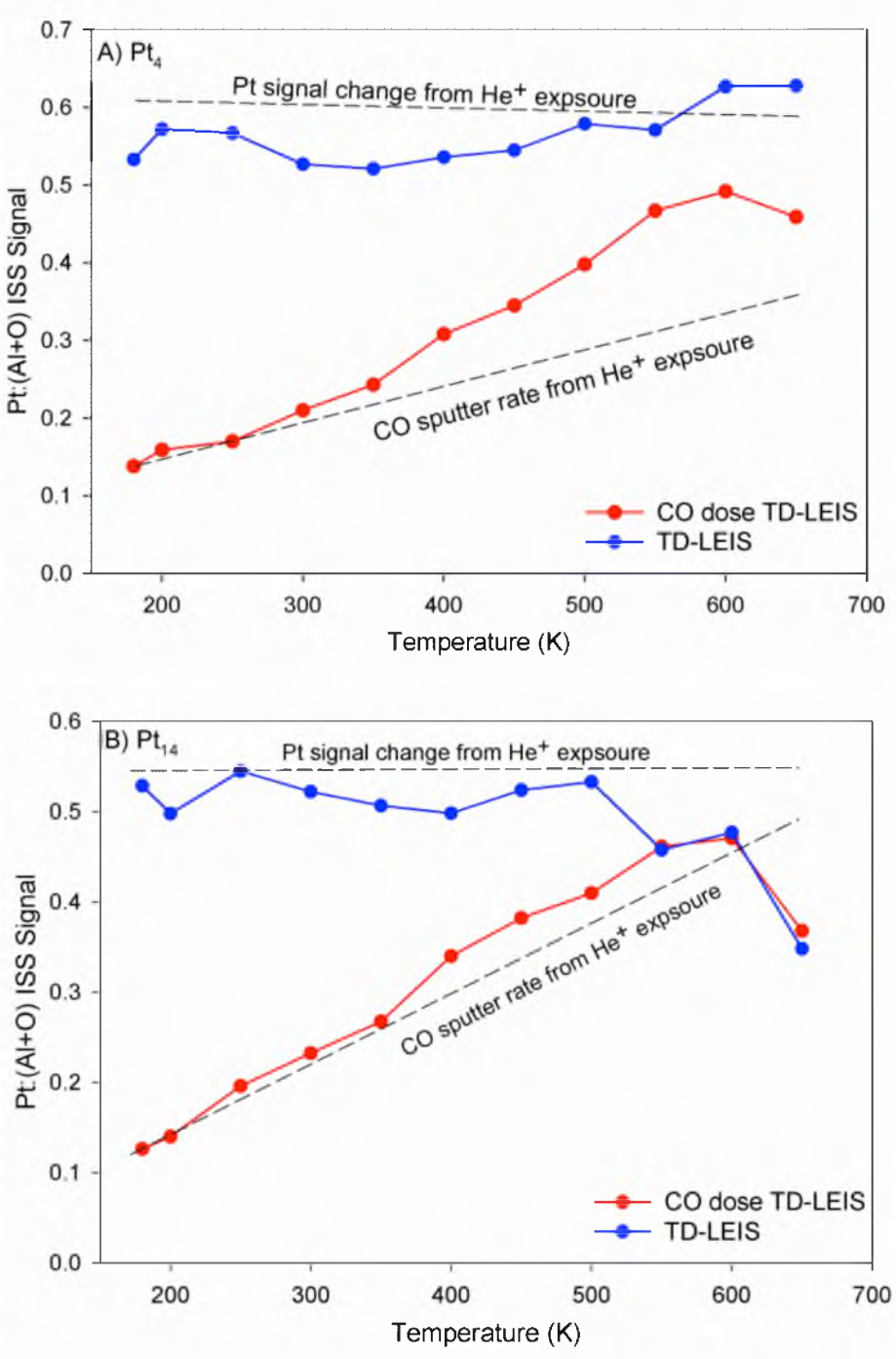

Figure 5.3 Temperature-dependent ISS results (TD-ISS) for clean (blue) and CO dosed (red) Pt_4 (part A) and Pt_{14} (part B). The dashed lines show the Pt and CO sputter rates as a function of He^+ exposure, and the details of the experiment can be found in the text.

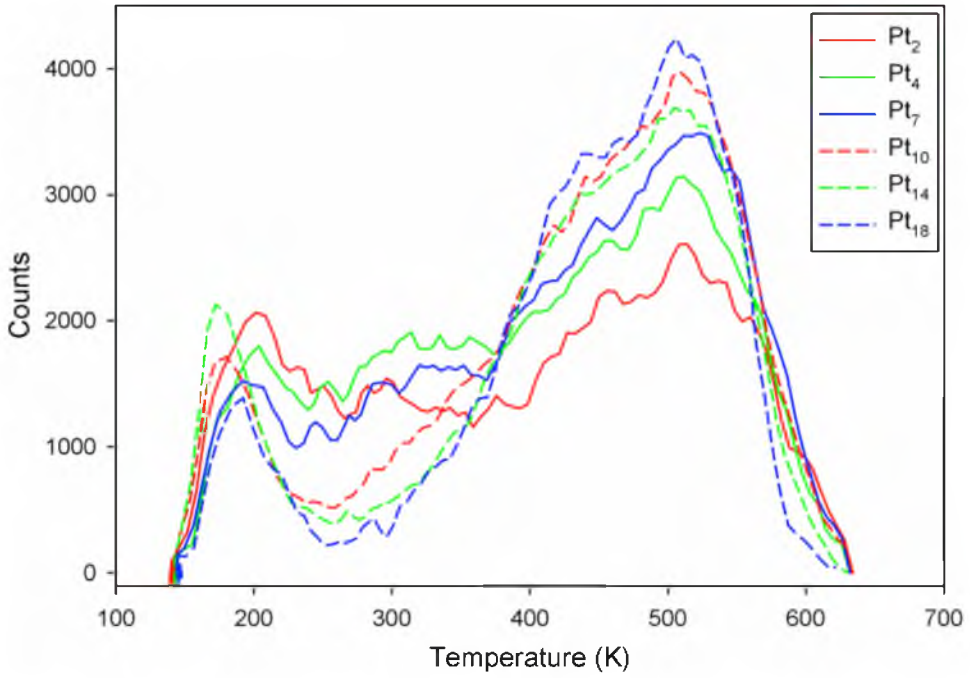

Figure 5.4 The first CO TPD performed on several pristine $Pt_n/Al_2O_3/Re(0001)$ model catalysts. Notice the inverse size-dependence for the intensity of the high temperature desorption site (500 K) and the low temperature feature (200-300 K).

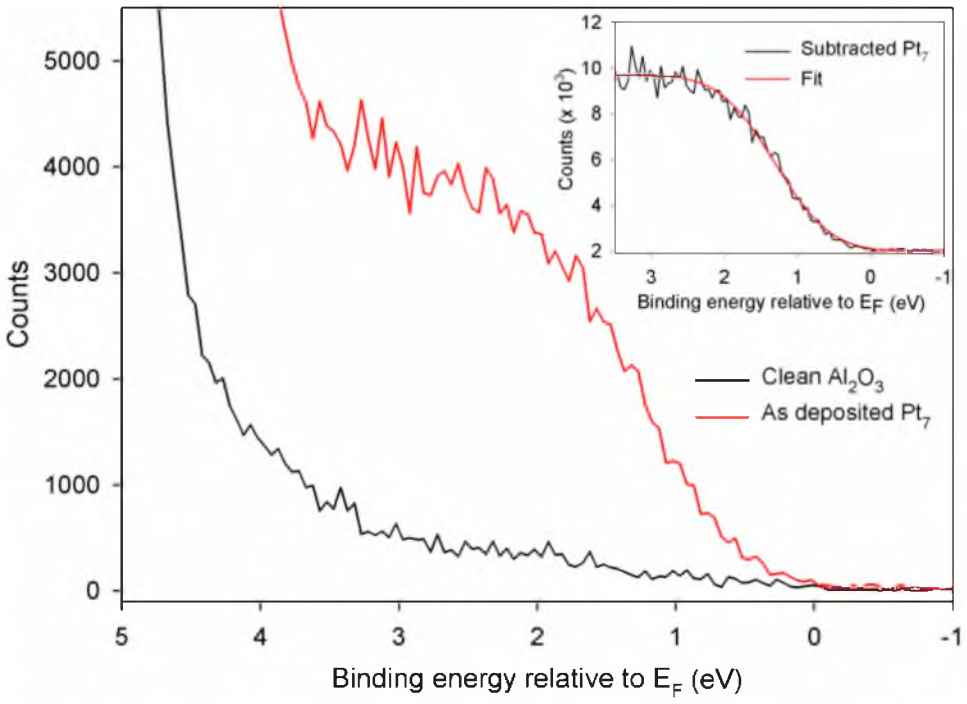

Figure 5.5 UP spectra for clean Al_2O_3 (black) and as-deposited Pt_7 (red) shown near the Fermi level. The inset shows the Pt_7 UPS signal with the clean Al_2O_3 spectra subtracted out along with the fit to determine how far the onset of the valence band is shifted below the Fermi level (0 BE).

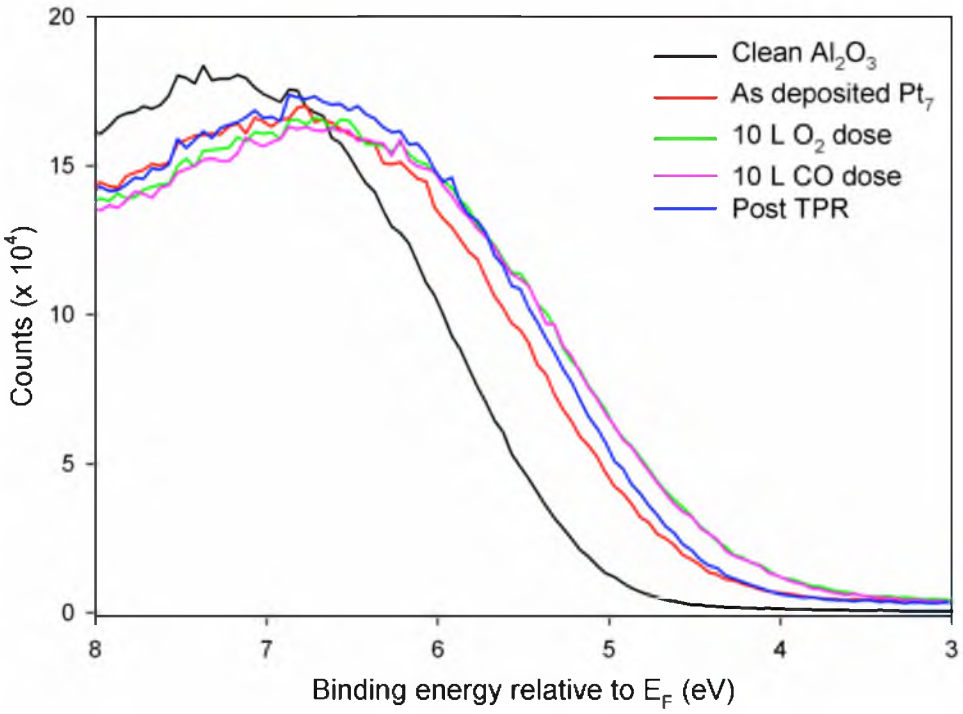

Figure 5.6 UP spectra showing only the onset of the O 2p valence band. Notice how the onsets shift under different surface conditions.

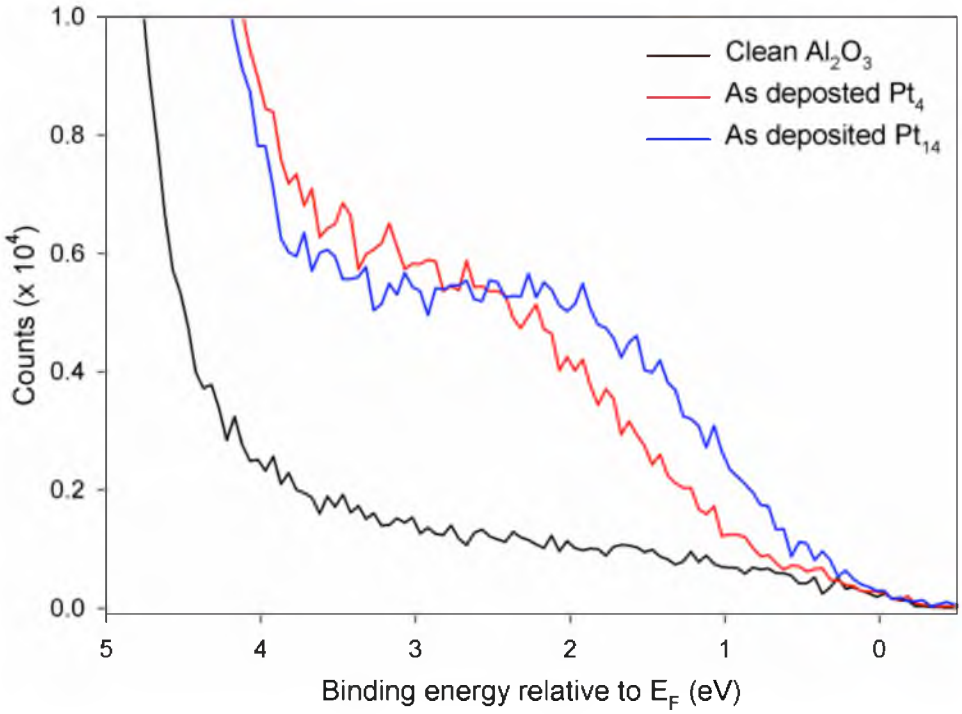

Figure 5.7 UP spectra showing the difference between the shapes of the DOS near the Fermi level for Pt_4 (red) and Pt_{14} (blue) which represent a "small" and "large" cluster, respectively. Pt_{14} has a higher DOS near the Fermi level as compared to Pt_4 and levels off sooner at 3 eV before being lost in the O 2p band.

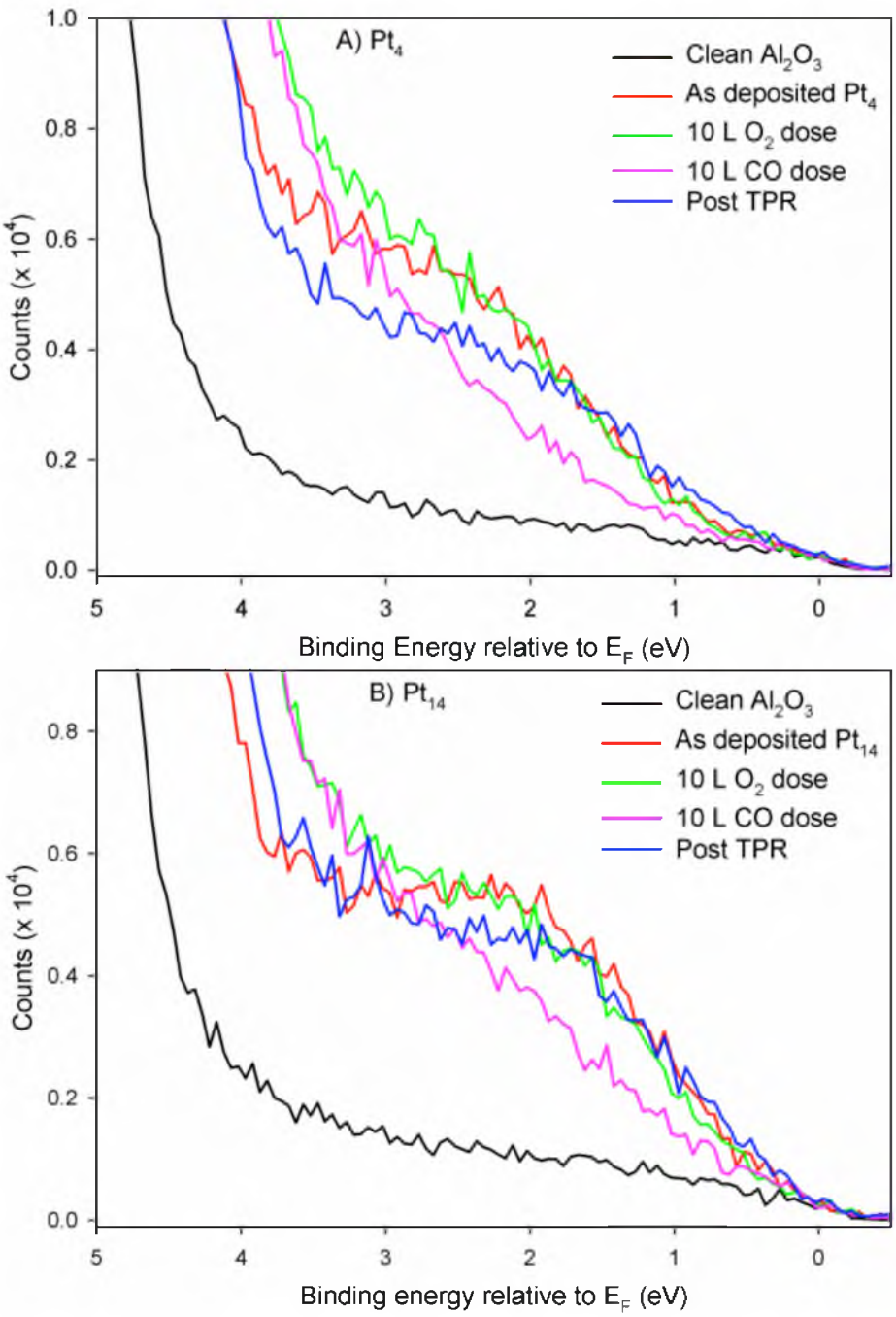

Figure 5.8 UP spectra showing the valence level for Pt_4 (part A) and Pt_{14} (part B) under different conditions (same as those shown for the O 2p band in Figure 5.6). There is no significant change after oxidation, but a CO dose and TPR cycle affect both cluster sizes similarly.

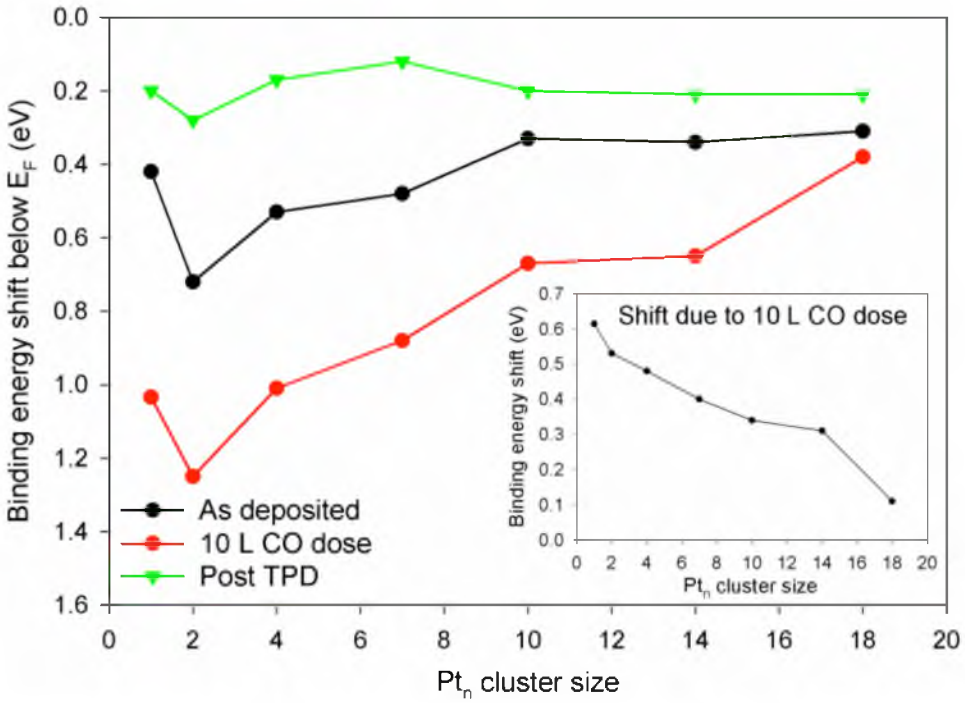

Figure 5.9 The shifts of the Pt_n valence band below the Fermi level as a function of cluster size are shown under various conditions: as-deposited clusters (black), CO dose (red), and after a CO TPD (green). The inset shows the magnitude of the shift from the as-deposited value due to a 10 L CO dose, with the larger shift occurring for the smaller cluster sizes.

CHAPTER 6

CONCLUSION

6.1 Conclusion

The work presented in this dissertation used a combination of surface analysis techniques to determine the properties that control catalytic CO oxidation efficiency for size-selected model catalysts. The focus was on using the newly added VUV lamp to elucidate valence electronic structure, which was found to track nicely with core level structure for the $Pd_n/TiO_2(110)$ (n = 1-25) system, as discussed in Chapter 3. The valence band structure was also monitored throughout a CO oxidation cycle in order to determine how CO adsorption and oxidation both affect the electronic structure of the model catalyst.

The newly investigated $Pt_n/Al_2O_3/Re(0001)$ (n = 1-18) system revealed very strong size-dependence, by about a factor of eight, for the CO oxidation reaction. The investigation of this reaction system, detailed in Chapter 4, determined the size-dependent valence electronic structure shifts below the Fermi level to strongly correlate (inversely) with catalyst activity. It appears the shifts in the valence band controls not only how much CO is bound in the high temperature desorption site, but also how much oxygen is dissociatively adsorbed for a given cluster size, thus determining how efficiently the CO oxidation reaction proceeds.

Detailed investigation of the physical properties of the $Pt_n/Al_2O_3/Re(0001)$ (n = 1-18) model catalyst system, presented in Chapter 5, shows the formation of a multilayer between Pt_7 and Pt_8 to be critical in the resulting electronic structure and catalytic activity. Again, the effect of adsorbates was investigated with an emphasis on how the physical and electronic structure change throughout a reaction.